DE

CHARACTERIZATION AND CONTROL OF THE FI
IN CERAMIC MATRIX COMPO

R. A. Lowden

ABSTRACT

ORNL/TM--11039

DE91 000922

Metals and Ceramics Division

CHARACTERIZATION AND CONTROL OF THE FIBER-MATRIX INTERFACE IN CERAMIC MATRIX COMPOSITES

R. A. Lowden

Date Published: March 1989

Prepared for the
DOE Office of Fossil Energy
AA 15 10 10 0

Prepared by the
OAK RIDGE NATIONAL LABORATORY
Oak Ridge, Tennessee 37831-6285
operated by
MARTIN MARIETTA ENERGY SYSTEMS, INC.
for the
U.S. DEPARTMENT OF ENERGY
under Contract DE-AC05-84OR21400

TABLE OF CONTENTS

LIST OF TABLES

LIST OF FIGURES

ACKNOWLEDGMENTS

The author wishes to thank R. A. Bradley, R. R. Judkins, and P. T. Carlson for their interest in and support of the characterization of interfaces in composites. Special appreciation is to be extended to R. C. Melton for his scanning electron microscopy analysis of fracture surfaces; R. A. Padgett, Jr., for the Auger analysis of fracture surfaces;, and G. C. Marsh for the preparation of the metallographic samples. R. D. Cole is acknowledged for conducting a portion of the mechanical properties testing.

Special gratitude must be expressed to H. R. Livesey for the meticulous preparation of many of the drawings and figures. The author also thanks those involved in the preparation of the manuscript for publication: Lydia Cornell for the initial editing, G. R. Carter and M. R. Upton for final lay-out and preparation, and P. H. Wilson for finishing touches and final editing. Thanks also go to C. J. McHargue and J. E. Spruiell for their advice and direction as well as their review of the manuscript.

The author finally expresses great appreciation to J. O. Stiegler, T. M. Besmann, and the members of the Ceramic Surface Systems Group for their patience, understanding, guidance, and assistance in completing the work and the report.

Strengthening with fibers has so many advantages -- high strength, toughness, high-temperature strength, thermal stability, and cheap, light and chemically inactive materials for the fibers -- that it seems certain to become the basis of engineering solids of the future. The main problems are technological. We have to develop ways of making and assembling the fibers cheaply by the ton and develop new methods of engineering design and fabrication to make best use of their properties. These developments will require great effort but the stakes are high.

A. H. Cottrell (1)

CHARACTERIZATION AND CONTROL OF THE FIBER-MATRIX INTERFACE IN CERAMIC MATRIX COMPOSITES*

R. A. Lowden

ABSTRACT

Fiber-reinforced SiC composites fabricated by thermal-gradient forced-flow chemical-vapor infiltration (FCVI) have exhibited both composite (toughened) and brittle behavior during mechanical property evaluation. Detailed analysis of the fiber-matrix interface revealed that a silica layer on the surface of Nicalon Si-C-O fibers tightly bonds the fiber to the matrix. The strongly bonded fiber and matrix, combined with the reduction in the strength of the fibers that occurs during processing, resulted in the observed brittle behavior.

The mechanical behavior of Nicalon/SiC composites has been improved by applying thin coatings to the fibers, prior to densification, to control the interfacial bond. Varying degrees of bonding have been achieved with different coating materials and film thicknesses. Fiber-matrix bond strengths have been quantitatively evaluated using an indentation method and a simple tensile test. The effects of bonding and friction on the mechanical behavior of this composite system have been investigated.

Fiber coatings not only weaken the fiber-matrix bond, increasing toughness, but can protect the fibers from chemical attack and hinder

---

*Research sponsored by the U.S. Department of Energy, AR&TD Fossil Energy Materials Program [DOE/FE AA 15 10 10 0, Work Breakdown Structure Element ORNL-1(c)] under contract DE-AC05-84OR21400 with Martin Marietta Energy Systems, Inc.

chemical interactions at the interface. Electron microscopy and surface analyses were utilized to characterize interface compositions and interactions. These results have been used to further characterize fiber-matrix interfaces and their influence on the mechanical behavior of these composite materials.

1. INTRODUCTION

During the last several years, tremendous emphasis has been placed on developing high-performance materials for use in elevated-temperature applications. Advanced designs for high-velocity aircraft, efficient power-conversion systems, and aerospace vehicles call for limited or extended service at high temperatures in a variety of environments. Conventional metals and alloys do not possess the thermal stability or elevated-temperature properties to meet the advanced material requirements. Ceramic fiber-reinforced metal-matrix composites have been developed as replacements for conventional metallic materials (2-4), but most are susceptible to property degradation, particularly under conditions of thermal cycling in which fiber-matrix thermal expansion differences lead to internal failure caused by fiber fragmentation.

Many ceramics and glass-ceramics exhibit relatively high strength and stability at elevated temperatures. These materials have low densities and are chemically inert. Unfortunately, many conventional monolithic ceramic materials lack stress-relieving or energy-absorbing mechanisms, and therefore, are inherently brittle and sensitive to thermal shock. In an attempt to increase the strength of ceramic materials and, more importantly, the work of fracture and toughness, barriers to crack propagation have been incorporated into ceramic matrices. Particles, platelets, whiskers, and fibers have been used as reinforcement in ceramic matrices, the most potential being in the areas of fiber and whisker reinforcement.

2. HISTORICAL DEVELOPMENTS IN CERAMIC COMPOSITES

The concept of fiber-reinforced ceramic materials is not new. Throughout history, fibers have been added to brittle materials to improve their properties. Straw and animal hair were mixed with clay and the mixture formed into bricks or pottery. The fiber acted to improve the handleability of the materials prior to drying or firing and to increase the strength and fracture resistance of the finished product. It has been suggested that goat hair was added to pottery in ancient times and upon firing was converted to carbon. These materials may be the first examples of carbon-fiber-reinforced ceramic composites (5-7). Composite jars and vessels were supposedly less prone to breakage than their unreinforced counterparts.

Although the advantages of ceramic composites have been recognized for many years, most of the developments in fiber-reinforced ceramic materials have occurred in the past twenty years. In some early work, randomly oriented, discontinuous metal fibers were incorporated into a range of ceramic matrices (5,7,8-10). The result was improved toughness, and in some cases, increased strength. Unfortunately, these modest improvements were accompanied by significant disadvantages in that the densities were increased relative to the monolithic materials, the ceramic matrices failed to protect the fibers from degradation in damaging environments, and the thermal expansion mismatch between fibers and matrices resulted in premature failure of the composites because of matrix cracking upon temperature cycling. By the late 1960s, the development of these composite materials had been abandoned to pursue more promising ventures.

The development of low-density, high-strength carbon fibers led to a renewed interest in fiber-reinforced composites. In contrast to the earlier research that attempted to improve the toughness of brittle ceramics by the addition of ductile metal fibers, researchers began to investigate the possibility of reinforcing brittle matrices with the relatively brittle carbon fibers. The majority of the initial efforts were in the development of carbon-carbon composites for defense applications; however, carbon-carbon composites begin to oxidize in air at temperatures above 700 K, thereby limiting their usefulness. Alternative matrix materials were examined, and again, ceramics were produced that possessed the desired attributes of high strength, thermal stability, chemical inertness, and oxidation resistance.

Some of the original research examining the toughening of ceramic matrices by the addition of carbon fibers was initiated in the late 1960s and early 1970s at Harwell and at the National Physics Laboratory in England (1,11-15). Large increases in the work of fracture were attained by incorporating carbon fibers into glass and glass-ceramic matrices. The composites demonstrated high strength and toughness and could be fabricated using techniques similar to those already well established in the production of polymeric matrix composites. As with metal matrix and metal fiber-reinforced ceramic composites, these materials lacked thermal stability because of the relatively large differences in the fiber and matrix thermal expansions and the poor oxidation resistance of the carbon fibers. Interest in the materials waned as efforts to improve the oxidation resistance of the carbon-fiber-glass matrix composites were unsuccessful.

Although these materials did not perform well at elevated temperatures, the materials were not abandoned; instead, the fabrication techniques, physical properties, and mechanical behavior of carbon-fiber-reinforced glasses and glass-ceramics were studied in detail. Every aspect of these composite materials was thoroughly examined in hopes that a new improved fiber would be discovered. The need for a more stable and oxidation-resistant reinforcement was met by the introduction of ceramic filaments produced by the chemical-vapor deposition of silicon carbide (SiC) on carbon or tungsten fiber cores (16). The filaments were large in diameter (140 μm), extremely stiff, and costly. The fibers were used in glass matrices, but the aforementioned factors combined with a loss of strength at 1075 K limited their usefulness.

Research continued to develop a low-cost oxidation-resistant fiber with good mechanical properties. Yajima et al. (17,18) developed a continuous fine-grained SiC fiber having high strength and excellent oxidation resistance. The fibers were synthesized from polycarbosilane, an organometallic precursor, and processing was similar to that used in the production of carbon fibers. The fibers consisted mainly of SiC but also contained silica and free carbon. The introduction of the Nicalon® SiC fibers spawned a new era in the development of ceramic-ceramic composites. The availability of sufficient quantities of the Nicalon Si-C-O fibers brought forth an upsurge in the research and development of ceramic-ceramic composites (19,20).

®Nippon Carbon, Tokyo, Japan.

3. FABRICATION TECHNIQUES

3.1 Introduction

A wide range of techniques exists for the fabrication of polycrystalline ceramic bodies (21,22). The methods for the fabrication of monolithic ceramics generally involves starting with the raw materials in powdered form. The powder or powder mixture is first consolidated as a loose powder in a shaped mold, an extruded solid with aqueous or organic binders, or a compact formed by cold pressing. Final consolidation into a monolithic article then involves the application of heat or possibly a combination of elevated temperature and pressure. Glasses soften and melt at lower temperatures, and components can be produced utilizing the molten phases. Glass-ceramics can be processed similarly, taking advantage of the glassy state at lower temperatures (23). Fine-grained polycrystalline material is produced by devitrification of the material through heat treatments. These methods have been used in producing fiber-reinforced ceramic composites with varying success (21,22).

The manufacture of fiber-reinforced composites with polycrystalline ceramic matrices by employing powder-processing techniques involves blending the fibers with the unconsolidated matrix material and then processing the fiber-powder mixture to form a densified material. The combining of fibers and matrix precursor can be accomplished in many ways. For random short fibers, simple mixing of the fibers and powders may suffice (5,24,25). Continuous yarns or woven fabric can be impregnated by passing the fibers through a slurry of powdered matrix material and binder to produce a an unimpregnated tape or sheet (19,20,26). The tapes or sheets can be assembled into stacked

lay-ups or filaments wound into cylindrical shapes and densified, usually by hot pressing.

The object of consolidation is to produce a dense material while inflicting minimal damage to the fiber or whisker reinforcement. The majority of densification processes employ high temperatures and some, such as hot pressing, utilize elevated temperature combined with extreme pressure. These conditions may have detrimental effects on the properties of the reinforcing component.

3.2 Hot Pressing

The most widely used technique for producing ceramic matrix composites is hot pressing. Hot pressing has been used to fabricate composites from a large selection of polycrystalline ceramic matrices (21,22,25). The properties of the composites depend on fabrication parameters such as the particle size distribution of the powders and the temperatures and pressures employed. These parameters control the porosity of the matrix and the damage introduced into the fibers and can affect fiber-matrix bond strength. Hot pressing has yielded fiber-reinforced ceramic composites with reproducible properties, and the materials and processing conditions have been studied in depth. However, the temperatures and pressures necessary to attain the required densities in the matrices severely damage many of the available fibers.

An advantage of hot pressing is that the procedure does not require binders to stiffen preforms prior to densification; thus, components can be fabricated with close dimensional tolerances. The technique is restricted to relatively simple shapes but a similar process, hot

isostatic pressing (HIP), can be applied to more complex geometries with comparable results. Hot pressing is ideal for the fabrication of short-fiber or whisker-reinforced ceramics (such as the SiC-reinforced alumina) and unidirectional lay-ups, but it is expensive. Its application to multidimensional continuous-fiber-reinforced composites is also limited; therefore, other techniques for the fabrication of fiber-reinforced ceramic composites have been explored.

3.3 Sintering

Alternative powder-processing techniques incorporate a forming step and a subsequent sintering/firing densification stage. "Greenware" preforms are fabricated by cold pressing, slip casting, or extruding a fiber-powder-binder mixture or slurry. The binders are removed by low-temperature heat treatments, and the components are consolidated by firing to high temperatures. The major disadvantage of these processes is the large degree of shrinkage that occurs during sintering. The shrinkage produces cracks and porosity in the composite matrix, resulting in poor properties. The high sintering temperatures can also damage the fiber reinforcement.

3.4 Unconventional Techniques

Most of the aforementioned fabrication techniques are more suited to short fibers or whiskers than to continuous fibers or filaments. Many composites processed using the methods described herein have exhibited improved mechanical behavior over monolithic ceramics, but the processes are not easily adaptable to the manufacture of continuous-fiber composites. The forming and pressing steps cannot be used for large

plates or complex shapes containing continuous-fiber-reinforced materials; therefore, other more versatile techniques have been explored.

Impregnation with polymeric ceramic precursors has seen limited success (27). The processing techniques are similar to those developed for the production of carbon-carbon composites. The pyrolysis of the organometallic precursors to a fully dense ceramic is a complicated process that is accompanied by large volume changes. Multiple impregnations are necessary to obtain reasonable (77% theoretical) densities. Another disadvantage is that the polymers are also used in the manufacture of the fibers; thus, chemical interactions during pyrolysis are of great concern.

Reaction bonding is another interesting technique that has been used in the production of ceramic components (28,29). Most of the development of this process has involved the nitriding or carburizing of silicon powder preforms to form Si_3N_4 and SiC. Fiber-reinforced ceramics have been fabricated utilizing this method with varying results. Chemical interactions at the fiber-matrix interface and consumption of the reinforcement have detrimental effects on the properties of the products. Protective fiber coatings are currently being evaluated to inhibit fiber-matrix interaction, thereby improving composite properties (29).

3.5 Chemical Vapor Infiltration

High toughness and strengths have been reported for a number of fiber-reinforced ceramic composite systems; however, many of the described fabrication techniques tend to mechanically, thermally, or chemically damage the fibers during processing. To overcome the hazards of conventional ceramic processing, ceramic composites have been produced

utilizing the comparatively low-temperature low-stress process of chemical-vapor deposition (CVD). Porous, fibrous structures are densified by infiltrating the substrates with vapors that deposit as solid phases on and around the fibers to form the matrix.

CVD has been employed to form the matrix of fiber-reinforced ceramic composites (30-39). Matrices of SiC, Si_3N_4, B_4C, BN, and TiB_2 have exhibited good mechanical properties, but the processing times have been extremely long (weeks). Three types of infiltration methods have been used to fabricate fiber-reinforced ceramic composites: (1) an isothermal process in which gases diffuse into the preform, (2) a thermal-gradient process in which the gases diffuse into the fibrous body, and (3) an isothermal process in which the gases are forced through the substrate by a pressure gradient. The resulting composites possessed improved mechanical behavior compared with unreinforced monolithic ceramics, but the long processing times are costly.

4. FORCED-FLOW THERMAL-GRADIENT CHEMICAL-VAPOR INFILTRATION

A new process combining the thermal-gradient and pressure-gradient (forced-flow) approaches has been developed at Oak Ridge National Laboratory (ORNL) (40-44). A schematic of the process is shown in Figure 4.1. Fibrous preforms are retained in a graphite holder that contacts a water-cooled metal gas distributor, thus cooling the bottom and side surfaces of the substrate. The top of the fibrous preform is exposed to the hot zone of the furnace, creating a steep temperature gradient across the substrate. The reactant gases pass into the cooled portion of the fibrous body but do not react because of the low temperature. The gases continue from the cooled region of the preform into the hot zone, where they decompose and deposit the solid matrix phase. Deposition of the matrix within the hot region of the preform increases the density and thermal conductivity of the substrate, so that the hot region moves progressively from the top of the preform toward the bottom. When the top surface becomes coated and is no longer permeable, the gases flow radially through the substrate to the preform circumference and exit through the perforated retaining lid.

The majority of this work has investigated the infiltration of Nicalon fibrous preforms with CVD SiC (41-44). The preforms were fabricated by stacking multiple layers of SiC cloth into the graphite holders. This technique provides a two-dimensional reinforcement and is extremely reproducible. Composites processed utilizing this technique have exhibited improved mechanical behavior compared with monolithic

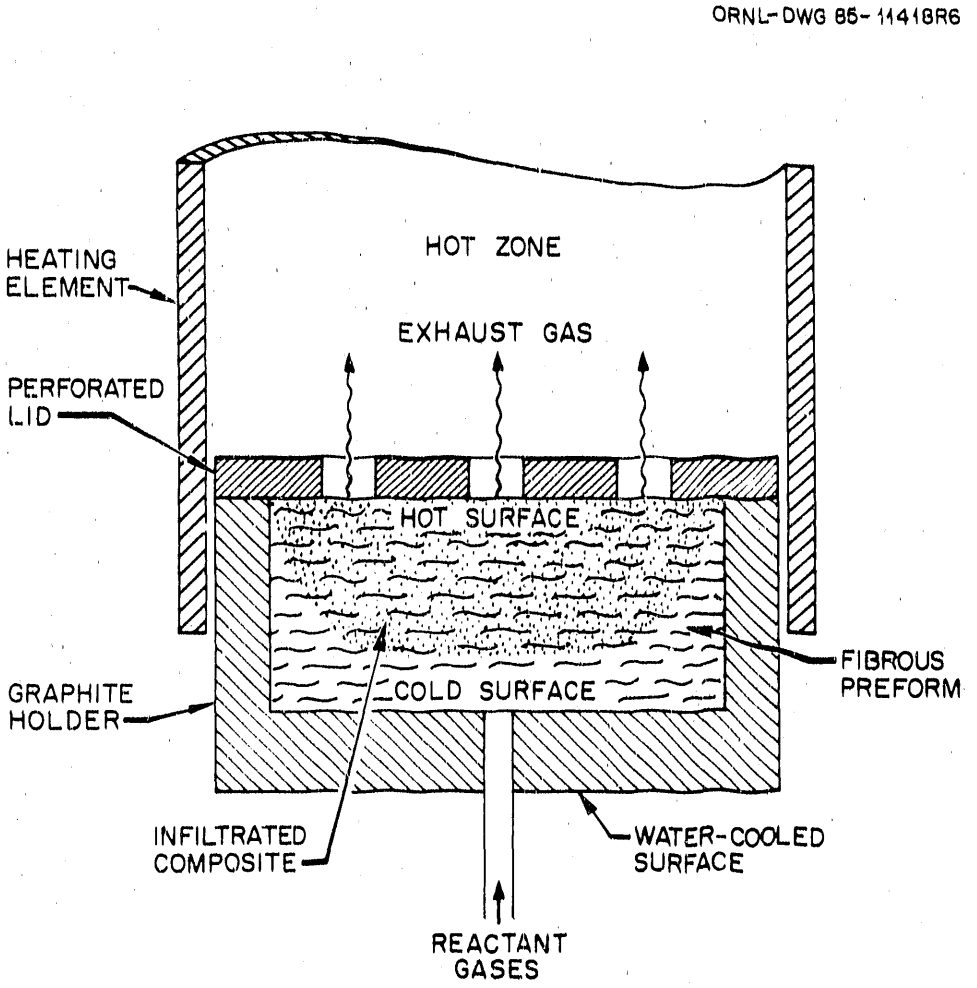

Figure 4.1. Schematic of the forced-flow thermal-gradient chemical-vapor-infiltration process developed at ORNL.

materials and certain ceramic-fiber-reinforced ceramic matrix composites. Densities >90% theoretical and flexure strengths approaching 600 MPa accompanied by large strain to failure and extensive fiber pull-out have been achieved in relatively short processing times (18 to 24 hours).

5. COMPOSITE DESIGN

5.1 Introduction

Composites are produced when two materials are joined together to give a combination of properties that cannnot be attained in the original materials. Composite materials are designed to give beneficial combinations of strength, stiffness, high-temperature performance, weight, thermal conductivity, or corrosion resistance. The properties of the product are entirely dependent on the constituents and the physical, chemical, and mechanical interactions between the phases. Fiber-matrix combinations are chosen to provide the properties and stability defined by the application; however, a variety of factors from processing to chemical and mechanical compatibility must be considered in the design of a composite system. A summary of the mechanical and physical properties of selected fibers, whiskers, and matrix materials is given in Table 5.1 (3,20,45-48).

For a particular ceramic fiber and ceramic matrix combination to perform well as a composite, several compatibility requirements must be satisfied. The thermal expansion mismatch between the fibers and matrix cannot be too great because extensive cracking and damage will occur upon temperature cycling. The relative moduli of the components determine the extent to which cracking can be hindered. Generally, the fibers are stronger than the matrix materials and the goal in the fabrication of the composite is to have the fiber bear a greater portion of the load. Load distribution is a function of the components, and thus must be considered in the choice of matrix and reinforcement. Finally, the constituents must be chemically compatible with each other and their external environment at temperatures of fabrication and use.

Table 5.1. Properties of some reinforcement and matrix materials.[a]

	Density (g/cm^3)	Tensile strength (MPa)	Young's modulus (GPa)	Thermal expansion ($10^{-6}/°C$)	Fiber diameter (μm)
Fibers					
High modulus carbon	1.8	1900	530	radial 8.0	8
High strength carbon	1.8	2760	275	axial < 0	
CVD SiC monofilaments	3.2	3450	415	4.8	140
Nicalon SiC yarn	2.6	2060	220	3.1	10-15
Alumina	3.9	1400	385	8.5	20
Alumina-borosilicates:					
Nextel 312	2.5	1550	152	5.5	11
Nextel 480	3.1	1900	220	5.5	11
Nextel 440	3.1	2000	190	5.5	11
Boron monofilament	2.5	2750	400	4.7	100-200
Boron nitride	1.9	1380	90	7.5	
Boron carbide	2.4	2275	90	4.5	
Whiskers					
SiC whiskers	3.2	21000	840	4.8	0.1-0.6
VLS SiC whiskers	3.2	8400	580	5.5	6
Alumina	3.9	21000	430	8.6	
Beryllia	2.9	13000	345	9.5	
Boron carbide	2.5	14000	480	4.5	
Graphite	1.7	21000	700	2.0	
Slicon nitride	3.2	14000	380	2.8	
Matrix glasses and ceramics					
Borosilicate glass	2.3	100	60	3.5	
Soda-lime glass	2.5	100	60	8.9	
Lithium aluminosilicate glass-ceramic	2.0	150	100	1.5	
Magnesium alumino-silicate glass-ceramic	2.7	170	120	2.5-5.5	
Silica glass	2.3	120	70	0.5-8.6	
Mullite	2.8	185	145	5.3	
Si_3N_4	3.2	410	310	2.8	
SiC	3.2	310	440	4.8	
CVD SiC	3.2	1200	440	5.5	
Al_2O_3	3.9	300	400	8.5	
ZrO_2	5.7	140	250	7.6	
HfO_2	9.7	69	565	5.9	
ZrC	6.8	210	480	6.7	
B_4C	2.5	490	450	4.5	
TiB_2	4.5	1000	570	8.1	

[a]Representative values are given. There is considerable variation in the reported properties for many of the materials.

5.2 Mechanical Considerations

The prediction of the properties and behavior of a selected composite system is a formidable challenge. A composite is a heterogeneous mixture of multiple phases with differing physical, chemical, and mechanical properties. The composite properties are derived from the properties of the constituents and the interaction that occur between the components. A simple calculation of tensile stress and strain for a composite containing continuous filament reinforcement can be based on the following assumptions (24,48-52).

1. The filaments are perfectly aligned parallel to the tensile axis and surrounded by matrix.

2. Load is transferred from the matrix to the fibers by shear stresses at the interface.

3. The filaments, the matrix, and the composite are elongated equally according to Hooke's Law.

4. The fiber reinforcement is fully bonded to the matrix, and the fibers all have the same strength, size, and shape.

5. The stress on the components is determined by the modulus and the strain.

On this basis, linear expressions for the modulus and strength of a composite material have been derived from the rule of mixtures (53). The linear models are not as accurate as some of the more complex theories developed in recent years, but the mathematics is much less rigorous and general trends and relationships can be examined. The mechanical properties of the fiber and the matrix contribute to the final properties

of the composite and the contribution of each constituent is proportional to its volume fraction.

In the region of linear behavior, the relationship for stress in the composite, σ_c, is given as

$$\sigma_c = V_f\sigma_f + V_m\sigma_m \ , \tag{1}$$

where σ_f and σ_m are the strengths of the fibers and matrix, respectively, and V_f and V_m are the volume fractions of the phases. In the elastic region, the strains for the composite, matrix, and fibers are equal, $\epsilon_c = \epsilon_f = \epsilon_m$, (isostrain restriction) and the stress-strain behavior of the composite can be written as $\sigma_c = E_c\epsilon_c$, where

$$E_c = V_fE_f + V_mE_m \ , \tag{2}$$

where E is the corresponding moduli of the constituents. In polymer and metal-matrix composites, the maximum strength is reached when the ultimate strain in the fiber is achieved; thus,

$$\sigma_c = V_f\sigma_{fu} + V_m\sigma_m \ . \tag{3}$$

In this case, the fibers fracture before the matrix does [Figure 5.1(*a*)]. Ceramic composites differ significantly in that the moduli of the constituents are much closer than in the aforementioned systems and the failure strain of the fibers is generally higher than that of the matrix.

ORNL-DWG 88-7126

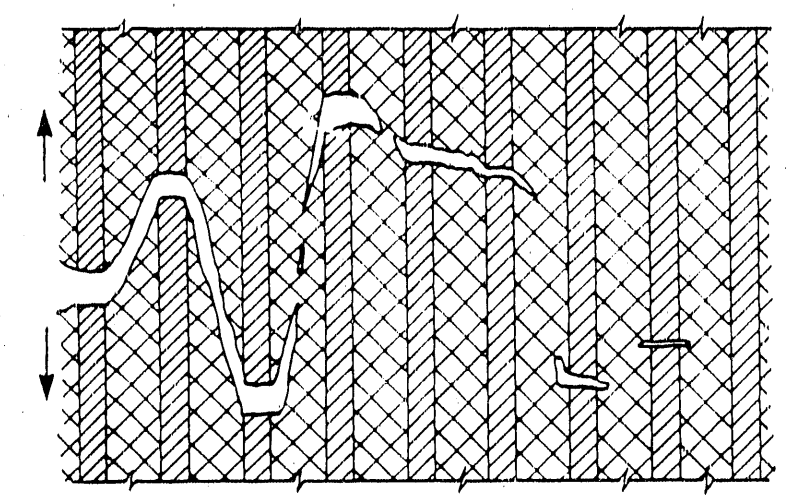

(a) $\epsilon_{mu} > \epsilon_{fu}$

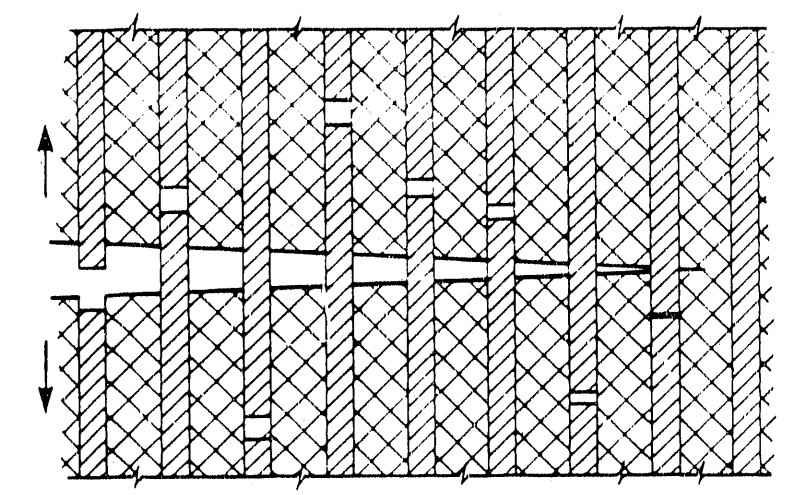

(b) $\epsilon_{mu} < \epsilon_{fu}$

Figure 5.1. The influence of failure strain on the fracture mode of a fiber-reinforced composite.

Therefore, the maximum strength of a ceramic-ceramic composite is attained when

$$\sigma_c = V_f\sigma_f + V_m\sigma_{mu} \quad . \tag{4}$$

As the strain in a ceramic composite is increased, σ_m will reach σ_{mu} before σ_f reaches σ_{fu}. Because the ratio of stress carried by the fibers and matrix, respectively, is E_fV_f/E_mV_m, the equation can be rearranged to give

$$\sigma_c = \sigma_{mu}[1 + V_f(E_f/E_m - 1)] \quad . \tag{5}$$

At this stress, the first matrix cracks will develop and load transfer to the fibers begins [Figure 5.1(*b*)]. Once matrix fracture is complete, and if the fibers are able to support the entire load, the ultimate strength of the composite becomes

$$\sigma_{cu} = V_f\sigma_{fu} \quad . \tag{6}$$

Equation (5) demonstrates the importance of the relative elastic moduli of the components. Matrix cracking will occur at a much higher stress in a system combining high-modulus fibers with a low-modulus matrix than for high-stiffness fibers in a stiff matrix. Although high-moduli matrices fracture at lower stresses, these systems should not be discarded.

Equation (6) shows that the strength of the composite is determined by the ultimate strength of the fiber reinforcement and not simply matrix failure stress.

The previous equations describing the elastic behavior of a composite assume that the fibers are continuous and unidirectionally aligned in the direction of the applied stress. An allowance can be made for fibers that are not aligned in the stress field (50,51). The contribution of a fiber is obviously reduced as it is rotated out of the direction of the applied stress or strain. A correction factor X can be added to the equations for stress and modulus. The value of X is approximately 0.38 for a composite containing randomly oriented fibers lying in one plane (two-dimensional reinforcement). Accounting for the misalignment of the reinforcement, the expressions describing stress in a composite becomes

$$\sigma_c = XV_f\sigma_f + V_m\sigma_m \quad . \tag{7}$$

Many ceramic matrix composites contain residual porosity that occurs during processing. Porosity reduces both strength and modulus in ceramics (54-56). The presence of pores in a structure reduces cross-sectional area exposed to a load, and the voids act as stress concentrators. The strength of a ceramic body decreases exponentially with increased porosity. The equation,

$$\sigma_p = \sigma_o \exp(-np) \quad , \tag{8}$$

was derived from extensive testing of alumina specimens with known levels of porosity. In the equation, p is the volume fraction of porosity and n is a geometrical factor between 4 and 7. The effect of voids on the Young's modulus of ceramics has been evaluated in similar experiments. The voids are assumed to possess zero Young's modulus, thereby altering the elastic properties of a material. The influence of closed porosity in a continuous matrix is described by the expression

$$E_p = E_o(1 - 1.9p + 0.9p^2) \quad , \tag{9}$$

where, again, p is the volume fraction of porosity, E_p is the porosity corrected modulus, and E_o is the modulus for a fully dense material.

5.3 Thermomechanical Compatibility

Because ceramics are inherently brittle and thus lack ductility, efforts must be maintained to minimize residual thermal stresses in a ceramic composite by appropriately matching fiber and matrix thermal expansions. Differences in thermal expansion between fiber and matrix can cause severe damage, and this factor has rendered a number of potential composite systems unacceptable for high-temperature use. Thermal expansion mismatches result in very large stresses in the fiber and matrix, and thermal cycling can lead to fiber or matrix failure.

Thermal expansion effects can lead to high stress levels at the fiber-matrix interface (5,57-59). The effect is dependent on the degree of bonding that is present at the fiber-matrix interface. If the bond is strong, the stresses can fracture the fibers or matrix; if the bonding is weak, separation of the fibers and matrix will occur, resulting in a loss

of reinforcement. There are two cases to consider when selecting a fiber-matrix combination: (1) the coefficient of thermal expansion of the fibers is greater than that of the matrix ($\alpha_f > \alpha_m$) and (2) the opposite case, in which the expansion coefficient of the matrix is greater than that of the fibers ($\alpha_m > \alpha_f$). Defining $\Delta\alpha = (\alpha_m - \alpha_f)$, the thermal stresses for a given unidirectionally aligned fiber composite are briefly summarized.

When ($\alpha_m > \alpha_f$), the matrix will contract more than the fibers upon cooling [Figure 5.2(*a*)]. The matrix will radially compress the fibers, increasing the degree of bonding and friction at the fiber-matrix interface and, in extreme instances, could crush the reinforcement. The fibers function to keep the matrix in tension in the axial direction. If the mismatch is large enough, the failure strain of the matrix will be exceeded and cracks will develop in the matrix in a direction perpendicular to the fiber axes.

When the thermal expansion cefficient of the fibers is greater than that of the matrix, ($\alpha_m < \alpha_f$),, the fibers will shrink away from the matrix upon cooling [Figure 5.2(*b*)]. If the fiber-matrix bonding is weak, the fiber will separate from the matrix in the radial direction so that the frictional force along the interface is zero. This results in insufficient load transfer from the matrix to the fibers for the fibers to provide effective reinforcement. If the components are well bonded, and the fibers are strong and do not fail, a compressive stress will be induced in the matrix. This will increase the overall strain necessary to initiate failure in the matrix and, hence, will result in an increase

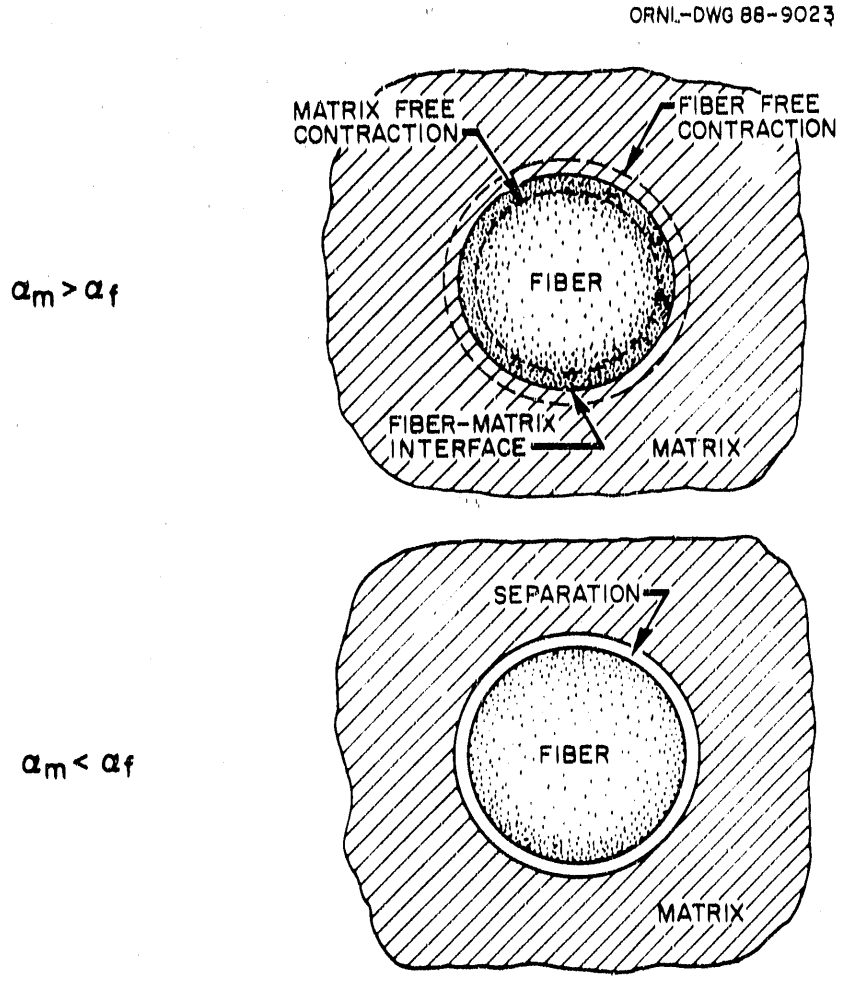

Figure 5.2. The effects of the thermal expansion mismatch on the fiber-matrix interface.

in strength. Conversely, the fibers will be subjected to axial tensile stresses, and if the fibers are unable to withstand the stress, they will fracture.

The expressions describing these thermally induced stresses and strains for a unidirectionally reinforced composite can be derived by considering a composite element consisting of a single fiber surrounded by a tube of matrix (24,57,60). Assuming perfect bonding between the fiber and matrix, it can been shown that the strain induced in the fiber by thermal contraction of the matrix is given by

$$\epsilon_f{}^{th} = -E_m V_m \Delta\alpha \Delta T / E_c \quad , \tag{10}$$

and the strain in the matrix by

$$\epsilon_m{}^{th} = E_f V_f \Delta\alpha \Delta T / E_c \quad , \tag{11}$$

where E are the corresponding moduli of the composite and its constituents and ΔT is the temperature change. A negative value of ϵ^{th} designates compression, and conversely, tensile strains are positive.

If the value of $\epsilon_f{}^{th}$ is negative, the fibers will be compressed by the matrix, thus increasing interfacial frictional stresses. If positive, the fibers will contract away from the matrix, thus no interfacial bonding will exist and reinforcement is lost. If $\epsilon_m{}^{th}$ is negative, the matrix will be in compression and cracking will be inhibited. If positive, the matrix will be in tension, and if $\epsilon_m{}^{th} > \epsilon_{mu}$, the matrix will microcrack upon cooling.

The stress in the matrix resulting from an applied strain was given in Eq. (5). Remembering that $\sigma = E\epsilon$ and substituting Eq. (5) into Eq. (11), the thermal mismatch stress in the matrix can be calculated (61,62) from

$$\sigma_m{}^{th} = [E_f V_f \Delta\alpha \Delta T]/[1 + V_f(E_f/E_m - 1)] \ . \qquad (12)$$

Again it can be shown that if $\Delta\alpha$ is positive and ΔT is large enough, the thermal stress will exceed the ultimate stress of the matrix and the matrix will fail. Table 5.2 presents the calculated matrix thermal stresses for a set of fiber-matrix combinations.

The expressions for interfacial pressure (P) or radial stress at the fiber-matrix interface can be derived as for the matrix. The resulting relationship is

$$\sigma_f{}^{th} = P = [E_m V_m \Delta\alpha \Delta T]/[1 + V_m(E_f/E_m - 1)] \ . \qquad (13)$$

Frictional stress transfer occurs when the value is negative, thus α_f must be less than α_m. Table 5.3 contains the calculated interfacial pressures for some selected fiber-matrix combinations. The axial stress experienced by the fibers is given by the the same equation; however, thermal expansion in many fibers is anisotropic with radial expansion coefficients differing from the axial values (Table 5.3).

From these relationships, it is shown that fiber-matrix thermal expansion differences must be kept to a minimum. The difference should not be negative because the fibers will debond from the matrix and

Table 5.2. Thermally induced axial stress (in MPa) in the matrix upon cooling from 1275 K to room temperature.[a]

Fiber	Matrix					
	Alumina (8.5)	LAS glass (1.5)	CVD SiC (4.8)	Si_3N_4 (3.0)	TiB_2 (8.1)	Mullite (5.3)
Alumina (8.5)	0.0	-887.8	-895.0	-1361.1	-123.4	-510.9
Boron (4.7)	1071.6	-410.2	24.7	-429.5	1076.2	97.1
High-modulus carbon fibers (0.0)	2945.5	210.1	1415.7	909.8	3241.4	960.1
Low-modulus carbon fibers (0.0)	2207.8	185.1	1102.2	703.9	2338.9	817.4
Nextel (2.0)	916.5	-44.1	368.6	133.3	909.7	339.3
Nicalon (3.1)	897.2	-155.7	260.6	-15.6	887.8	254.2

[a]Numbers in parentheses are $\alpha(10^{-6}/°C)$.

Table 5.3. Stresses induced in the fiber by thermal expansion mismatch upon cooling from 1275 K to room temperature.[a]

Matrix	Fiber				
	Alumina (8.5)	Boron (4.7)	Carbon (0.0)	Nextel (2.0)	Nicalon (3.1)
	Axial stress in fiber (in MPa)				
Alumina (8.5)	0.0	-714.4	-1498.1	-611.0	-680.9
Lithium aluminosilicate glass-ceramic (1.5)	591.9	273.5	-124.4	29 4	111.8
Mullite (5.3)	340.6	-64.7	-550.6	-226.2	-185.2
CVD SiC (4.8)	596.7	-16.5	-746.4	-245.7	-195.7
Silicon nitride (3.0)	907.4	286.3	-476.8	-88.8	11.7
Titanium diboride (8.1)	82.2	-717.5	-1590.3	-606.5	-680.3
	Interfacial pressure (in MPa)				
Alumina (8.5)	0.0	-550.7	-76.9[b]	-728.5	-651.4
Lithium aluminosilicate glass-ceramic (1.5)	302.3	137.4	284.0[b]	19.8	64.8
Mullite (5.3)	188.7	-35.1	161.8[b]	-172.7	-119.1
CVD SiC (4.8)	603.3	-16.0	545.5[b]	-338.0	-222.1
Silicon nitride (3.0)	661.3	201.2	621.1[b]	-95.5	10.2
Titanium diboride (8.1)	79.5	-658.4	-21.0[b]	-849.0	-763.0

[a]Numbers in parentheses are $\alpha(10^{-6}/°C)$.

[b]Radial expansion in carbon fibers = $8.0 \times 10^{-6}/°C$.

reinforcement will be lost. The ideal situation is one in which $\Delta\alpha = 0$ or is slightly positive, therefore ensuring interfacial friction and efficient load transfer (Figure 5.3). For $\Delta\alpha > 0$, the expansion of the fibers must be less than in the matrix ($\alpha_f < \alpha_m$), but this condition will place the matrix in tension. Recalling that the thermally induced strain cannot exceed the ultimate strain of the matrix, the minimum value of α_f is restricted to

$$\alpha_m + [\epsilon_{mu}/\Delta T](1 - E_m/E_f) < \alpha_f \ , \tag{14}$$

where ϵ_{mu} is the failure strain of the matrix. Therefore, the thermal expansion coefficient of the fibers must be in the range

$$\alpha_m + [\epsilon_{mu}/\Delta T](1 - E_m/E_f) \leq \alpha_f \leq \alpha_m \ , \tag{15}$$

to produce a useful composite material.

5.4 Thermochemical Considerations

Chemical reactions at the fiber-matrix interface have been shown to play a major role in reducing the strength of a composite. The formation of brittle zones in ceramic fiber-reinforced metal-matrix composites generally decreases the strength of the material. Oxidation embrittlement has been noted in glass-matrix composites containing untreated SiC fibers (19,20,63,64). Short-term exposure of ceramic fiber-reinforced glasses to elevated temperatures in air resulted in increased fiber-matrix bonding and, ultimately, brittle behavior upon testing at room temperature.

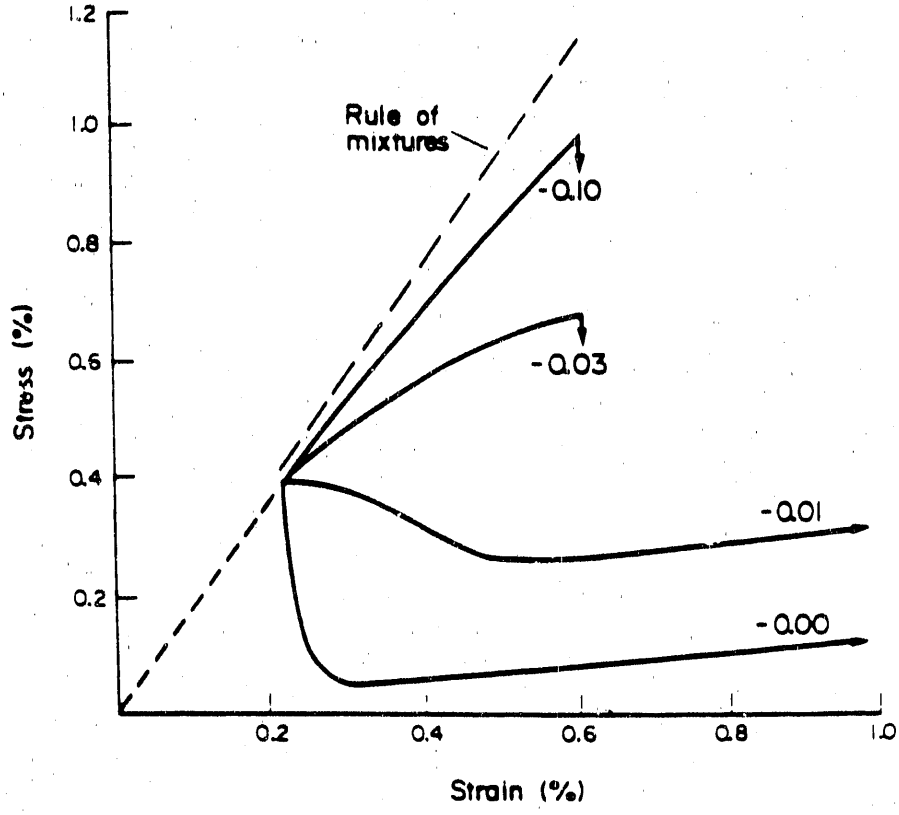

Figure 5.3. Effect of residual stress on the stress-strain behavior of carbon-epoxy composites. The solid curves start at the slip point and residual stresses (GPa) are marked on the curved. *Source*: M. R. Piggot, "Reinforcement Processes," pp. 83–97 in Load Bearing Fibre Composites, Chapter 5, Pergamon Press, Oxford, England, 1980.

The selection of the components of a composite is initially based on mechanical and physical properties of the individual constituents. When the materials are combined to form a composite, the system generally will not be at thermodynamic equilibrium, and thus, a driving force to change the system exists. Thermodynamic data and calculations allow prediction of the final equilibrium state of the composite material. These calculations can also be used to determine possible interactions that may occur between components during processing.

At relatively high temperatures (> 1000 K), chemical reactions proceed rapidly and the equilibrium state is attained in a relatively short time. Equilibrium conditions can be predicted by employing basic thermodynamic concepts to determine the compositional state of a given system having the minimum free energy (65). Numerous phases will be present in a system at elevated temperatures; therefore, the numerical analysis becomes extremely complicated. Computer programs have been developed to simplify the analytical process. The majority of the codes are based on SOLGAS, a program created to examine systems containing gaseous and pure condensed phases (65). SOLGAS has been modified to include pure solids, liquids, and gases and condensed phase solutions. The program has evolved over the years into SOLGASMIX (66,67), which has the ability to perform the calculations necessary to examine numerous combinations of compounds and system conditions of temperature, pressure, or volume.

Kinetic data including diffusivities are equally as important in the analysis because these can be used to predict the rate at which the system will change (68-70). It is obvious that chemical interactions

will affect the interface and, thus, the behavior of a composite. Increased activity can lead to enhanced bonding, fiber property degradation, and, finally, composite-strength reduction. All of these factors will influence the thermal stability of the composite product, but the calculations are only rough estimates.

6. FIBER-MATRIX INTERFACES

6.1 Introduction

The chief function of the interface is to transfer load across the fiber-matrix boundary. Dow (71) and others have developed analytical models to evaluate the stresses generated at the interface of a composite. Their observations were concerned with load transfer across the interface when either the fiber or matrix component was subjected to a uniaxial tensile load. Given a fiber of finite length, relationships for interfacial shear in terms of applied load and the properties and dimensions of the individual components were developed.

Much of the work was devoted to explaining behavior of fiber-reinforced plastics (72) or metals (2,71,73,74) in which many of the basic assumptions for elastic or plastic behavior of materials hold true, simplifying the analysis. Metals and polymers are generally soft and yielding; however, this is not true for ceramics. Ceramic materials are hard and stiff, possessing high moduli and low failure strains and Poisson's ratios. The elastic-plastic response of the majority of these materials is extremely limited; therefore, the applicability of these expressions in explaining composite behavior is narrow.

To further develop and improve ceramic-ceramic composites, it is essential to understand the mechanisms that control the mechanical behavior, especially the strength and toughness, of ceramic-ceramic systems (5,11,12,14,15,75-78). Although the relative moduli of the components are important, it is widely regarded that microcracking, fiber debonding, and particularly, fiber pull-out are the key contributors to the toughness of these composites. These mechanisms are controlled by

fiber-matrix bonding; thus, a fundamental understanding of the fiber-matrix interface is necessary to design and produce composites that possess the optimum combination of strength and fracture resistance.

The study of interfaces is not limited to the mechanical aspects, but is interdisciplinary, a combination of materials evaluation and mechanical relationships. A practical correlation relating interfaces to composite properties is impossible without an understanding of the mechanical, physical, and chemical interactions that are present in a given system. Chemical, physical, and mechanical bonding are present at the interfaces in all composite systems. These factors combined with the mechanical properties of the individual components can be used to explain the observed behavior of a multicomponent composite material.

6.2 Role of the Interface

The mechanical properties of filamentary composites are influenced strongly by the fiber-matrix interface. The interfacial bond affects matrix-cracking and composite-fracture behavior (57,78-80). For composites having a very strong interfacial bond, a crack propagating in the matrix will pass undisturbed through the fibers and the composite will fail in a brittle manner, much the same as the unreinforced matrix material does (Figure 6.1). For composites having poorly bonded interfaces, the fracture process begins progressively with debonding at the fiber-matrix interface, followed by subsequent matrix failure, fiber slip and pull-out, and finally, fiber failure (81,82). These energy-absorbing mechanisms all contribute to improve fracture toughness and are controlled by the strength of the fiber-matrix bond.

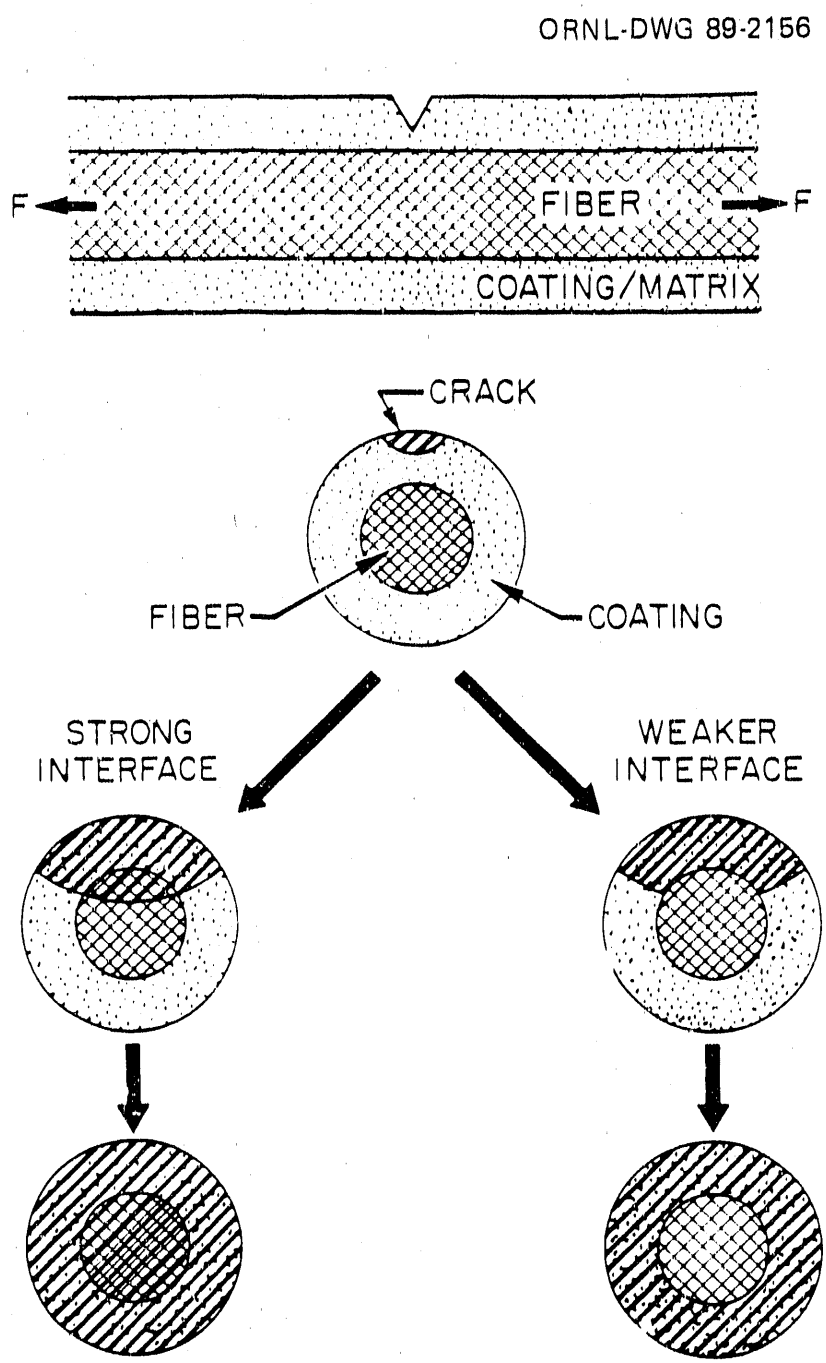

Figure 6.1. The effects of interfacial bonding on the behavior of a crack as it intersects the fiber-matrix boundary.

In the analysis of the mechanical relationships that control the performance of fiber-reinforced materials, it was assumed that a perfect bond exists between the fiber reinforcement and matrix. The condition ensures complete load transfer in the system and simplifies the calculations. The formulations indicate that a high ratio of fiber to matrix Young's modulus, E_f/E_m, is desirable for ceramic matrix composites, where the matrix has the lower ultimate strain. As noted earlier, the moduli of the components of ceramic-ceramic composites are much closer than in polymer- and metal-matrix systems; therefore, it is obvious that these expressions do not realistically explain the behavior of many brittle matrix composites. It has been demonstrated that the failure strain of the matrix can be increased by the addition of fiber reinforcement and that matrix fracture does not necessarily constitute the upper limit of load capacity of the composite.

The range in which the linear representations for stress and strain are accurate is limited by the condition of matrix fracture. The first deviation from linear behavior occurs immediately upon matrix failure, and beyond the point of matrix fracture, the mechanical behavior of a composite is governed by the properties of the fibers and by the adhesion and frictional stresses at the fiber-matrix interface (Figures 6.2 and 6.3). The effect of the fiber-matrx bond on the failure strain of the matrix in a composite has been examined. Aveston, Cooper, and Kelly (81,82) developed a model relating the failure strain of the matrix to material and composite parameters.

The ACK (Aveston, Cooper, and Kelly) model is based on energetics and employs an energy balance to predict the point of matrix failure

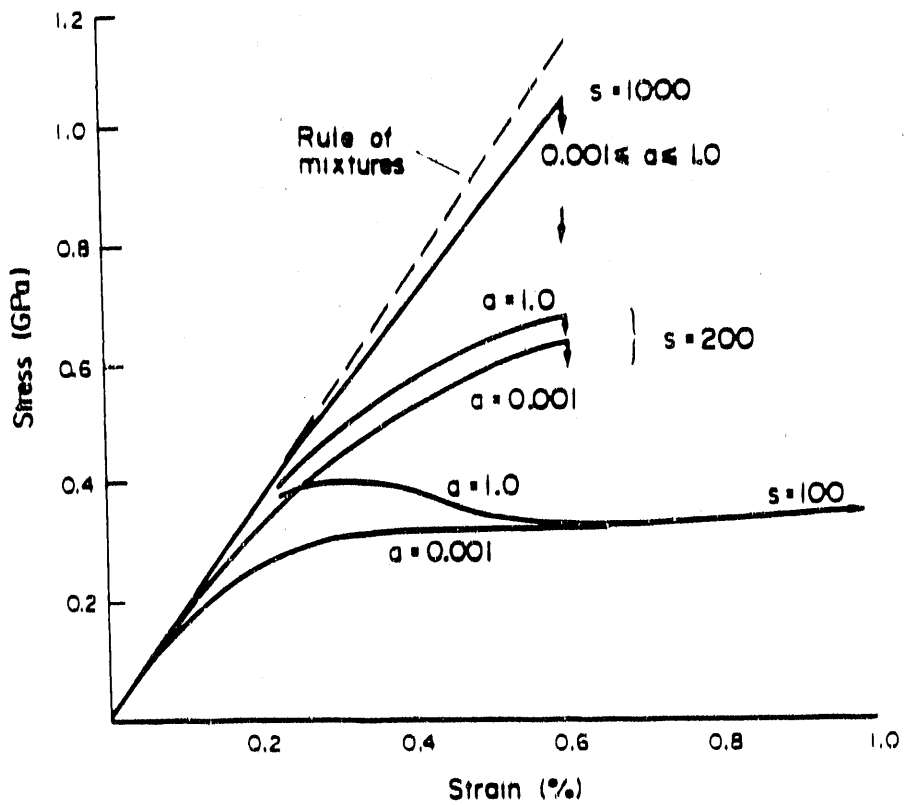

Figure 6.2. Effect of adhesion on the stress-strain behavior of carbon-epoxy composites. Corresponding adhesion coefficients and aspect ratios are given. *Source*: M. R. Pigor, "Reinforcement Processes," pp. 83-97 in *Load Bearing Fibre Composites*, Chapter 5, Pergamon Press, Oxford, England, 1980.

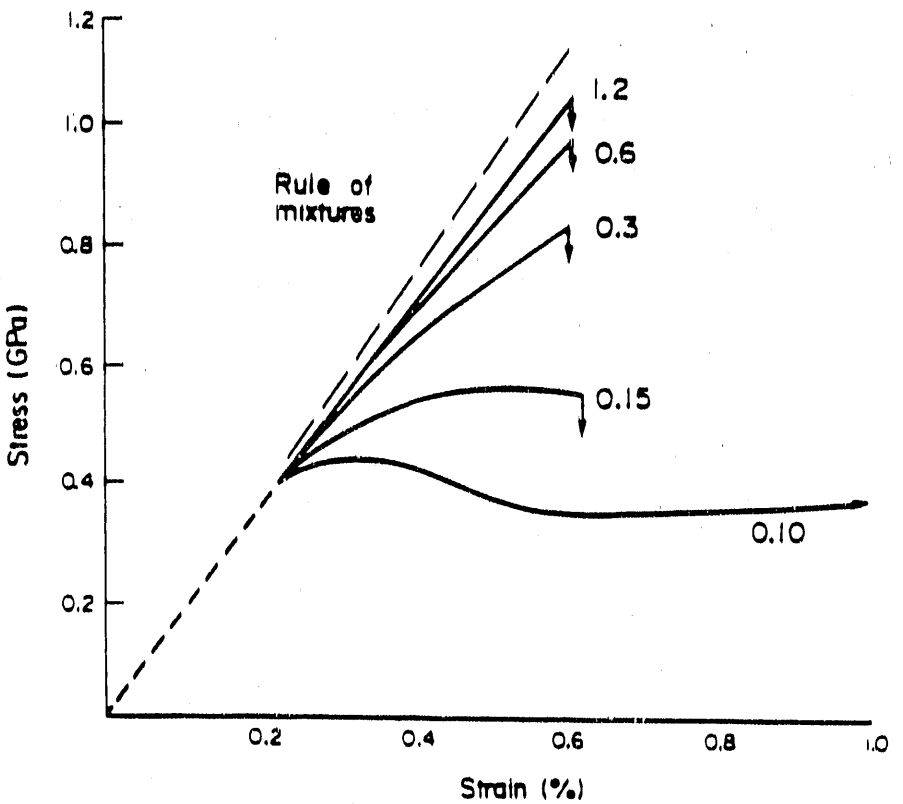

Figure 6.3. Effect of friction coefficient on the stress-strain behavior of carbon-epoxy composites. The solid curves start at the slip point and the friction coefficients are marked on the curves. *Source*: M. R. Piggot, "Reinforcement Processes," pp. 83–97 in *Load Bearing Fibre Composites*, Chapter 5, Pergamon Press, Oxford, England, 1980.

during the loading of a composite. In single-phase materials, the work of fracture is determined by the applied forces, the strain energy of the material, and the fracture surface energy. In composites, however, there are the additional phenomena of strain energy of the fibers and the work done in debonding the fibers and pulling them from the matrix. These additional factors will contribute to increase the strain at which the matrix in a composite will begin to crack.

The influence of the interfacial shear stress τ_i on the failure strain of the matrix, ϵ_{muc}, is shown in the expression

$$\epsilon_{muc} = [(24\tau_i\gamma_m E_f V_f^2)/(E_c E_m^2 r V_m)]^{1/3} , \tag{16}$$

where γ_m is the fracture energy of the matrix and r is the fiber radius. If adequate bonding exists, the presence of higher-strength fibers will suppress cracking in the matrix, resulting in an increase in ϵ_{mu} to ϵ_{muc}. Conversely, weak bonding at the fiber-matrix interface will result in a lower strain tolerance in the matrix.

Upon matrix fracture, load is transferred to the fibers, and if the fibers are strong enough, they will support the load. The fibers must be able to bear the entire load held by the composite at the point of matrix failure; therefore,

$$\sigma_f V_f > \sigma_{mu} V_m + \sigma_f' V_f , \tag{17}$$

where σ_f' is the stress on the fibers at matrix fracture. If the failure strain of the fibers is sufficiently large, a further increase in load

will result in the matrix being traversed by a set of cracks such that the lengths of the cracks is dependent on the value of r_i. Single fracture occurs if the fibers are unable to sustain the load when the matrix fails or if the value of r_i is large and $E_f \varepsilon_{muc} \geq \sigma_{fu} V_f$. [See Eq. (6).] Therefore, interfacial forces not only determine the limit of linear behavior for a composite, they influence the mechanical response of a composite until ultimate failure.

7. CHARACTERIZATION OF THE FIBER-MATRIX INTERFACE

Quantitative analysis of the interfacial bond strength and frictional stresses and detailed characterization of the chemical interactions at the fiber-matrix boundary are essential to begin relating composite properties to interfaces. When the nature of the fiber-matrix interface is fully understood, interfacial pretreatments can be employed to control fiber-matrix bonding and interaction and, ultimately, the mechanical behavior of composite materials.

7.1 Quantitative Analysis of Forces at the Interface

Numerous methods have been developed to quantify the strength of interfacial bonding in fiber-reinforced composites (83-88). These have involved either pushing or pulling on individual fibers embedded in a continuous matrix and determining the required forces. Such tests permit a quantitative determination of the bond strength and interfacial frictional stresses, which are derived from relatively simple load and displacement relationships.

7.1.1 Indentation techniques

Several indentation methods for measuring interfacial bonding forces have been examined (85-88). These techniques involve using a micro-hardness indentor to apply a force to the end of a fiber embedded in a matrix. The bond strength can be calculated from the applied load and the displacement of the fiber.

In the method developed by Marshall (88), a load is applied to the end of a single fiber embedded in a matrix and having an orientation perpendicular to a prepared surface (Figure 7.1). An analysis of the forces needed to displace a fiber in a thin specimen yields

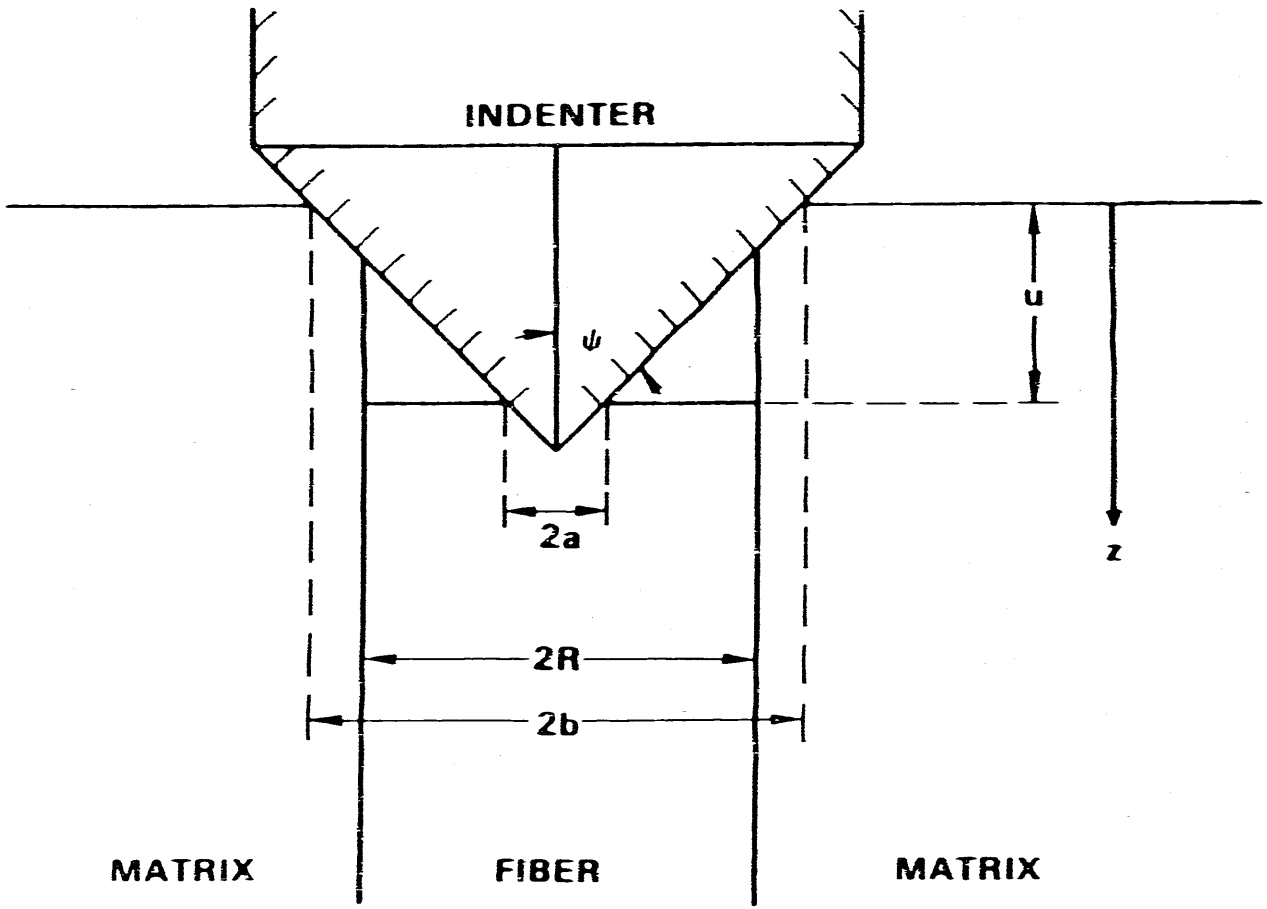

Figure 7.1. Schematic of indentation method for measurement of fiber-matrix frictional stress. *Source*: D. B. Marshall, "An Indentation Method for Measuring Matrix-Fiber Frictional Stresses in Ceramic Components," *Comm. Amer. Ceram. Soc.* C259-60 (December 1984).

$$F = 2\pi R t \tau \quad , \tag{18}$$

where τ is the frictional stress, t is the thickness of the sample parallel to the direction of the fibers, and R is the fiber radius. This relationship holds for thin specimens in which the thickness of the sample is less than the sliding distance of the fiber. The fiber will thus simply be pushed out of the opposite surface when a load is applied. The analysis becomes much more complex if the thickness of the specimen is larger than the sliding distance; however, it can be approximated that the given relationship can be applied to thicker specimens if the thickness of the specimen is much greater than the sliding distance. The frictional stress can then be calculated from the displacement of the fiber u, resulting from the load imposed by the diamond indentor. The frictional stress is

$$\tau_i = F^2/4\pi^2 u R^3 E_f \quad , \tag{19}$$

where E_f is the Young's modulus of the fiber and u is the fiber displacement. The value of u can be determined from the indent impression dimensions a and b and the indentor angle 2ψ as shown in Figure 7.1,

$$u = (b - a) \cot \psi \quad . \tag{20}$$

The force F supported by the fiber can be obtained from calculating the hardness impressions on the fiber,

$$F = 2a^2H , \qquad (21)$$

where H is the hardness of the fiber.

7.1.2 Tensile testing

Although indentation techniques can promote a better understanding of the nature of the interface and its role in the behavior of fiber-reinforced materials, these "push tests" are complicated by several factors. The Poisson expansion of the fiber as a result of compressive loading, the nature of the indentor penetration into the fiber end, and the intricacies of a completed composite specimen all add to the complexity of the analysis. In addition, the samples must first be cut, ground, and polished prior to testing, most likely disturbing the fiber-matrix interface. It has been postulated that a less-complex method that employs a simple tensile test could be developed to examine interfacial phenomena.

In general, the fibers in a ceramic-ceramic composite have a higher strain-to-failure than that of the matrix, and it is assumed that the ceramic matrix materials are essentially inelastic. When a ceramic-ceramic composite is stressed, the brittle matrix will fail before the fibers fail. In the event of matrix failure, the load is transferred from the matrix to the fibers. As loading continues, the fibers will strain and multiple cracking of the matrix will occur.

During mechanical property evaluation of Nicalon fiber-reinforced-SiC matrix composites fabricated using FCVI techniques, segmental fracturing of the fiber coatings on the tensile side of flexure specimens was observed. An example of this fracture phenomenon is shown

in Figure 7.2. Based on the multiple-matrix-cracking concepts described by Aveston, Cooper, and Kelly (81,82) and some recent work by Drzal (84) on interfaces in polymer matrix-graphite fiber composites, a simple tensile test to determine interfacial frictional stress was devised. In the test, a thin coating is deposited on a section of a single filament. The filament is then gripped on the uncoated ends, and a tensile force is applied. Load transfer to the coating from the fiber can only occur across the fiber-matrix interface. As loading continues, the axial stress in the coating increases until the coating fractures circumferentially (Figure 7.3). Continued application of the load results in repeated fracture of the coating into uniform lengths. The lengths of these fragments is dependent on the interfacial frictional stress, the strength of the coating, and the thickness of the film.

From an equilibrium of forces between the axial stress in the coating σ_{cg} and the interfacial shear stress τ_i acting on length ℓ, a simple relationship can be derived:

$$\sigma_{cg} = F/A_{cg} \ , \tag{22}$$

where F is the applied force and A_{cg} is the area of the coating given by $A_{cg} = \pi \ (d_c^2 - d_f^2)/4$. The diameter of the coating is d_c, and the diameter of the fiber is d_f. The shear stress at the interface is

$$\tau_i = F/A_f \ , \tag{23}$$

ORNL-PHOTO 6866-86

Figure 7.2. Segmental fracture of coatings on tensile side of flexure specimens.

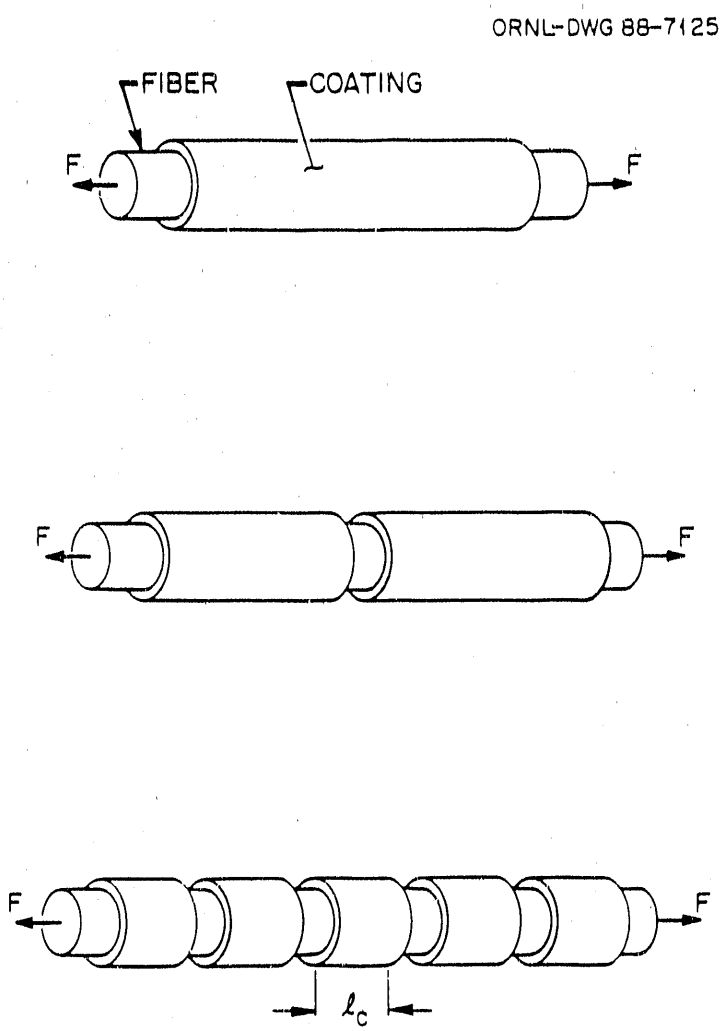

Figure 7.3. The sequence of coating fracture as loading is increased.

where A_f is the surface area of the fiber, $A_f = \pi d_f \ell$. Setting the forces to be equal

$$\sigma_{cg} A_c = \tau_i A_f \ , \tag{24}$$

$$\sigma_{cg} \pi (d_c^2 - d_f^2)/4 = \tau_i \pi_d f \ell \ , \tag{25}$$

and solving for shear,

$$\tau_i = \sigma_{cg} (d_c^2 - d_f^2)/4 d_f \ell_c \ , \tag{26}$$

where ℓ_c is the critical length of a fracture segment.

From the interfacial shear strength equation, it can be concluded that high shear stress results in short critical lengths, whereas low shear stress results in longer critical lengths. To examine the feasibility of this approach, thin coatings are applied to the center section of individual filaments using CVD techniques. The fibers can then be loaded in tension, and fracture phenomena observed.

An alternative approach to derive the relationship between interfacial shear stress and the length of the fracture segment is to utilize the established ACK model for multiple matrix fracture. The conditions for multiple fracture were given in Eq. (17), and as described, once matrix fracture is initiated, the load supported by the composite is transferred to the fibers. If the failure strain of the fibers is sufficiently large, the fibers will be able to sustain the load and, as loading continues, the matrix will successively fracture into

shorter lengths. Fragmentation of the matrix continues until the segments reach a critical length between ℓ and 2ℓ. The length ℓ is determined by the distance over which the straining fiber passing through the matrix can transfer a load to the matrix (by means of a shear force at the interface) sufficient to break the matrix.

In the regions of the matrix between cracks, an area in the center exists where the stresses are constant while slip is occurring over some distance near the face of the crack (Figure 7.4). In the regions of constant stress, the rate of load transfer is dependent on the interfacial shear stress and the contact area between the fibers and the matrix. A simple force balance yields

$$N\pi d\tau_i \ell = \sigma_{mu} V_m \ , \tag{27}$$

where N is the number of fibers per unit area or $N = V_f/(\pi d_f^2/4)$. Solving for ℓ, we have

$$\ell = V_m \sigma_{mu} d_f / 4 V_f \tau_i \ . \tag{28}$$

This is the minimum length over which sufficient load will be transferred to the matrix and exceed σ_{mu}, forming another crack. If the composite is a coated filament, then the volume of fiber is given as $\pi d_f^2 \ell/4$, the volume of the matrix (coating) is $\pi(d_{cg}^2 - d_f^2)\ell/4$, and τ_i is given by

$$\tau_i = \sigma_{mu}(d_{cg}^2 - d_f^2)/4 \ d_f \ell_c \ . \tag{29}$$

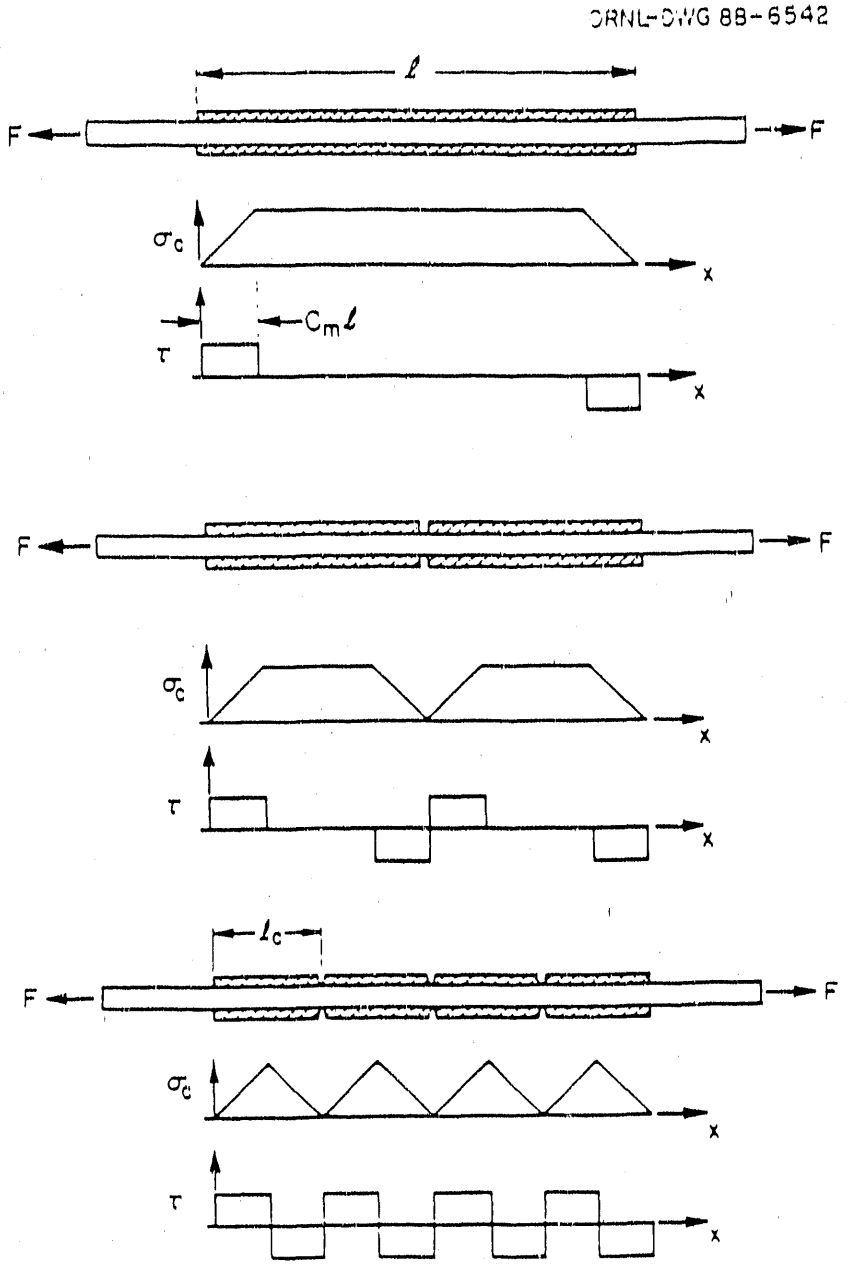

Figure 7.4. Tensile and shear stress diagrams for multiple-matrix fracture as loading of the fiber is increased.

The multiple-matrix fracture condition set by Eq. (17) reveals that the method is largely dependent on the volume of the matrix, thus on coating thickness. If the coating is too thick, single fracture will occur. The critical volume fraction of fiber and matrix for the transition from single to multiple fracture are shown schematically in Figure 7.5. The plot demonstrates that high-volume fractions of fiber are necessary for multiple fracture; thus, thin coatings are necessary for this technique to be properly implemented. Figure 7.6 graphically depicts the condition for multiple-matrix fracture for a coated Nicalon individual filament.

The materials being considered are brittle ceramics. It is assumed that the fibers and matrix will possess very limited strain tolerance; thus, fracture will occur over a small range of strain. The radial and tangential stresses induced by the contracting matrix as a result of Poisson effects can be assumed to be negligible. The expressions for stresses and strains in the matrix and fiber can be derived using the fiber-sheath model (89-92) as shown in Figure 7.7. When a single continuous fiber embedded in a matrix is stretched in a direction parallel to the fiber, tractions arise across the interface as a result of the difference in Poisson's ratios of the fiber and matrix. Assuming the fiber and matrix are circularly symmetric, the interfacial traction is a normal stress (90) σ_P given by

$$\sigma_P = [2\epsilon(\nu_m - \nu_f)V_m]/[(V_m/k_f) + (V_f/k_m) + (1/G_m)] \ , \qquad (30)$$

where k is the plane-strain bulk modulus and G_m is the shear modulus of the matrix. The stress at the interface caused by matrix contraction is

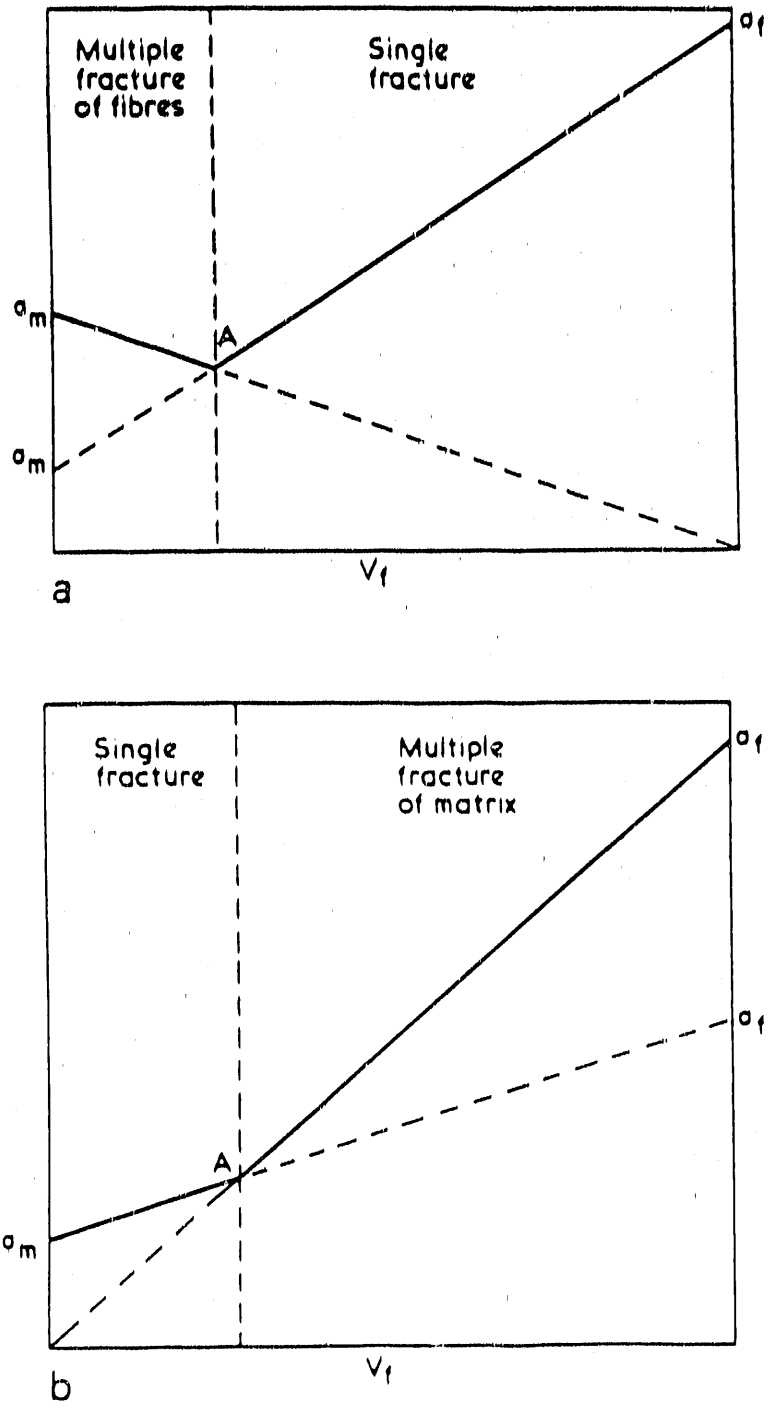

Figure 7.5. Conditions under which multiple-matrix fracture occurs: (*a*) brittle fiber, ductile matrix and (*b*) ductile matrix, brittle fiber. *Source*: J. Averson, G. A. Cooper, and A. Kelly, "Single Multiple Fracture: The Properties of Fiber Composites," pp. 15–26 in *National Physics Lab Conference Proceedings*, November 1971.

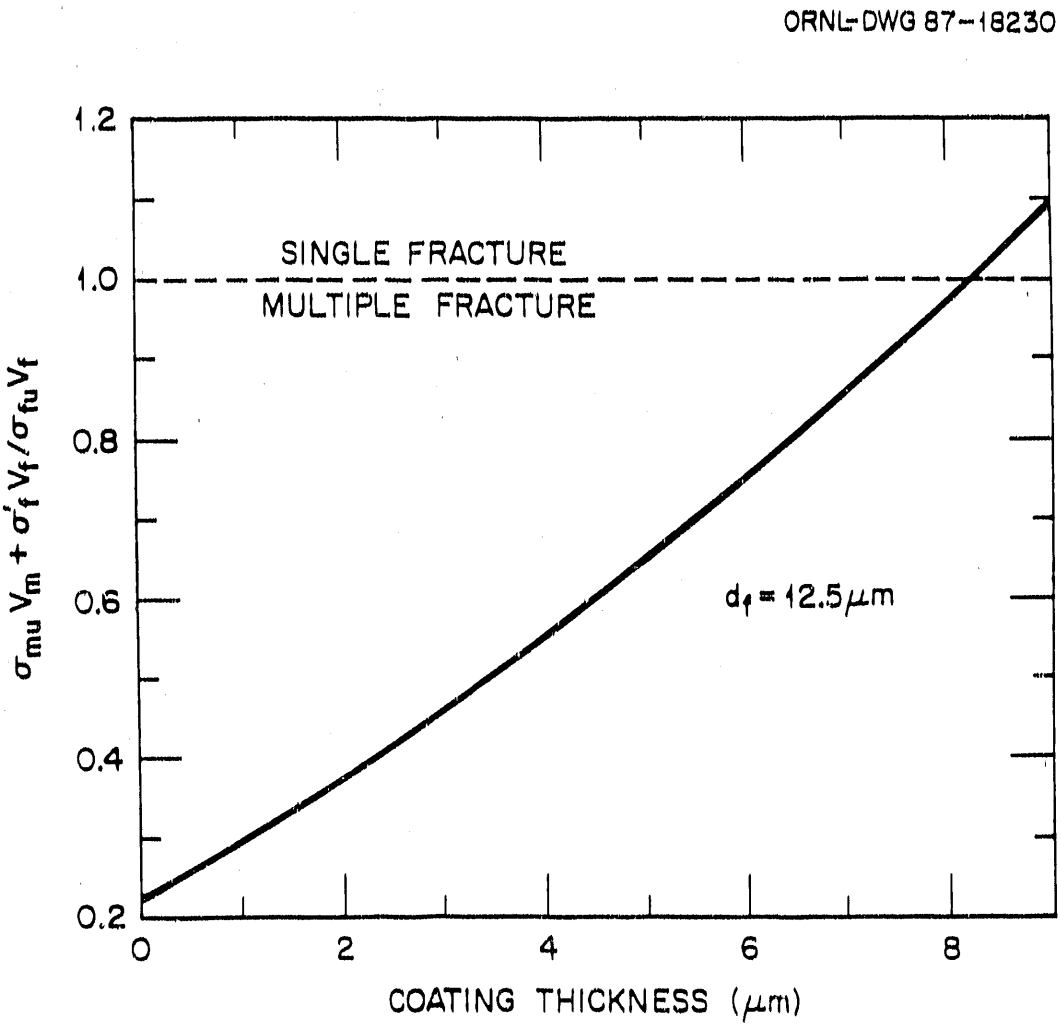

Figure 7.6. Multiple-matrix fracture condition versus coating thickness for a coated individual Nicalon filament.

ORNL-DWG 87-18231

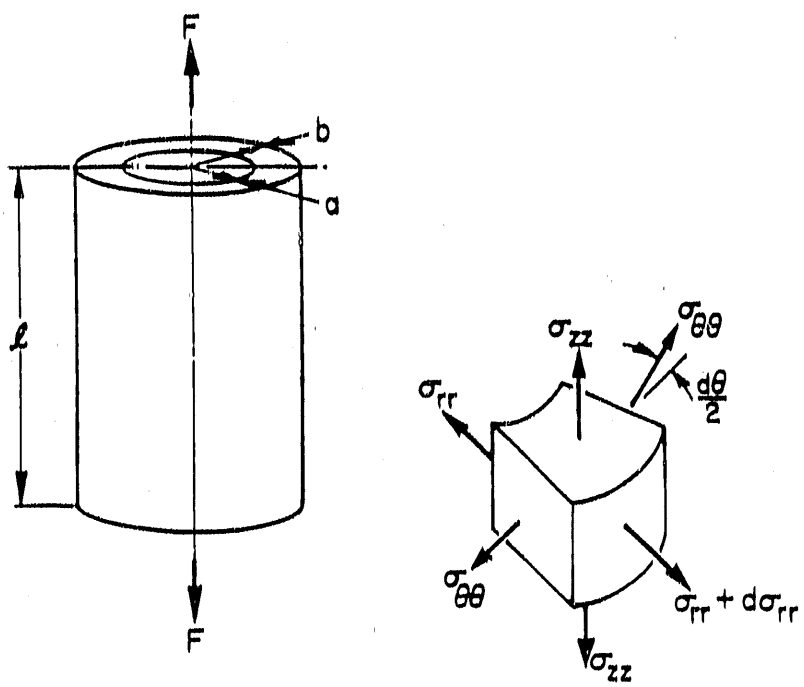

Figure 7.7. The fiber-sheath model.

determined by the difference in Poisson's ratios of the components. The Poisson's ratios for ceramics are relatively low, and the difference between matrix and fiber ratios will be small. This is especially true in the Nicalon-SiC system, in which the Poisson's ratios for the materials are equal. The effect of Poisson contraction can essentially be ignored in the analysis of ceramic-ceramic systems. A more detailed analysis of the stress and strain expressions from the fiber-sheath model is given in Appendix B.

Recently, a similar analysis has been applied to the investigation of coatings on metal filaments (93-97). The results are being used to develop a better understanding of the influence of interfacial reaction zones in metal-matrix composites. In many fiber-reinforced metal-matrix composites, a reaction between the fibers and matrix occurs both during processing and service. The brittle interfacial zone significantly influences the mechanical behavior of the composite. Ochiai and Murakami (93) examined the mechanisms associated with the fracture of materials containing brittle zones and developed a model describing behavior and failure based on the multiple fracture of the brittle coating on a notch-insensitive ductile fiber. The analysis follows the multiple-fracture approach, and interfacial shear stress is defined as

$$\tau_i = (\sigma_{cg}[(d_f + 2c)^2 - d_f^2]/4)\, d_f \ell_c \ , \qquad (31)$$

where c is the coating thickness. The phenomenon was studied in detail, and a computer program simulating the segmental fracturing of the brittle film was developed. The distribution of tensile stress in a segmented

coating and the distribution of shear stress at the fiber-coating interface were approximated, and the results were verified experimentally. The effects of coating thickness on the fracture behavior of metal wires was examined; however, the analysis was not applied to the determination of interfacial shear stresses at the fiber-coating interface. It was assumed that the bonding was strong enough to prevent debonding at the interface.

8. CONTROLLING THE INTERFACE

8.1 Introduction/Background

In evaluating the mechanical behavior of Nicalon/SiC composites fabricated early in the development of the forced-flow, temperature-gradient chemical-vapor infiltration process (FCVI), both brittle failure and ductile composite fracture were observed in specimens produced under similar conditions (Figure 8.1). A thorough analysis of fractured composite specimens that employed scanning and transmission electron microscopy revealed a thin film at the fiber-matrix interface (Figure 8.2). Auger electron spectroscopic (AES) analysis of heat-treated Nicalon fibers revealed a film composed of silicon and oxygen on the surface of the fibers (Figure 8.3) (98). The layer appears to be the result of the diffusion of silicon dioxide to the fiber surface during heating prior to infiltration. The silica layer binds the fibers and matrix together too strongly, resulting in brittle behavior. An intermediate coating applied to the fibers prior to infiltration was, therefore, determined to be needed to weaken the fiber-matrix bond and produce the crack deflection and fiber pull-out that contribute to the toughening of a composite (40).

Secondary ion mass spectroscopic (SIMS) analysis of composite samples fabricated from uncoated Nicalon fibers revealed higher concentrations of chlorine in the fibers than in the matrix (99). This suggests that the fibers may be chemically attacked by chlorides during matrix deposition (methyltrichlorosilane is the infiltration precursor), perhaps resulting in the degradation of fiber properties. A strength reduction in the fiber reinforcement yields a decrease in the strength of

ORNL PHOTO 6676-87

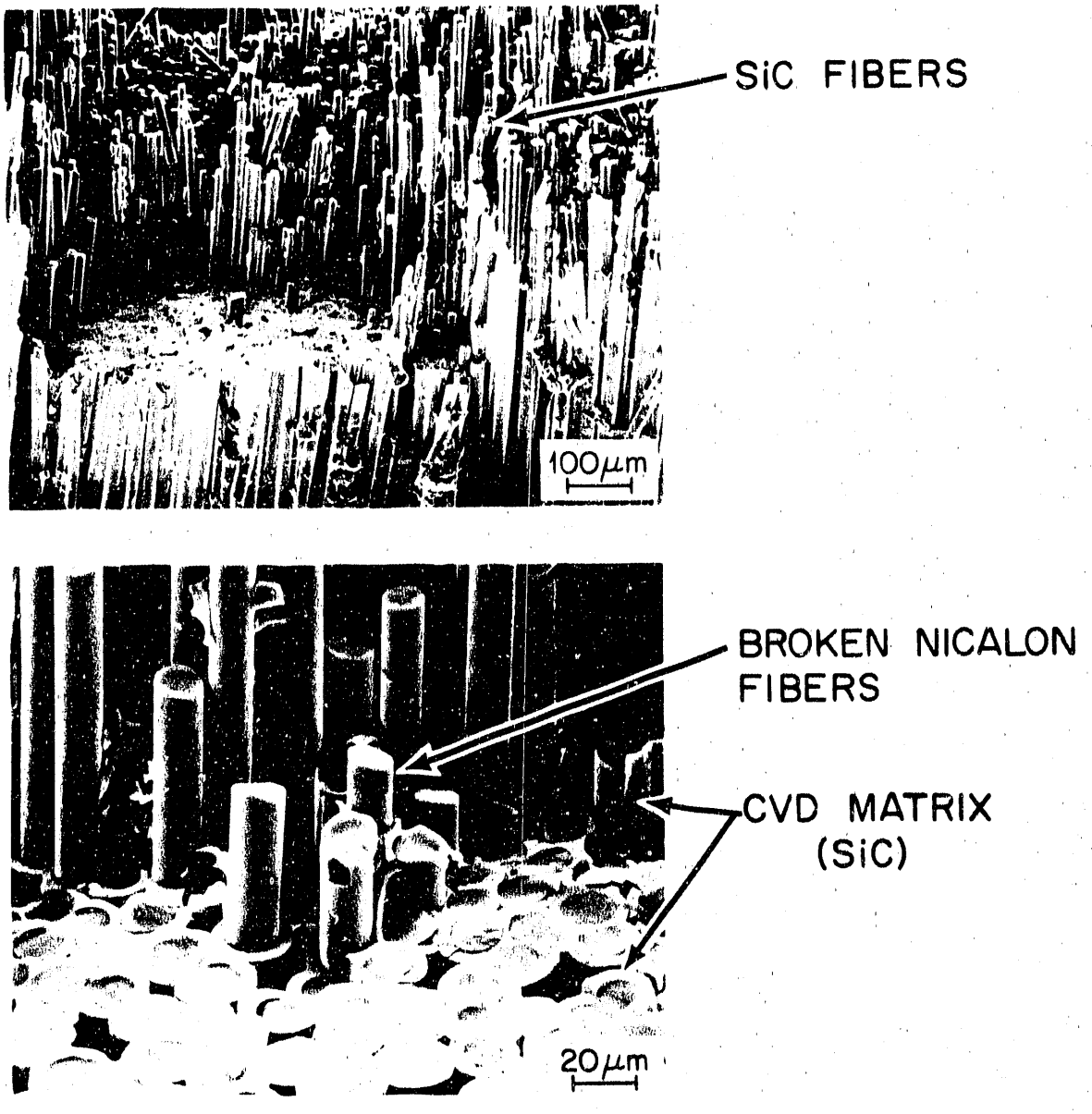

Figure 8.1. The fracture surface of a unidirectionally reinforced Nicalon-SiC composite containing 50 vol % fiber. The sample exhibited both brittle fracture and fiber pull-out, demonstrating the erratic behavior observed during testing early in the program.

ORNL PHOTO 6676-86

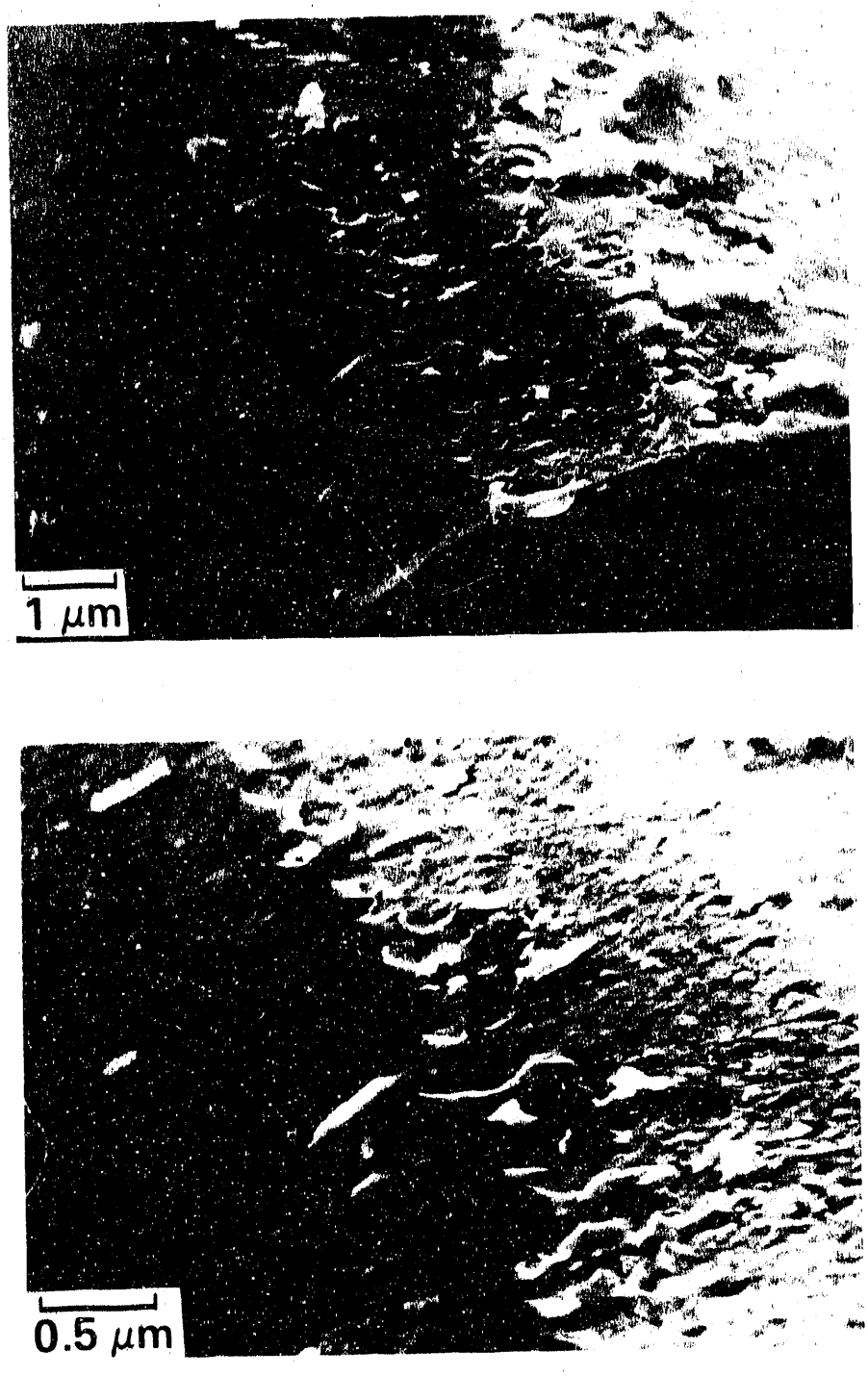

Figure 8.2. Film found on surface of Nicalon fibers heated to 1475 K in argon.

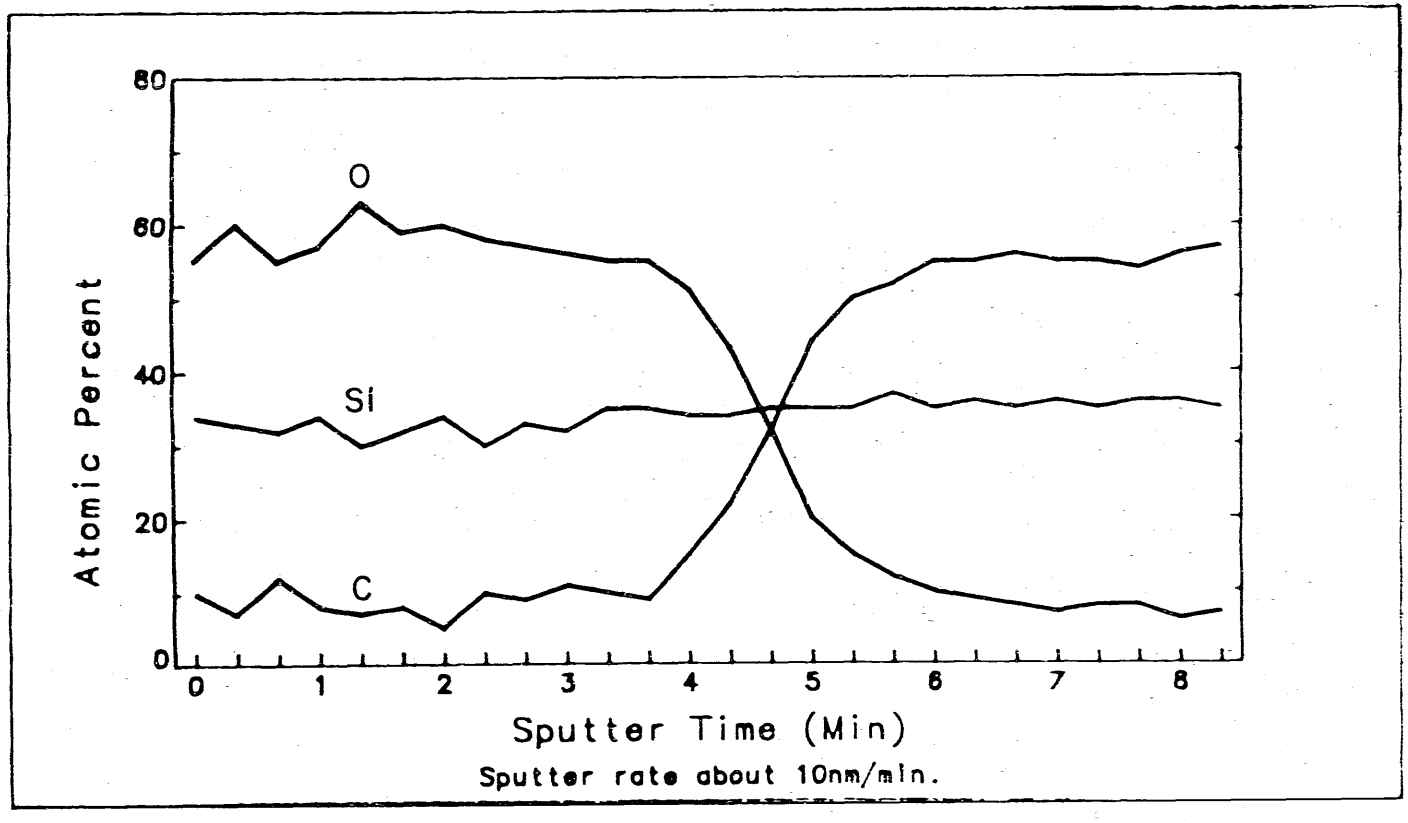

Figure 8.3. Auger depth profile of the surface of Nicalon fibers heated to 1475 K in argon.

the composite, therefore an intermediate coating may be necessary not only to obtain satisfactory fiber pull-out but to protect the fibers during processing.

8.2 Intermediate Coatings

As discussed, numerous factors must be considered in choosing the reinforcement, matrix, and fabrication procedure to be used in developing reliable composite materials. These include chemical and mechanical compatibility between materials during fabrication and during service, the degree of bonding between matrix and reinforcement, and the degree of mechanical and chemical damage that may occur during processing. These are of critical importance because the ultimate properties of the composite will be determined by the retained strength of the reinforcement and the degree of bonding at the fiber-matrix interface. The difficulties encountered arise from chemical interactions at the fiber-matrix interface during processing and service.

To alleviate many of the difficulties, the incorporation of a third phase in the form of a thin coating on the surface of the fibers has been found to be advantageous (100-105). The coating is applied to the filaments prior to fabrication, and its functions are twofold: (1) to protect the fibers from damage during processing or environmental attack in use and (2) to control interfacial bonding and friction at the interface. Thin layers can protect the fiber reinforcement from chemical attack during processing and then can act as a diffusion barrier between the fibers and matrix, hindering chemical interactions and, consequently, both protecting the integrity of the reinforcement and controlling the

bonding. Low-modulus or "soft" materials can act to relieve a portion of the thermally induced stresses and can provide enhanced debonding and slip at the interface.

Interfacial coatings or treatments to control fiber-matrix bonding have been examined with positive results. A thin pyrolytic carbon layer deposited on Nicalon fibrous preforms prior to densification increased product reproducibility and improved mechanical properties in Nicalon-SiC composites fabricated by chemical-vapor infiltration (CVI) techniques. The thin films were deposited on the fiber surfaces to prevent chemical interaction and to weaken the fiber-matrix interface, enhancing fiber pull-out and slip. Use of this method has resulted in increased toughness and ultimate strength of the composite materials.

Pyrolytic carbon was chosen to be intentionally applied as an intermediate layer for the FCVI Nicalon-SiC composites for several reasons. It has been shown that a carbon-rich layer forms on the fiber surface in Nicalon-reinforced lithium aluminosilicate (LAS) glass-ceramic composites during processing (106-108). The carbon-rich layer weakens bonding at the fiber-matrix interface, resulting in a composite having high toughness. The layer could not be detected in samples having low strength and low toughness.

A review of other CVI methods employed in the fabrication of ceramic composites revealed that resin binders are employed in preform fabrication (109). These are subsequently heat-treated, pyrolyzing the binders and forming a carbon coating on the fibers. Other (110) methods deposit carbon on the fibrous preforms using CVI before subsequent densification. The carbon deposition procedure generally uses

methane as the reactant and is, thus, chlorine-free and requires relatively low temperatures, limiting fiber degradation that may be caused by environmental factors. The carbon-coating parameters can be adjusted to produce laminar structures in the films that lie parallel to the fibers, enhancing slip (111,112). However, the usefulness of pyrolytic carbon is limited by its low resistance to oxidation. The carbon layer may also provide for excessive slip, thus reducing the ultimate strength of the composite. Therefore, other coatings with different bonding and oxidation characteristics were assessed for application to the fiber-matrix interface to alter the bonding and the mechanical behavior of the resulting composite body.

Elemental silicon was chosen as an interface layer because it was thought that by diffusing silicon into the fiber the stability of the Nicalon fibers would improve. Thermodynamic calculations have been used to show that elemental silicon could react with the excess carbon present in the fiber (113), preventing the formation and subsequent degassing of carbon monoxide upon heating of the fibers. A thin silicon film could also oxidize at high temperatures to form a viscous glass that would heal cracks in the composite structure and hinder further oxygen penetration.

Another approach is to deposit a silicon carbide coating from a chlorine-free precursor to protect the fibers from chemical corrosion by HCl during densification. Silicon carbide can be deposited from a mixture of methylsilane and argon in the temperature range of 975 to 1275 K. The coating is physically and chemically compatible with the fibers and matrix. The density of the deposit is generally low, and the mechanical properties are poor. This procedure may be beneficial in

providing a compliant coating that would fail at low strain, enhancing debonding and aiding in the slip process.

Boron nitride has been employed as a modifying interlayer in various composite systems (64,114). Submicron boron nitride coatings have proven valuable in controlling fiber-matrix bonding and interaction in zircon and zirconium titanate composites, as well as in other glass matrix systems. The graphite-like properties of boron nitride, combined with its chemical inertness, make it an excellent alternative to carbon for use in oxide-based systems in which carbon would react with oxide fibers or matrices at elevated temperature. Boron nitride offers an improvement in resistance to oxidation at elevated temperatures as compared to carbon.

Boron has properties similar to those of silicon; thus, it was also chosen to be deposited as an interlayer. Elemental boron has a melting point of 2575 K. Boron can be deposited from a diborane-argon mixture at the relatively low temperature of 775 K. At higher temperatures in air, a boron layer would oxidize to form a low-melting-point glass that would act as a crack sealer. Boron and silicon are brittle materials, whereas carbon and boron nitride possess structures that allow these materials to act as lubricants. In certain applications, nickel has been applied to carbon fibers as an intermediate layer to aid in wetting and to prevent chemical interaction during processing of metal-matrix composites. Metals offer alternative properties such as ductility, which may result in unique interfacial bonding and deformation phenomena. Molybdenum can be easily deposited at low temperatures and possesses desirable high-temperature properties.

9. EXPERIMENTAL PROCEDURES

9.1 Deposition System

The apparatus employed for the deposition and infiltration experiments is shown in Figure 9.1. The furnace consists of an aluminum water jacket with two concentric tubular shells capped at the ends and fitted with a water inlet at the bottom edge and an outlet at the top. The interior of the jacket is insulated with a low-density graphite felt and a thin layer of graphite foil, which reduces exposure of the interior to direct heating and increases efficiency of the furnace through lower heat loss to the jacket. Ports have also been provided in the shell for thermocouple access and gas-purge lines.

The jacket is bolted to an upper extension and to a lower base. O-ring seals join the components. The upper extension is aluminum, but no means of cooling is provided. This upper section contains the exhaust outlet and is capped with a removable lid. The lid, which is also aluminum, is water-cooled with a 40-mm sight port equipped with gas purges to prevent condensation on the 6-mm-thick quartz window during deposition. The lid is attached to the extension using a series of bolts around the upper diameter and is sealed with an O-ring.

The base section is also uncooled. The base provides support for the furnace, feed-throughs for water-cooled electrodes, access for the gas-distribution system, and support for the heating element. The graphite heating element is mounted to electrodes, which are attached to the base through a ceramic insulator. The base is fitted with a center port and a base plate with internal and external O-ring seals. The gas distributor-specimen support is fed through the base plate into the

ORNL-DWG 88-14864R

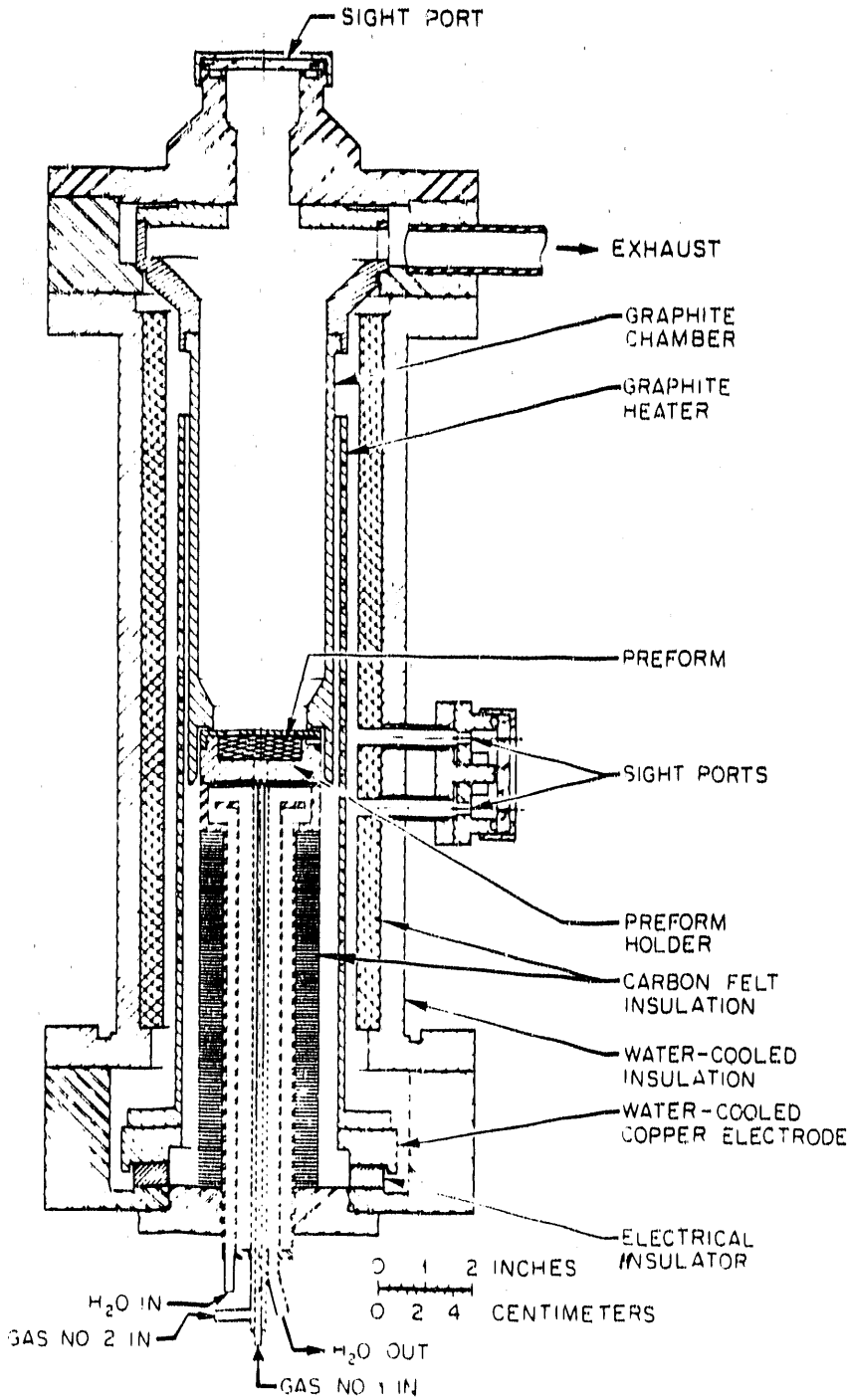

Figure 9.1. Details of the chemical-vapor-infiltration furnace for the densification of fibrous preforms using the FCVI process.

furnace. The furnace is, therefore, loaded from the bottom and is completely sealed using O-rings.

The furnace is resistively heated using a graphite element and single-phase alternating current. Power is supplied by a 50 KVA transformer, which is regulated by a silicon-controlled rectifier (SCR). The SCR receives a control signal from a number of sources that are dependent on processing options. The temperature of the furnace can be maintained utilizing either internal thermocouples or an external pyrometer. The device outputs are fed to a proportional controller. Alternatively, the furnace can be operated in a manual model.

The critical components of the infiltration apparatus are the water-cooled injector and the graphite holder (Figure 9.2). The water-cooled gas injector is composed of several concentric stainless steel tubes, connected to form separate gas and water passages. The fibrous preform is positioned atop the water-cooled surface and is held in place by an outer perimeter lip and a cylindrical graphite chamber. The chamber also acts to isolate the heating element from the reactant gases. The upper section of the gas distibutor is protected by the graphite chamber and the lower areas are insulated with graphite felt. The injector is spring-loaded from the bottom such that the inner chamber is pressed against the inner-surface water-cooled lid. Grafoil* gaskets at the injector and holder surfaces seal the internal workings, forcing all gases to flow through the preform. The seals also hinder gas flow to the heating element, and the element region is purged with argon to provide

*Union Carbide, Danbury, Connecticut.

ORNL-DWG 85-7788CR2

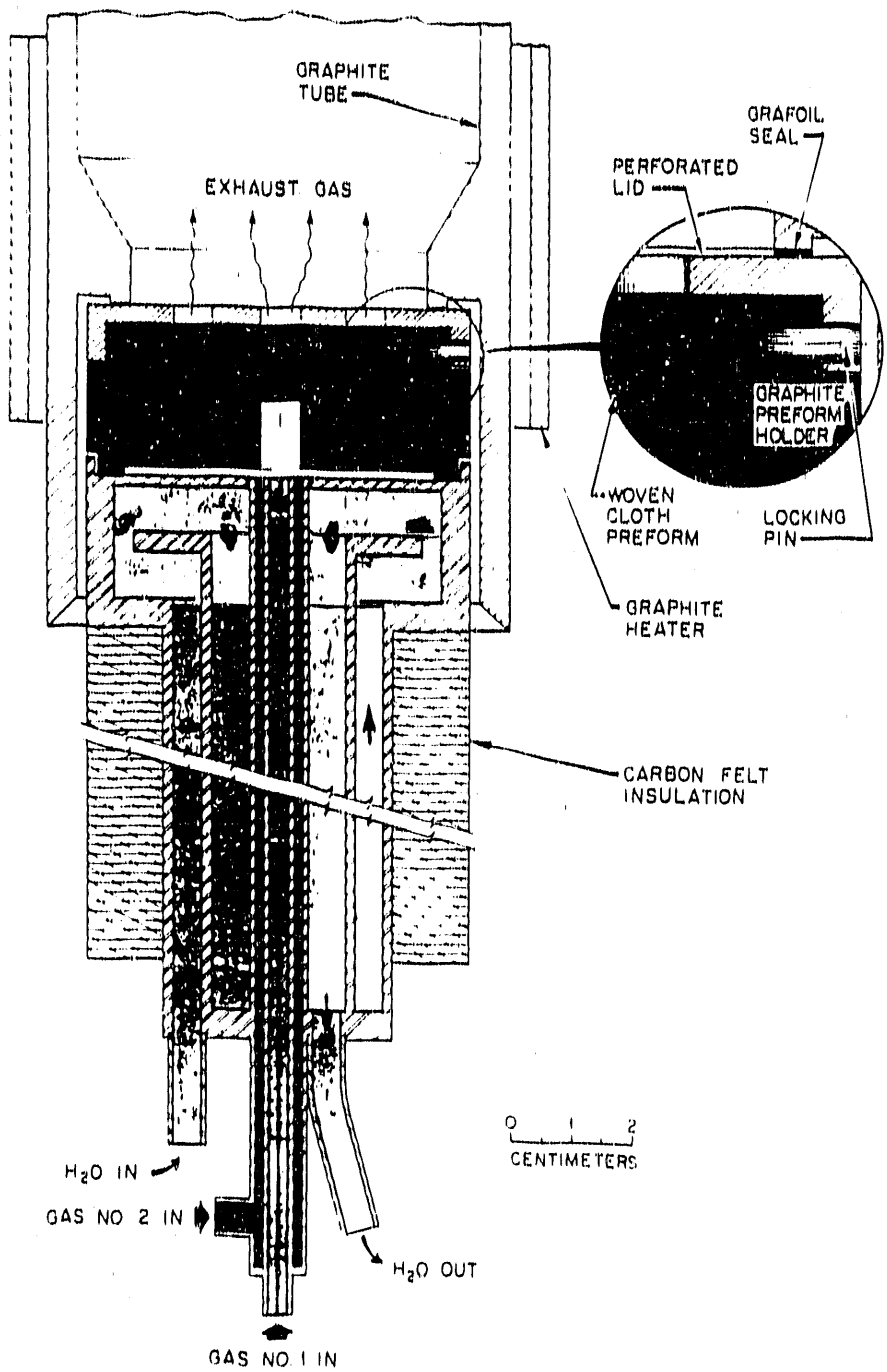

Figure 9.2. Details of the water-cooled gas distributor.

further protection. A 6.5-cm-diam by 10-cm-long graphite spacer can be placed between the graphite holder and the water-cooled injector to provide a uniform isothermal hot zone across the preform.

9.2 Instrumentation

A schematic of the infiltration system is given in Figure 9.3. The control systems have been automated to allow for unattended operation and to eliminate daily cycling. The furnace operates on either a time- or pressure-control circuit. A photograph of the system is given in Figure 9.4.

The corrected optical temperature at the top surface of the specimen is measured and controlled by a single-wavelength automatic optical pyrometer* equipped with a time-proportioning power controller. The operating temperature must be measured directly from the top surface of the specimen. As infiltration proceeds, the density and thermal conductivity of the specimen increase and the heat flow through the infiltrating composite increases. More heat is required to maintain the proper temperature and thermal gradient for deposition to continue. This is demonstrated by a steady increase in voltage and current being supplied to the furnace as densification proceeds. In the past, a thermocouple placed in contact with the outside surface of the coating chamber at the level of the specimen did not allow for this change. Furnace power levels were held constant and the top surface temperature

---

*IRCON, Inc., Niles, Illinois.

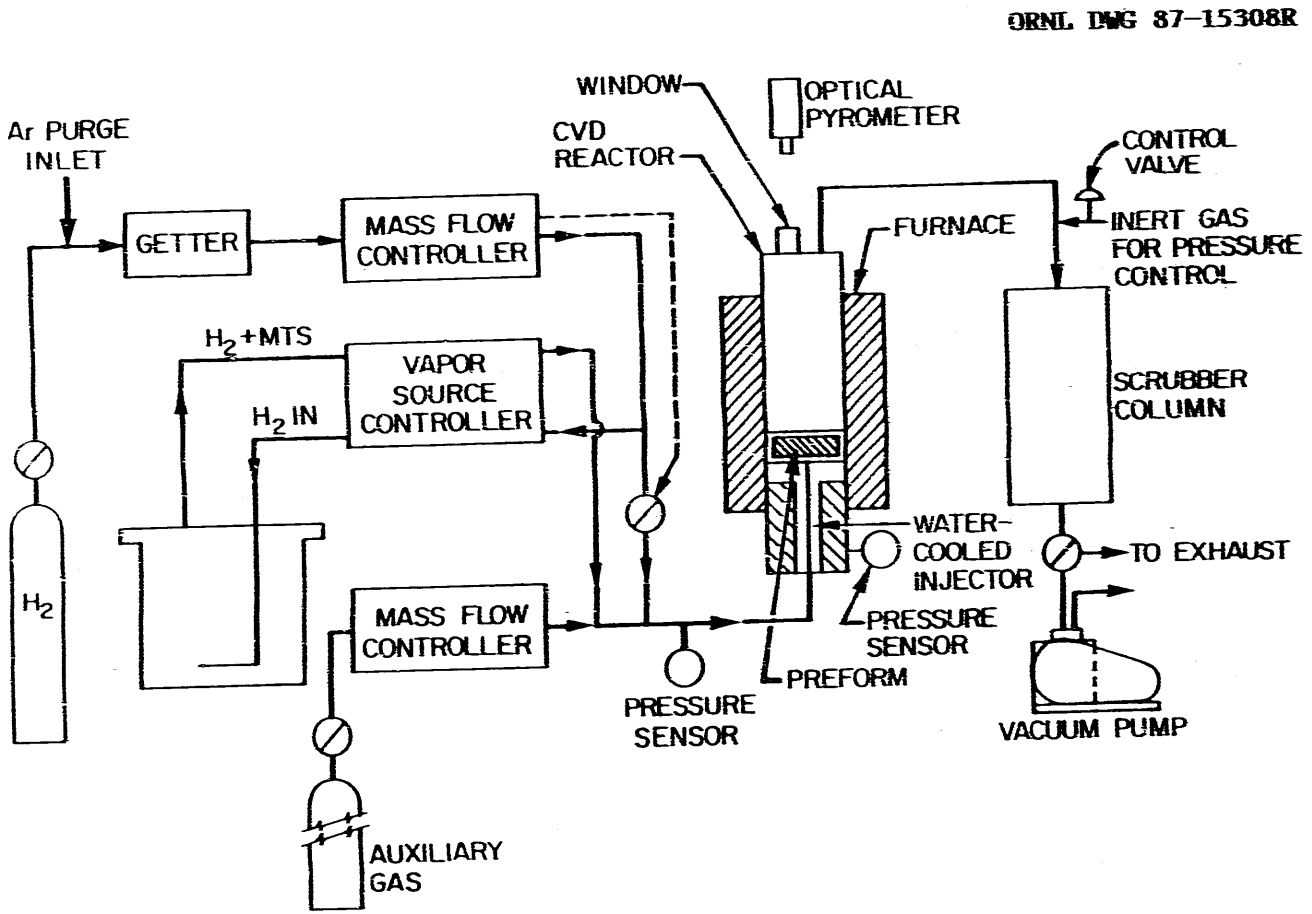

Figure 9.3. Schematic of the infiltration system.

Figure 9.4. Photograph of infiltration furnace.

of the specimen slowly decreased. This resulted in poor densification of the lower regions of the composite closest to the water-cooled gas injector.

Pyrometer sighting was accomplished through a right-angle glass prism and a 6-mm-thick quartz window. Corrections were made for the prism and window absorptions and reflections. Matched pairs of prisms and windows were calibrated at the Oak Ridge National Laboratory (ORNL) Metrology Research and Development Laboratory. The sets were installed and the pyrometer reading was corrected using a black-body hole drilled into the lid of a graphite preform holder. The average loss resulting from the quartz window and prism was $20 \pm 4°$ at 1475 K.

During the infiltration process, silicon carbide deposits on the surface of the holders and closes the black-body hole; therefore, an alternative sighting method was pursued. A point on the surface of the graphite holder was chosen as the sighting area. Once reactant gases were introduced in the chamber and deposition proceeded, corrections were provided for the emissivity difference of the silicon carbide coating. The spectral emissivity factor for silicon carbide is between 0.75 and 0.85. The optical pyrometer is equipped with an adjustable emissivity factor; a value of 0.85 was used during the infiltration procedure.

The flow rates of the gases and vapors were controlled by mass flow controllers.* The hydrogen gas was purified by passage through a de-oxygenating unit and a moisture-absorbing column containing drierite. Argon gas was passed through a drying column to eliminate moisture but

---

*MKS instruments Inc., Andover, Massachusetts.

was not deoxygenated. Other gases such as silane, ammonia, and diborane were not treated but were used as received (at least 99.99% purity).

Methyltrichlorosilane (MTS), which is a liquid at room temperature, was carried to the reactor by a flow of hydrogen through an evaporator, and flow was metered using a vapor source controller.* On bubbling the hydrogen carrier gas through the reservoir containing the liquid reactant, the gas stream becomes saturated with vapor. The vapor-source controller monitors the heat capacity of the incoming gas and the exit gas mixture and, by subtracting the incoming carrier flow signal, can measure the vapor concentration in the outgoing mixture. The controller varies the flow of hydrogen to the reservoir to maintain the given vapor concentration. The gas-vapor mixture is then diluted to the proper ratio using a mass flow controller that is placed in series with the vapor-source controller. The system is designed to allow for complete control of not only vapor flow but gas-to-vapor ratios. Although the source controller maintains the flow of reactant independent of pressure or temperature, the reservoir temperature was held at 297 K using a constant temperature bath to minimize cooling effects caused by the evaporation of the MTS.

On completion of densification, a programmed cool-down sequence was used to minimize thermal shock effects. Temperature control was switched from the optical pyrometer to a thermocouple controlled programmer.**

---

*Research, Inc., Minneapolis, Minnesota.

**Tylan, Inc., Torrance, California.

The programmer is also equipped to control external relays, thus allowing gases to be switched on or off during the cool-down sequence.

The effluent from the reaction chamber containing excess reactants and reaction products was passed through a trap containing a solid sodium hydroxide-calcium hydroxide mixture. This method effectively removes the chlorides before the exhaust gases reach the mechanical pump or are released into the building exhaust system. Effluent hydrogen amounting to <500 cm^3/min was allowed to flow into the hood exhaust system. The flow rate of the hood exhaust is adequate to dil the hydrogen to a point below its explosive limits.

Pressure control was accomplished using a gas-ballast technique. A capacitance manometer was used to monitor the furnace pressure, and the pressure was held constant by injecting argon gas into the pump inlet to regulate effective pumping speed.

9.3 Composite Fabrication

9.3.1 Preform fabrication

Fibrous preforms were fabricated by stacking multiple layers of plain-weave ceramic-grade Nicalon cloth, Lot #AP125001, rotated in a 30°-60°-90° sequence within the cavity of a graphite holder (Figure 9.5). The layers were hand-compressed and held in place by a perforated graphite lid pinned to the holder. The average sample dimensions were 45 mm diam by 12.7 mm thickness, and 52 layers of cloth were used to form each preform. The continuous fibers are coated with a polyvinyl acetate sizing by the manufacturer to protect the fiber during handling or weaving. The sizing was removed after the layers were stacked in the

Y201840

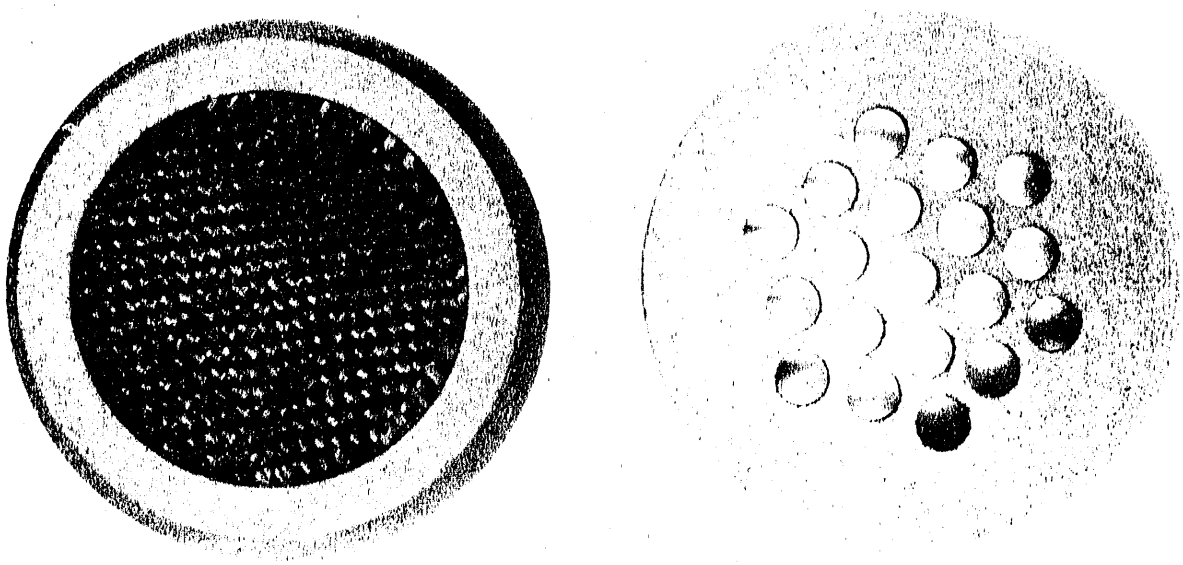

Y201841

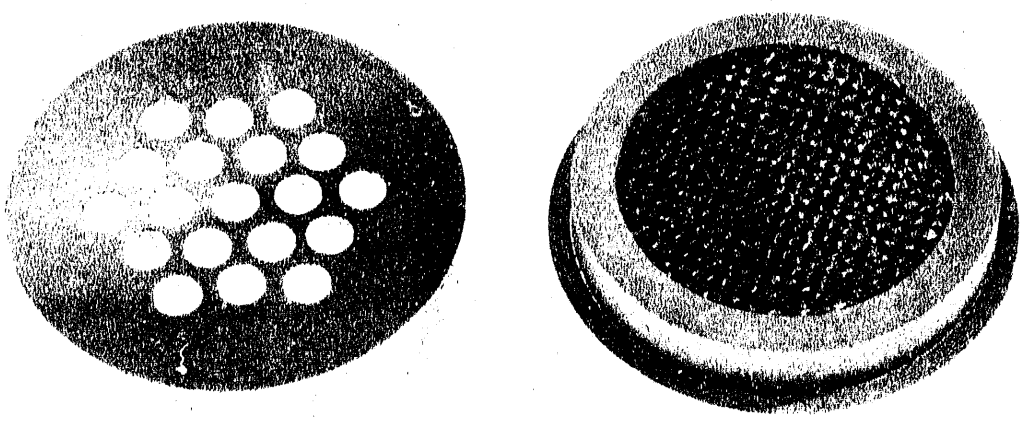

Figure 9.5. Graphite retainer containing plain-weave cloth layers.

graphite holders through multiple washings in acetone. The average fiber content of the resulting fiber preforms was 41.4 ± 1.3 vol %.

9.3.2 Intermediate coating deposition

The preforms next were precoated with thin layers of various materials. The deposition parameters and nominal thicknesses of the films are summarized in Table 9.1. The coating runs were carried out using the following procedure. The preform was placed atop the graphite spacer, and Grafoil gaskets were used to seal the injector to the spacer and the preform to the spacer. Hot water of 355 K average temperature was supplied to the injector, whereas only cold water was passed through the furnace sections and electrodes.

The apparatus was evacuated (with the exception of the MTS reservoir) to an ultimate pressure of < 0.5 torr using a rotary mechanical pump. The argon purges to the furnace base, shell, and sight port were set at appropriate levels (a total flow of 5 L/min), and argon was allowed to flow to the preform at a rate of 500 cm^3/min through the reactant gas supply lines, subsequently flushing these lines at the same time. The furnace was then heated to the specified deposition temperature and the system was allowed to degas for 30 min.

After these preliminary procedures, the operation pressure of the furnace was set on the controller and reactants were directed into the reaction chamber. The system was allowed to stabilize and then run at steady state for 2 hours. On completion, the reactant gases were replaced with argon gas flow and the furnace was cooled to room

Table 9.1. Precoating processing parameters.

Sample No.	Fiber (%)	Precoat[a]	Reactant flow (cm^3/min)	Ar diluent (cm^3/min)	Temp. (K)	Precoat thickness[b] (μm)	Infiltration time (hours)
170	41.8	Si	15 (SiH_4)	500	675	0.17	24.8
171	41.3	Carbon	10 (C_3H_6)	500	1375	0.03	21.3
172	42.1	Boron	15 (B_2H_6)	500	775	0.50	26.1
173	39.0	SiC	25 (CH_3SiH_3)	500	1125	0.08	23.7
174	41.8	Carbon	20 (C_3H_6)	500	1375	0.12	21.7
175	43.5	Carbon	15 (C_3H_6)	500	1375	0.07	22.0
176	42.0	SiC	25 (CH_3SiH_3)	500	975	0.22	22.5
177	40.4	BN	15 (B_2H_6)	40 (NH_3)	875	0.13	20.6
178	40.3	uncoated	NA	500	1375		21.7
179	41.4	Mo	25 (MoF_6)	500 (H_2)	1125	0.18	24.1
180	41.7	Carbon	25 (C_3H_6)	500	1375	0.28	23.7

[a]All precoat times = 2 hours.

[b]Calculated from weight gain.

temperature by simply switching off the power. Finally, the sample was removed from the furnace after evacuating the system for another 30 min at room temperature.

9.3.3 Densification

The coated preforms were densified using the FCVI process. The composites were infiltrated with SiC produced by the decomposition of methyltrichlorosilane (MTS) in hydrogen. The deposition parameters used were as follows: a top surface temperature of 1200°C, an MTS flow of 0.333 g/min, a hydrogen flow of 500 cm^3/min, and atmospheric pressure.

The infiltration procedure is the same as for the deposition of intermediate layers, with a few exceptions. All infiltration runs were performed at atmospheric pressure, approximately 740 torr for the majority of the experiments. The samples were heated to 1475 K with the full 500 cm^3/min of hydrogen flowing through the vaporizer by pass. When the temperature stabilized, flow was diverted to the evaporator using a set of pneumatic valves and diluent flow was supplied by a mass flow controller in series with the vapor contoller. A predetermined pressure differential across the sample (170 KPa) designated complete infiltration. At this point, system control is switched to a programmer. The programmer diverts the hydrogen flow back to the vaporizer bypass and slowly cools the furnace to room temperature. The hydrogen flow is replaced by argon below 500 K. The samples were removed from the furnace once the system had reached ambient temperature. The MTS reservoir was weighed after every run to verify actual reactant usage and flow.

9.4 Mechanical Properties

9.4.1 Sample preparation

The densified composites were weighed in the graphite holders to examine densification. In some earlier experiments, the seals at the injector leaked, resulting in incomplete infiltration. Fortunately, this did not occur in this series; thus, samples were not returned to the furnace for further densification. All infiltration runs were completed in one step. The composite samples were then removed from their holders by cutting and grinding away the graphite using carbide-tipped tool bits.

The samples were then sliced into various pieces for analysis. Figure 9.6 shows the areas from which the specimens were removed. All cutting and grinding was accomplished using a high-speed grinder/slicer. Metal-bonded low-concentration slicing blades were employed in the cutting, and low-concentration resin-bonded wheels were used for grinding.

9.4.2 Flexure testing

Twelve bend bars were prepared from each sample (four each from the top, middle, and bottom areas) to determine variations within and between samples (Figure 9.6). The bars were cut from the samples parallel to the 0-90° orientation of the top layer of cloth using a diamond saw, and tensile and compression surfaces were ground parallel to the long axis of the specimens. The average dimensions of the bars were 2.5 × 3.3 × 45 mm; all were measured and weighed to determine densities.

The strengths of all composites were measured in four-point bending. It has been noted that the four-point flexure test does not measure the

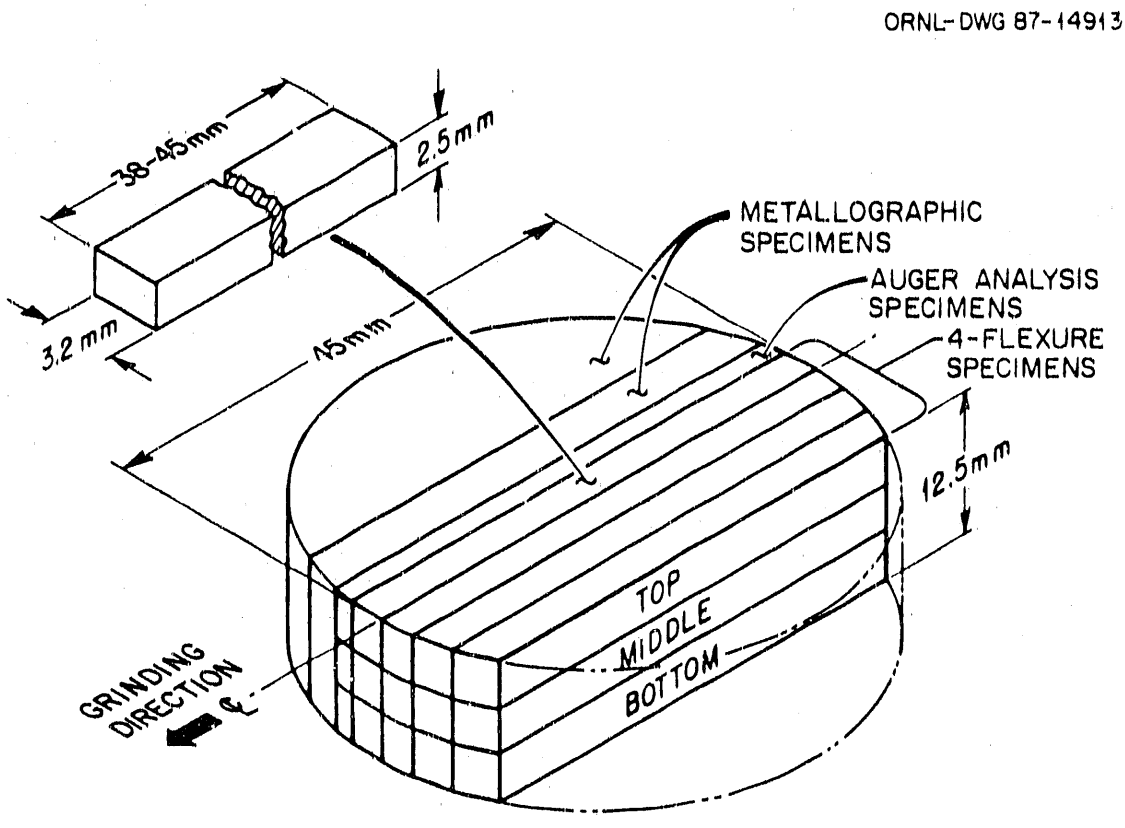

Figure 9.6. Location of test specimens within the composite sample.

true tensile strength of a composite material because of the failure frequently occurring first at the compression face during actual testing. However, flexure testing can yield a quantitative estimate of the strength of a sample and provide a simple method for characterization and comparison of specimens processed under various conditions.

Flexural strengths were measured at room temperature utilizing four-point bending methods. A support span of 25.4 mm, a loading span of 6.4 mm, and a crosshead speed of 0.051 cm/min were used in the testing. To minimize shear affects, a minimum span-to-depth ratio of 15:1 has been specified for glass-matrix composites having similar properties (78); however, testing was limited to the span-to-depth ratio of 10:1 due to sample length constraints. Specimens were loaded perpendicular to the layers of cloth. Load versus time (crosshead displacement) curves were recorded to examine fracture behavior. Flexure properties such as flexure strength and modulus were determined using the guidelines described in ASTM test method D790-81. The flexure strengths were calculated from the equation

$$\sigma_{uF} = 9/8[P/wt^2] , \tag{32}$$

where P is the applied load, w is the specimen width, and t is the specimen thickness. Flexure strain was determined from the initial slope of the load-deflection curve

$$\epsilon_F = mL^3/4wt^2 , \tag{33}$$

where m is the slope and L is the span length.

9.5 Fracture Surface Analysis

The fracture surfaces of the specimens were examined using both Hitachi S-800 and JEOL JSM-35CF scanning electron microscopes. Specimens that did not completely fracture during flexure testing were broken by hand so that the fracture surfaces could be examined.

Elemental analysis of the fracture surfaces was accomplished using a Perkin-Elmer PHI 660 scanning Auger system. The specimens were fractured in the chamber of the instrument to limit contamination of freshly exposed surfaces. Specimens with average dimensions of 2 × 2 × 20 mm were prepared from a wafer cut 5 mm from the center of the sample (Figure 9.6). After slicing, all specimens were thoroughly washed in acetone, freon, and then in ethanol and were degassed at 150°C at reduced pressure prior to being placed in the instrument. This procedure ensured removal of cutting lubricants and other materials that could contaminate both the fresh fracture surfaces of the specimens and the instrument. Surface analysis of bulk fibers, matrix, fiber surfaces and pull-out grooves was completed on several representative specimens (Figure 9.7).

9.6 Preparation of Oxidized Specimens

To examine a composite with "no interfacial bond," a carbon-coated sample was cut into thin wafers and ground to 2.5 mm, the thickness of a flexure specimen. The wafers were then cut in half, and one set was placed in an alumina tube furnace to be oxidized. The specimens were heat-treated in flowing oxygen at 1075 K for 44 hours to oxidize and remove the carbon interfacial layer. The samples were weighed before and after oxidation, and external surfaces were examined for discoloration, which may signify oxidation of the SiC fibers and matrix. Both the

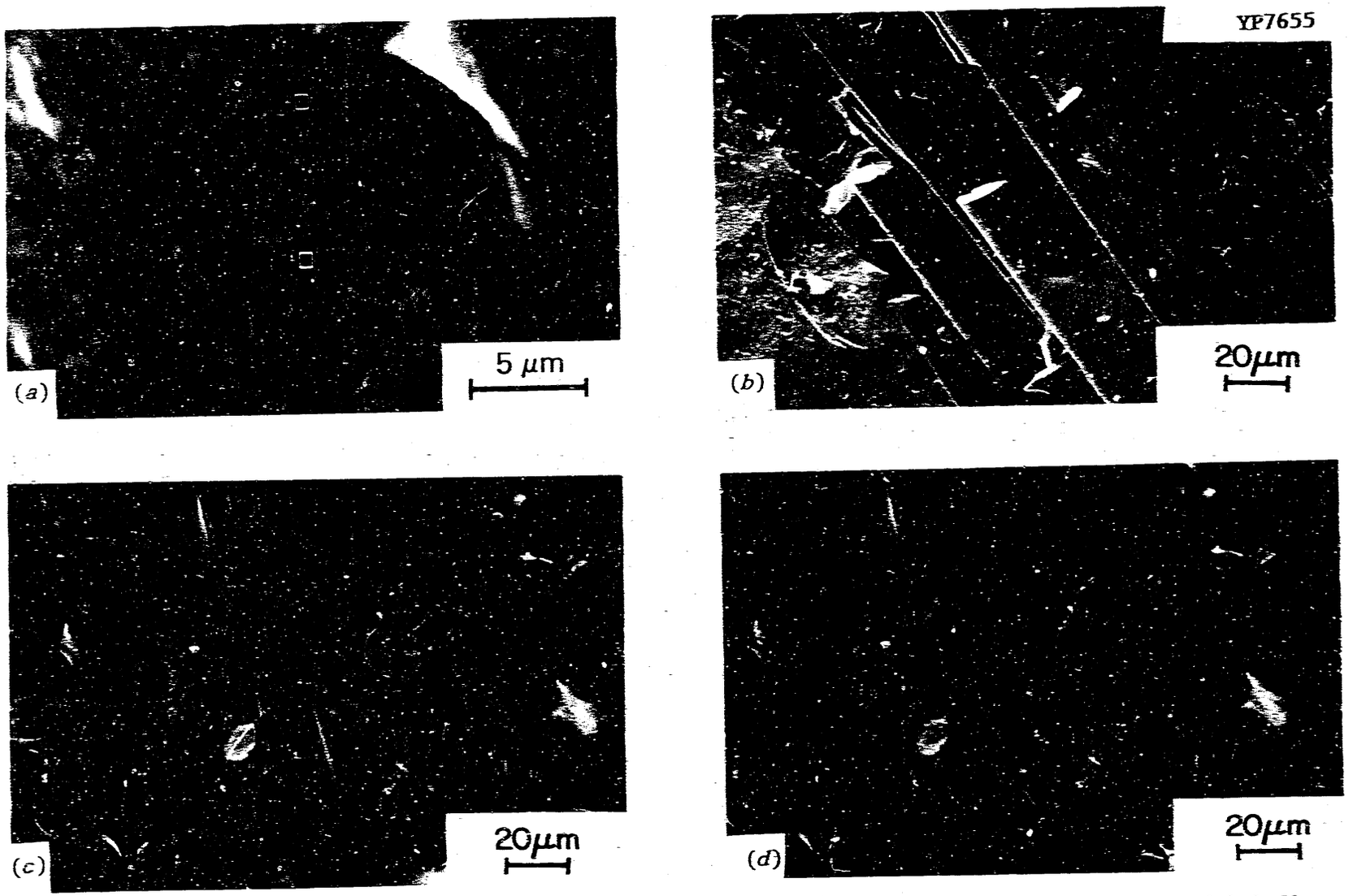

Figure 9.7. The features of the fracture surfaces analyzed using Auger spectroscopy: (*a*) bulk fiber, (*b*) fiber surface, (*c*) pull-out groove, and (*d*) matrix.

treated and untreated halves were then cut into standard flexure specimens and tested in the same manner as the other composite samples.

9.7 Thermodynamic Considerations

Material interactions at the interface during the different stages of processing were evaluated using thermodynamic equilibrium calculations. A free-energy minimization program, EQUILIB (115), was used to determine possible chemical reactions that may occur. The computer code was accessed through the F*A*C*T system at McGill University in Montreal, Quebec, Canada. The program is based on the SOLGASMIX thermodynamics code, and the results were related to observed bonding behavior, fiber degradation, and Auger analyses.

The following boundaries were examined in each system:

1. fiber-interlayer interface during deposition of the interlayer,
2. fiber-interlayer boundary after deposition but during infiltration,
3. interface between the silica coating at the fiber surface and the intermediate coating during deposition of the interlayer,
4. silica-interlayer interface during matrix deposition,
5. intermediate coating-matrix interface during infiltration, and
6. interlayer-matrix interface prior to the termination of infiltration.

9.8 Interfacial Frictional Stress

9.8.1 Indentation

A 6.0-mm-thick cross-sectional specimen was cut from each completed composite sample to be used for indentation testing. The specimens were cut along the 0-90° orientation of the top layer of cloth to ensure that a portion of the exposed fibers would be oriented perpendicular to the

cut surface. This alignment is essential for proper implementation of the indentation mechanics. The specimens were mounted and polished using standard metallographic techniques used for ceramic materials such as silicon carbide.

Loads were applied to fiber ends using a Vickers diamond indentor and a Shimadzu Type M instrument.* The edge-to-edge angle of the indentor is used in the calculation of interfacial friction to determine the displacement depth of the loaded fiber. The diamond indentor was examined using an optical microscope, and from photographs, the angle between the edges was verified to be 148°.

The interfacial stress measurement technique requires that the fiber be displaced to a depth at which the edges of the diamond contact the perimeter of the fiber cavity. Loading to the fiber ends was progressively increased until debonding was observed and then again until contact of the indentor with the edge of the fiber cavity was evident. Loads in the range of 1 to 3 N were required to displace the fibers. Impression dimensions were measured using the ocular scale of the indentor and from scanning electron microscopy photomicrographs.

The hardness of the fibers was calculated from indents placed in longitudinally polished fibers. A 1-N load was used because radial cracking or complete failure of the fibers ocurred at higher loads. Lower loadings were not used to avoid possible elastic recovery during unloading (116-118). The dimensions of the impressions were measured using the ocular scale of the indentor.

---

*Shemodyn Corporation, Tokyo, Japan.

CM4357
3μm

CM4358

9.8.2 Tensile testing

In an initial series of experiments, a 10.0-μm coating of silicon carbide was deposited on untreated large diameter (140-μm) AVCO SCS-6 filaments.* Graphite mounting fixtures similar to those described in ASTM standard D3379-75 for the tensile testing of brittle fibers were fabricated (Figure 9.8). The holders are designed to provide support for fragile single filaments during handling before testing. The filaments were glued into the graphite fixtures using a high-temperature graphite cement and were hung in the hot zone of the furnace. The coating was applied to 15-cm lengths of the filaments using the same conditions employed in densification of the composite samples, except at a reduced pressure of 13.3 KPa (100 torr). The reactant gases were introduced such that deposition occurred only on the center sections of the fibers (Figure 9.9).

The coated fibers were removed and an epoxy adhesive was applied to the remaining cavities of the fixtures to ensure adequate gripping of the fibers upon loading. The mounted filaments were placed in a small custom-made tensile frame for loading in tension. The load was applied by hand using a fine thread micrometer head, and the fibers were observed during loading using a low-power stereoscopic microscope. Tension was increased until repeated fragmentation of the coating was observed. The tension was held constant, and the critical lengths of the fractured sections were measured from photographs and by using the ocular scale of the microscope. It was necessary to hold the fibers in tension while the fragments were examined because releasing the load resulted in closing of

*AVCO-Textron, Lowell, Massachusetts.

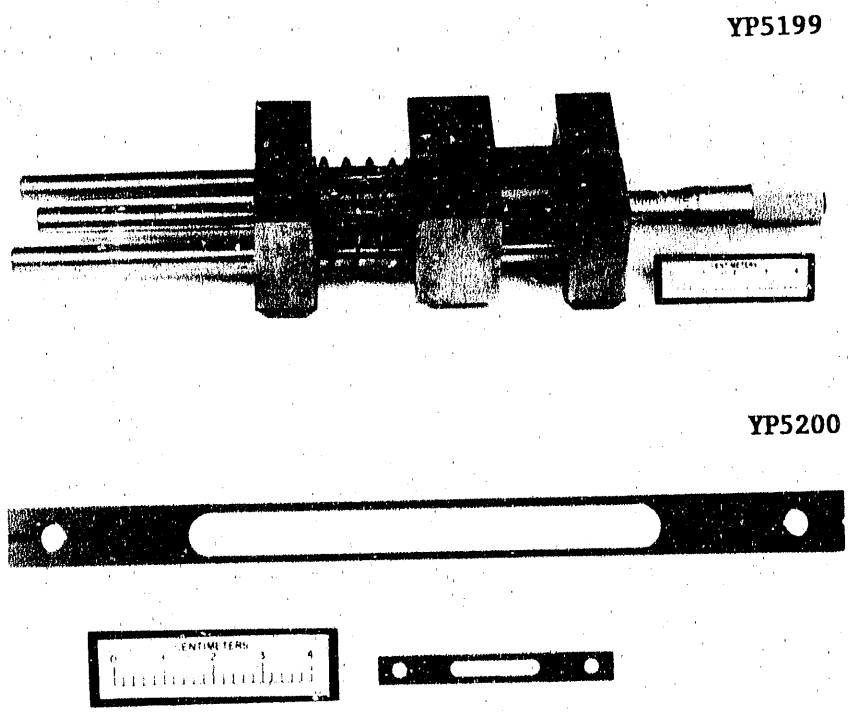

Figure 9.8. Photographs of the loading frame and fixtures used in the tensile technique for the measurement of interfacial stresses.

ORNL-DWG 85-11767R2

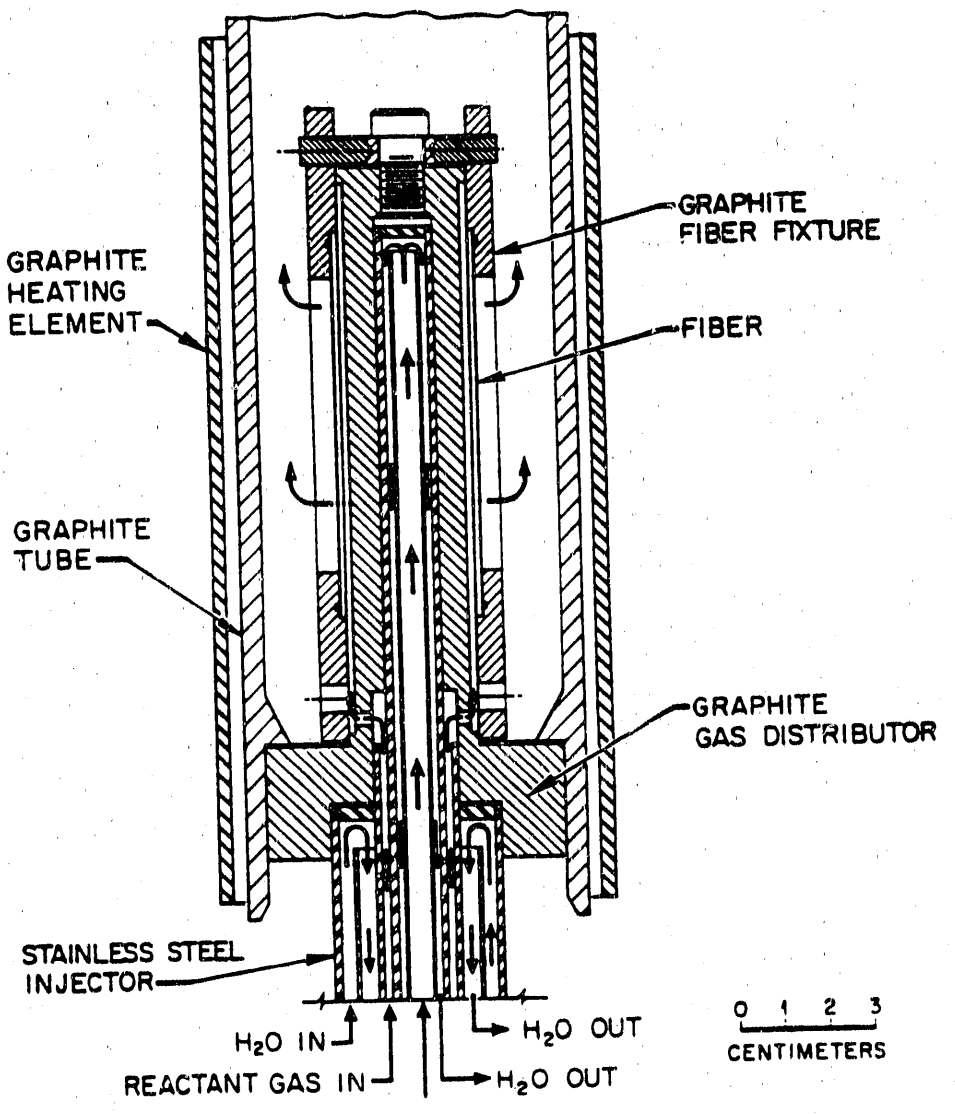

Figure 9.9. The gas distributor was redesigned to accommodate coating the center section of the fibers.

the cracks. In addition, if the segments slipped during stressing, sections of the coating buckled and spalled upon load release.

The procedure was repeated for filaments precoated with a <1.0-μm-thick film of pyrolytic carbon. The pyrocarbon layer was deposited on the filaments from a mixture of 25-cm^3/min propylene gas in 500-cm^3/min argon at 1375 K and a pressure of 3 KPa. A 10-μm SiC coating was then applied employing the previously described fixturing and procedures. The coated filaments were tested, and critical lengths were recorded.

The same methods were applied to Nicalon fiber tows. Acetone-washed yarns were placed in the same graphite fixtures and coated with SiC. Additional fiber lengths were coated with pyrolytic carbon and then silicon carbide. In this series of experiments, the SiC deposition pressure was reduced from 13.3 KPa to 3 KPa to produce uniform coatings throughout the fiber bundles. The fiber tows were tested, and segment lengths were measured from photographs at a magnification of 320X. Uniform loading of each individual filament within the entangled yarns was impossible, and fusion of filaments at contact points during coating compounded the difficulty. Only small areas exhibited the desired segmental fracturing of the coating.

It was recognized that the procedure could only be easily and routinely implemented using individual filaments. The average diameter of Nicalon filaments is in the range of 10-20 μm; therefore, the graphite tensile fixtures were miniaturized. At the same time, the gage length of the fixtures was shortened to fit into the chamber of a JECL 35CF scanning electron microscope. The stage of the microscope is capable of applying a tensile load to small specimens; thus, deformation and

fracture of individual Nicalon filaments with modifying interlayers and a thin coating of silicon carbide could be observed in situ.

Lengths of Nicalon yarn were washed in acetone, and while still immersed in the solvent, individual filaments were collected. The fibers were placed into the fixtures and affixed with graphite cement. Thin films of the precoat materials were deposited at conditions similar to those used to coat preforms before infiltration (Table 9.1). A final coating of SiC was deposited at 1475 K, an MTS flow of 0.165 g/min, a hydrogen flow of 250 cm^3/min, and a pressure of 3 KPa. The reduced pressure was necessary to produce the smooth uniform deposits needed to observe the segmented fracturing upon testing.

9.9 Fiber Tensile Strength

Nicalon tows were glued into graphite fixtures and washed in acetone to remove the sizing. The yarns were coated with the chosen intermediate layers using the conditions given in Table 9.1. The mounted fibers were heat treated at 1475 K in flowing argon for 25 hours to simulate infiltration thermal conditions. Epoxy was added to the empty cavities of the fixtures, and the fibers were tested while held in tension. The strengths of the fibers were calculated from the maximum recorded loads.

10. RESULTS

10.1 Composite Properties

The infiltrated composite samples had an average bulk density of 2.78 ± 0.19 g/cm^3, which is approximately 95% of theoretical density. The theoretical density is defined as the sum of the products of volume fraction and reported density of the components of the composite (fibers; precoat; and, after infiltration, SiC). These values are calculated directly from measured weight gain and are used only as a preliminary evaluation of the infiltration process. A photograph of an infiltrated sample before removal from the graphite fixture is shown in Figure 10.1 and a typical cross section is pictured in Figure 10.2.

The densities and four-point flexure strengths of the composite specimens are summarized in Table 10.1. The data are listed by position to correlate variations in the composite samples as a result of nonuniform infiltration. Density affects both flexure strength and fracture behavior.

10.2 Frictional Stress

The average hardness value for the Nicalon fibers for all samples tested was 22.0 ± 0.7 GPa. To further examine the indentation of the individual fibers, the tested areas of the samples were examined using the Hitachi S-800 scanning electron microscope (SEM). It was necessary to sputter carbon onto the polished cross sections before SEM examination because of the charging of epoxy mounting material. The dimensions of the impressions were measured from the SEM photos, and the results were

Y201684

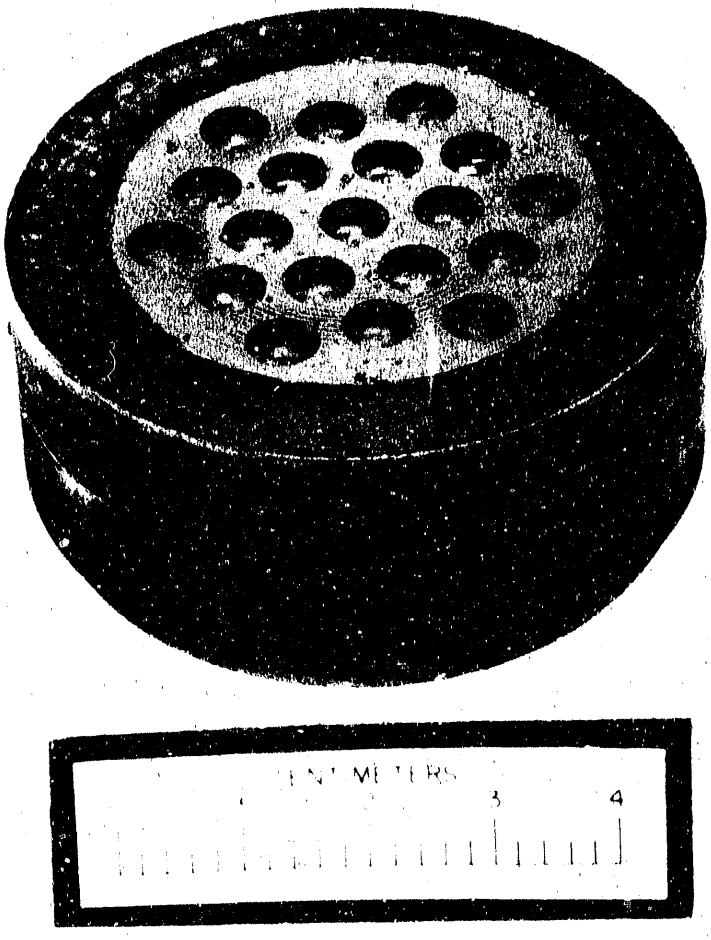

Figure 10.1. SiC-infiltrated Nicalon sample before being removed from holder.

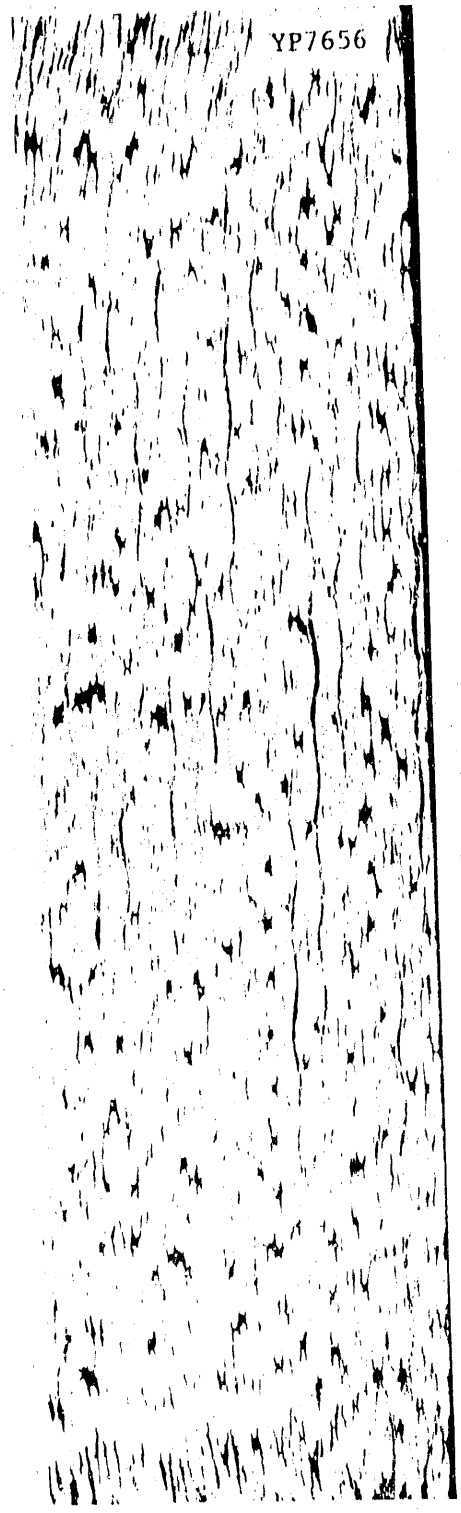

Figure 10.2 Representative cross section of a sample with an apparent density of 85% theoretical. 425X.

Table 10.1. Property summary for Nicalon/SiC composite specimens.

Sample No.	Position	Density (g/cm^3)	Theoretical density (%)	Flexure strength (MPa)
170	Top	2.43±0.03	83.5±1.0	99.0±4.1
	Middle	2.35±0.03	80.9±1.0	82.2±15.5
	Bottom	2.28±0.03	78.4±1.2	82.7±3.9
171	Top	2.41±0.04	82.8±1.3	424.8±24.9
	Middle	2.34±0.04	80.5±1.5	414.9±10.5
	Bottom	2.22±0.04	76.1±1.3	326.7±8.3
172	Top	2.48±0.03	85.3±0.9	109.5±9.7
	Middle	2.36±0.03	81.1±1.0	88.3±13.3
	Bottom	2.20±0.04	75.6±1.3	125.2±16.7
173	Top	2.46±0.03	84.6±1.0	100.3±14.2
	Middle	2.35±0.01	80.8±0.3	77.8±8.9
	Bottom	2.11±0.03	72.4±1.0	61.8±7.8
174	Top	2.51±0.03	86.2±0.9	419.3±24.4
	Middle	2.44±0.02	83.8±0.7	380.7±4.2
	Bottom	2.31±0.04	79.2±1.4	369.2±11.6
175	Top	2.40±0.01	82.5±0.5	98.0±7.2
	Middle	2.27±0.06	78.0±2.0	401.2±4.9
	Bottom	2.09±0.05	71.9±1.9	286.2±19.6
176	Top	2.50±0.03	85.9±0.9	91.0±2.8
	Middle	2.48±0.05	85.3±1.7	91.1±5.1
	Bottom	2.35±0.01	80.8±0.5	94.1±4.5
177	Top	2.42±0.03	83.1±1.6	138.8±29.5
	Middle	2.35±0.05	80.9±1.7	104.0±8.2
	Bottom	2.13±0.07	73.3±2.6	99.0±21.0
178	Top	2.47±0.01	84.8±0.3	89.1±9.5
	Middle	2.37±0.03	81.5±1.2	82.0±12.4
	Bottom	2.18±0.03	74.9±1.2	74.7±8.3
179	Top	2.39±0.02	82.1±0.8	61.8±23.5
	Middle	2.24±0.04	77.0±1.5	77.7±9.0
	Bottom	1.87±0.04	64.2±1.4	32.0±2.2
180	Top	2.53±0.01	87.2±0.1	419.2±1.9
	Middle	2.42±0.02	83.3±0.4	375.3±4.4
	Bottom	2.23±0.01	76.8±0.4	[illegible]0±10.9
180 (oxidized)	Top[a]	2.51	86.4	207.3
	Middle[a]	2.40	82.6	173.1
	Bottom[a]	2.21	76.0	185.2

[a]Single specimen.

compared with the dimensions acquired using the ocular scale of the indentor. A summary of the calculated interfacial frictional stresses is given in Table 10.2.

10.3 Fiber Tensile Strength

The tensile strengths of the coated and heat-treated Nicalon fiber yarns are listed in Table 10.3. The listed results include data retrieved from the literature (119-123). Nicalon tows coated with either silicon from silane or silicon carbide from methylsilane could not be tested. The fibers failed during heat treatment, and therefore, the strength of these samples could not be evaluated.

10.4 Fracture Behavior and Interfacial Stresses

10.4.1 Silicon carbide coatings

The sample composed of uncoated fibers and the composites prepared from preforms treated with thin coatings of SiC from methylsilane exhibited low flexure strength. The specimens displayed completely brittle failure, with no signs of fiber pull-out. Load-deflection curves and photomicrographs of the fracture surface of these composites are shown in Figure 10.3.

Auger analysis of fracture surfaces of composite specimens with silicon carbide coatings, either from methylsilane or MTS, provided evidence of an oxygen-rich layer on the fiber surfaces and in the pull-out grooves (Figures 10.4 and 10.5). A silica layer forms on the surface of the fibers during heating, and this layer adheres well to the fiber and the subsequent SiC coating. SEM photographs of fracture surfaces of

Table 10.2. Interfacial frictional stress calculated using the indentation method.

Sample No.	Indent load (N)	Av. fiber diameter (μm)	Frictional stress (MPa)
170	3	16.9±1.2	87.8±54.5
171	2	14.6±2.0	4.3±1.2
172	2	16.3±1.3	6.3±1.7
173	3	16.0±1.9	82.1±23.8
174	1	15.4±2.2	0.6±0.4
175	2	13.3±0.7	11.3±4.7
176	2	15.3±0.9	19.9±4.2
177	2	15.3±1.9	15.7±5.0
178	3	16.5±2.4	47.7±13.8
179	3	15.5±0.8	32.3±6.0

Table 10.3. Strength and modulus for treated Nicalon fibers.

Treatment	Strength (MPa)	Modulus (GPa)
As received	1766	106
Sizing removed[a]	2110	118
800°C Ar	1310	
1000°C Ar	1283	
1200°C Ar	1234	108
1300°C Ar	1262	110
1400°C Ar	848	104
1200°C air	660	110
1300°C air	1262	114
1400°C air	1379	102
1000°C vacuum	690	
1200°C vacuum	345	94
1300°C vacuum	200	48
Uncoated continuous	2315±160	
Uncoated from cloth	1730±126	
Carbon coated	2175±191	
Boron coated	861±70	
Boron coated/HT 1475 K	163±40	
BN coated[b]	1886±464	
BN coated	1718±304	
1275 K 10%HCl/H_2 1 hour	1847±99	
1375 K 10%HCl/H_2 1 hour	1223±89	
1475 K 10%HCl/H_2 1 hour	861±70	
1475 K 10%HCl/H_2 25 hours	71±15	

[a]Three washings in acetone.
[b]Coated by Synterials, Inc., Herndon, VA.

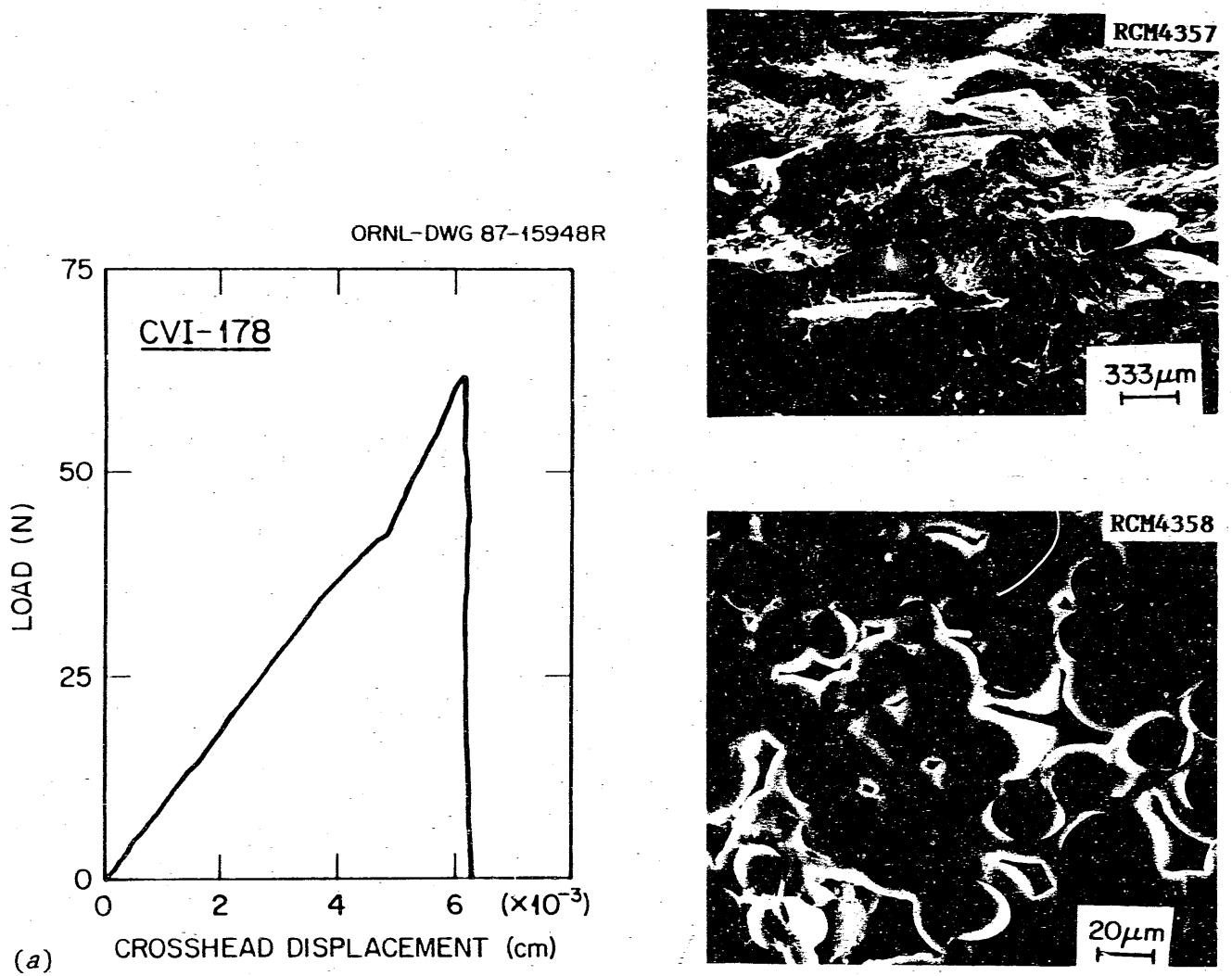

Figure 10.3. Load-displacement curves and fracture surfaces of specimens containing Nicalon fibers coated with silicon carbide: (*a*) CVI-178, uncoated fibers; (*b*) CVI-173, SiC from methylsilane; and (*c*) CVI-176, SiC from methylsilane.

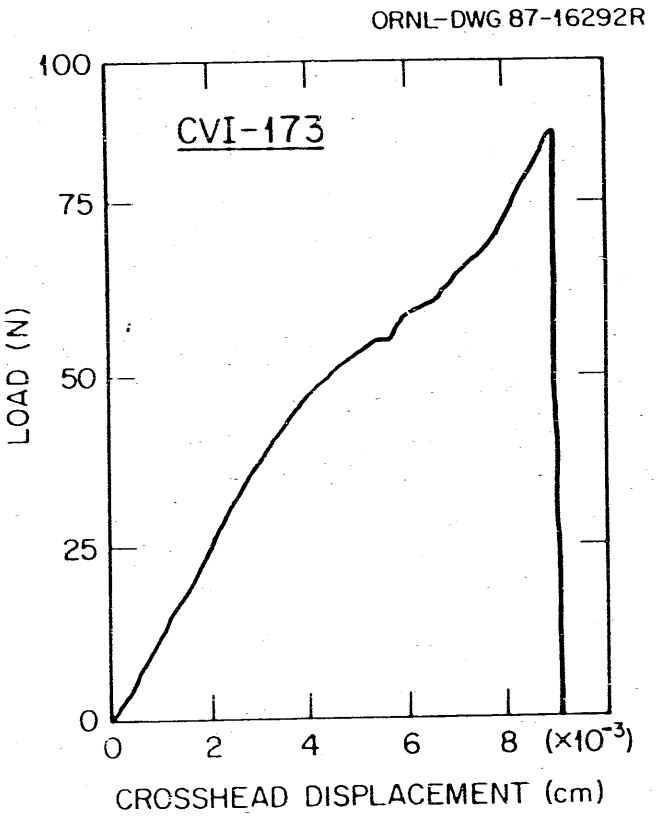

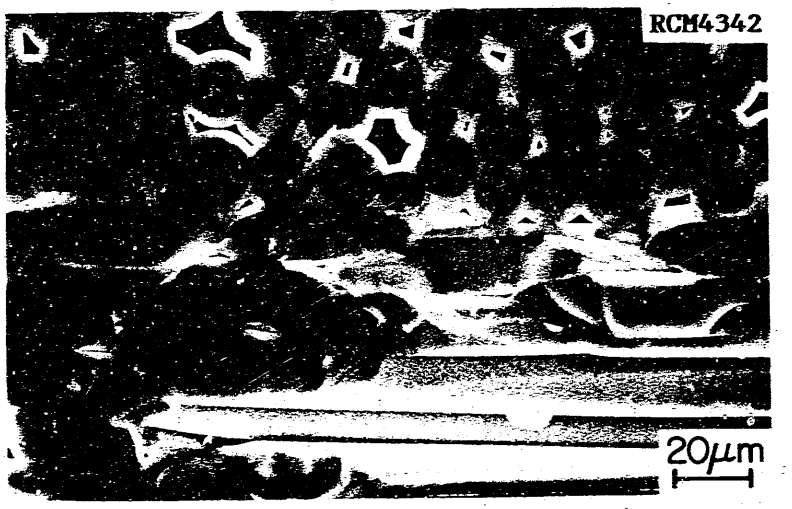

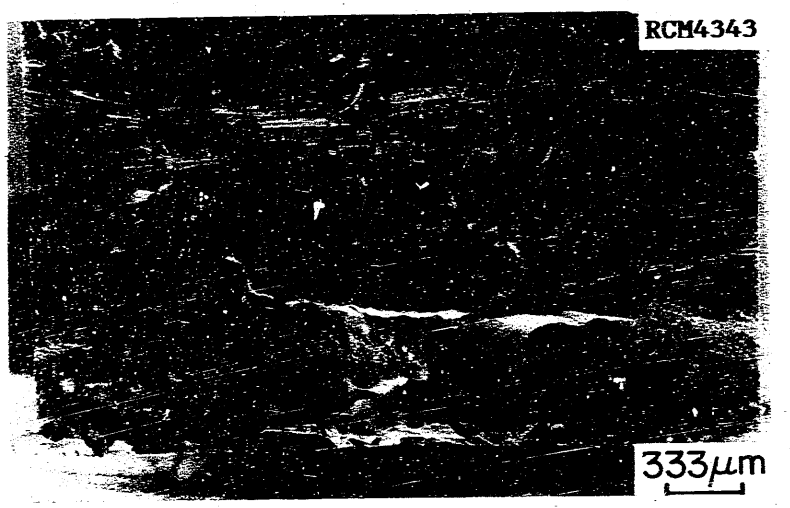

(*b*)

Figure 10.3 continued

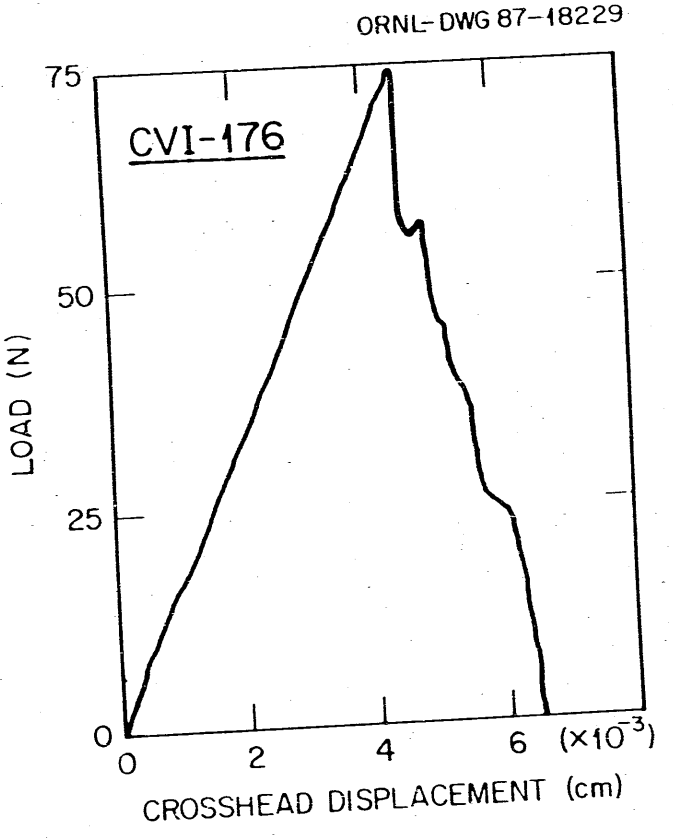

(c)

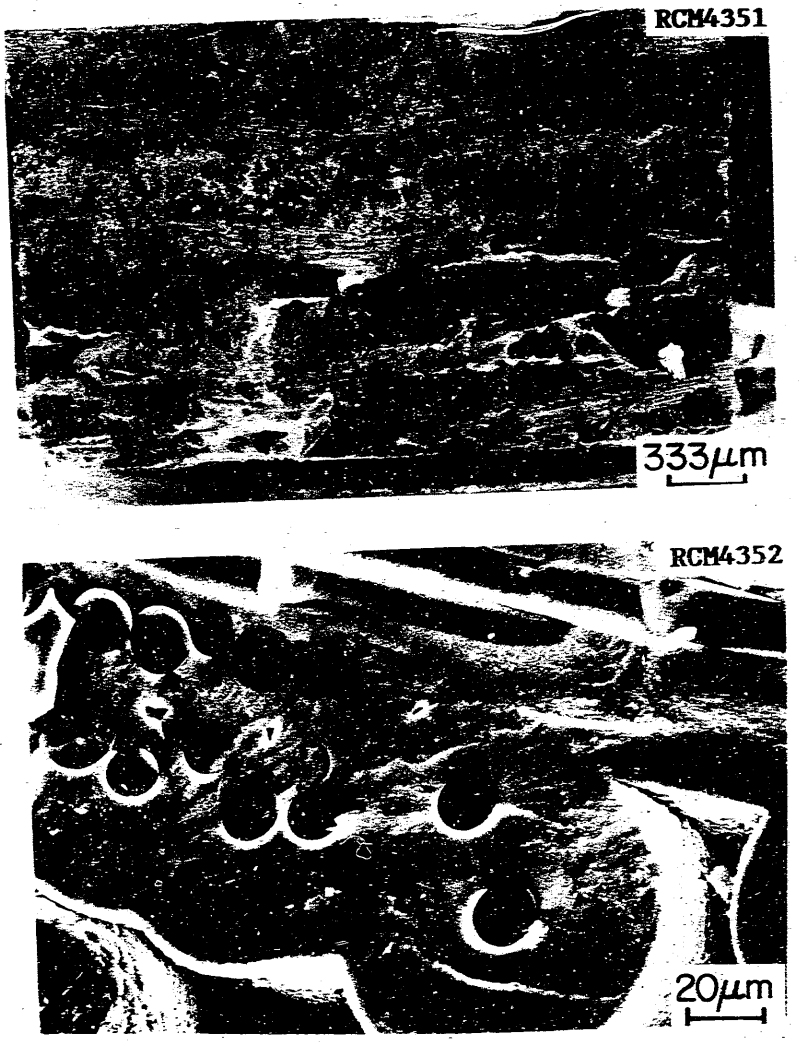

Figure 10.3 continued

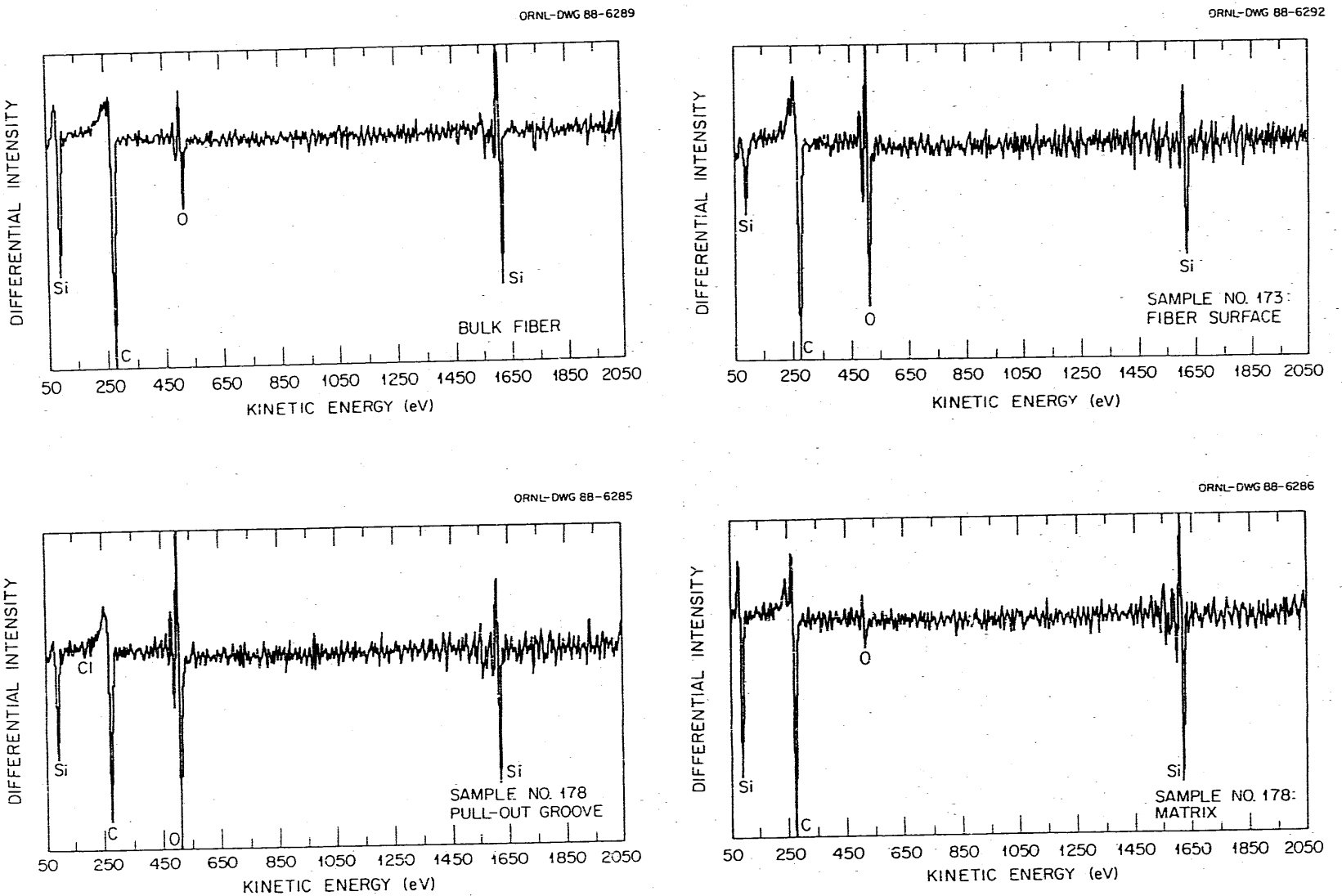

Figure 10.4. AES analysis of fracture surface features for an SiC composite specimen fabricated from untreated Nicalon fibers.

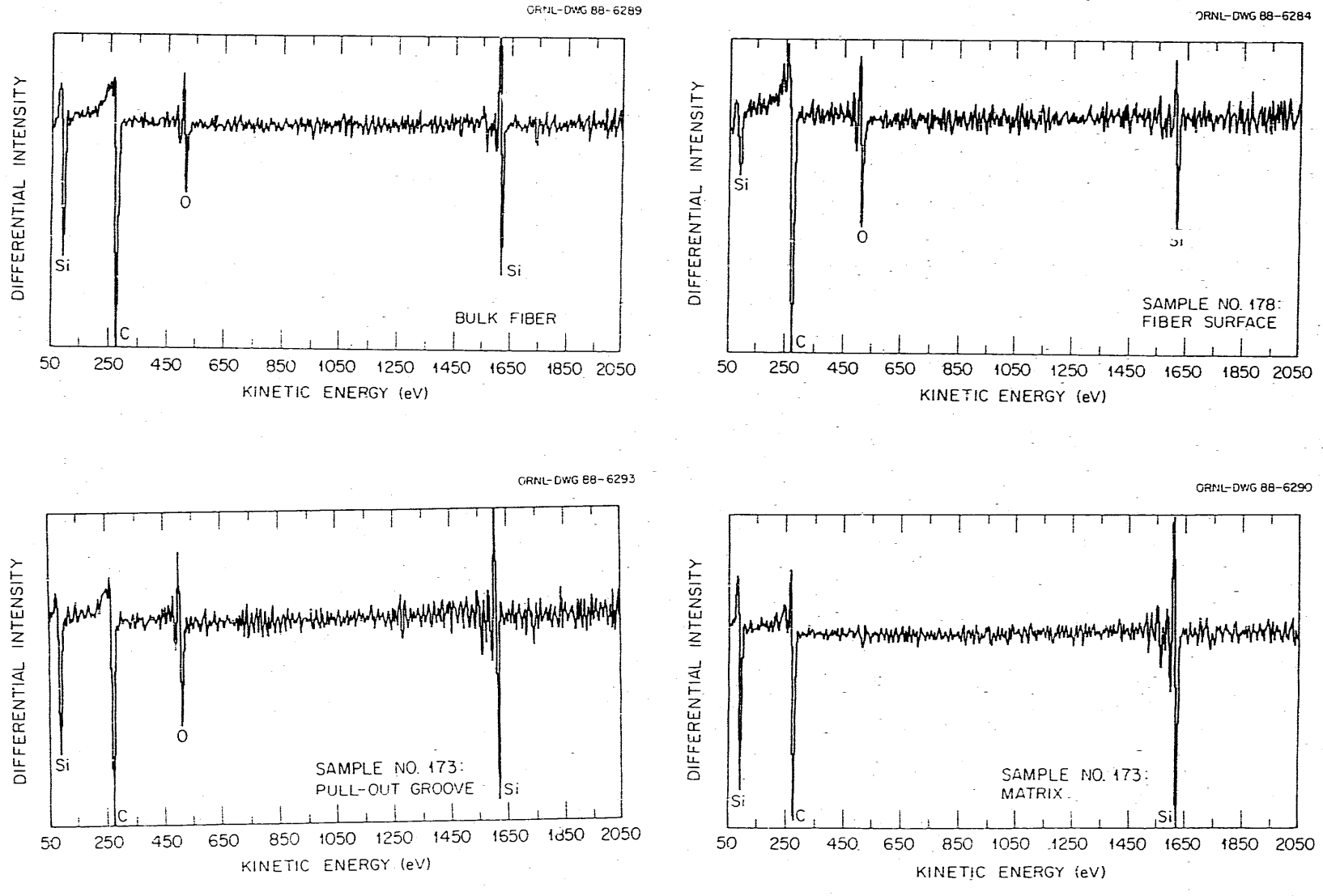

Figure 10.5. AES analysis of fracture surface features for an SiC composite specimen containing Nicalon fibers coated with an intermediate SiC layer deposited at 1125 K.

similar samples show the film on both the fiber surface and the pull-out grooves in the matrix. This layer appears as a glassy translucent film and can be seen in the micrographs in Figure 10.6.

The flat smooth fracture surfaces suggest that the silica layer bonds the fibers and matrix too strongly. Indentation measurements confirmed the high interfacial frictional stresses for samples CVI-178 and CVI-173. In some cases, the loads caused splitting of the fiber and cracking of the surrounding matrix [Figure 10.7(*a*) and (*b*)]. The cracks generated during indentation propagated through the matrix to neighboring fibers. There was no evidence of crack deflection at these fiber-matrix interfaces (i.e., cracks passed undisturbed across the boundary).

Although the interfacial shear stress for sample 176 [Figure 10.7(*c*)] was much lower than the measured values for the previously described composites, the flexure strengths for the sample showed no improvement. The silicon carbide intermediate coating was deposited at a lower temperature, which may have resulted in a very-low-density coating. If this is true, the coating could enhance debonding at the interface. The fibers, however, provided no reinforcement, as demonstrated by the low strengths. The loss of fiber strength was evident in that continuous fibers coated with silicon carbide from methylsilane could not be tensile tested because the coated tows failed during heat treatment.

The intense bonding and fiber-property degradation are a result of the chemical reactions that occur within the body of the fiber and at the fiber-matrix interface. The vapor-deposited SiC coating understandably bonds strongly to the underlying silica layer. Thermochemical analysis of the interactions that would likely occur during the various processing

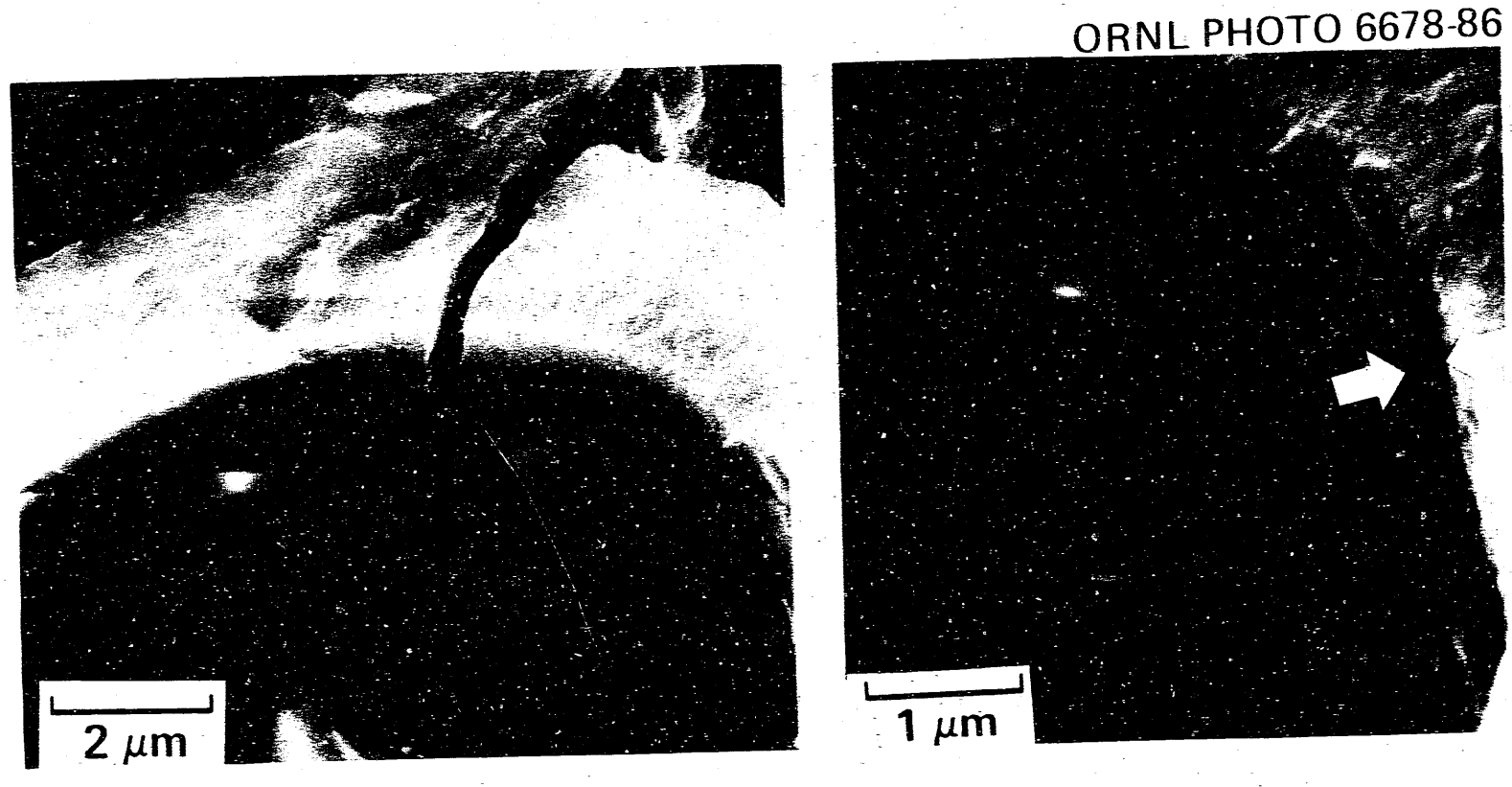

Figure 10.6. A thin, translucent layer observed in the pull-out grooves of fractured composite specimens fabricated from uncoated Nicalon fibers.

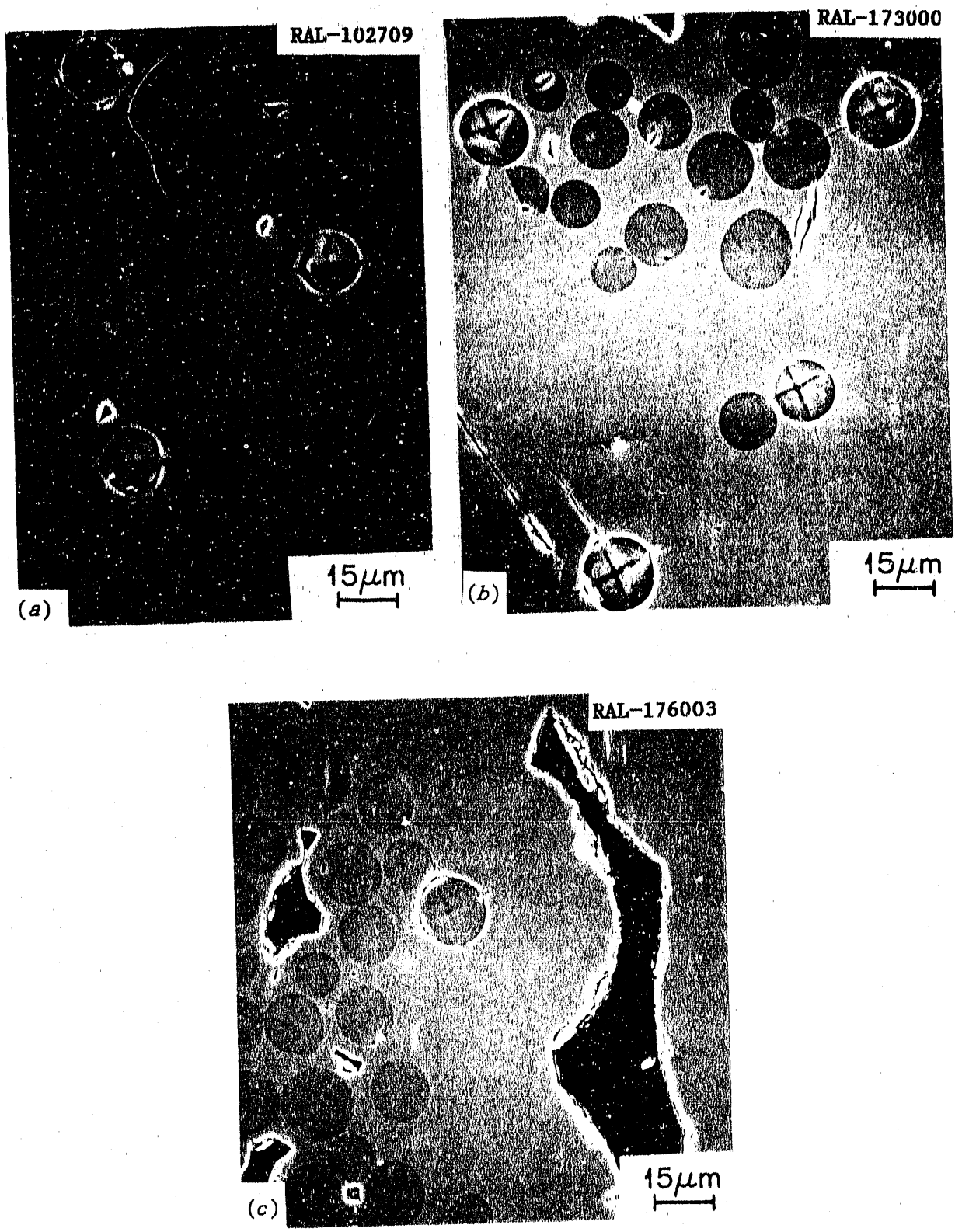

Figure 10.7. SEM micrographs showing indented Nicalon fibers: (*a*) CVI-178, uncoated Nicalon fibers; (*b*) CVI-173, SiC from methylsilane deposited at 1125 K; and (*c*) CVI-176, SiC from methylsilane deposited at 975 K.

steps demonstrates that silicon present in the gas phase during the fiber-coating process could react with the excess carbon in the fiber to form silicon carbide (Table 10.4). The reaction disturbs the chemistry and morphology of the fiber, which results in mechanical property degradation.

10.4.2 Elemental silicon

The presence of the 0.17-μm silicon coating was verified using X-ray line scan data obtained using a JEOL 733 electron microprobe (Figure 10.8). The flexure specimens exhibited extremely low strength and brittle fracture and no evidence of fiber pull-out or reinforcement. This behavior is displayed in the fracture surfaces and in the load-displacement curve in Figure 10.9.

Indentation measurements demonstrated that the silicon layer produced extremely high interfacial bonding in the sample. A load of 3 N was required to displace the fibers, and in most tests, the loads heavily damaged the fiber and the surrounding matrix. Extensive cracking of the matrix and crushing of the fibers suggests that the interfacial stresses were approaching the useful limits of the indentation method (Figure 10.10).

As with the previous specimens, thermochemical examination of the system suggests the silicon can diffuse into the fiber during interlayer deposition or during further processing. The silicon can react with the free carbon to form SiC, which can damage the integrity of the reinforcement. Tensile testing to determine the strength of the silicon-coated fiber tows was impossible because the specimens failed during heat treatment.

Table 10.4. Thermochemical evaluation of the system containing uncoated and SiC-coated fibers.

Uncoated fibers

1. $SiC + SiO_2 + C + CH_3SiCl_3 + 10H_2 \xrightarrow[100KPa]{1473K} 2\ SiC + 0.9\ SiO_2 + 0.8\ C + 10.1\ H_2 + 2.8\ HCl + 0.2\ CO$

2. $SiO_2 + CH_3SiCl_3 + 10H_2 \xrightarrow[100KPa]{1473K} 0.9\ SiO_2 + 0.9\ SiC + 10.2\ H_2 + 2.6\ HCl + 01\ CO + 0.1\ SiCl_x$

Nicalon fibers in an HCl containing environment:

$SiC + SiO_2 + C + HCl \xrightarrow[100KPa]{1473K} 0.8\ SiC + SiO_2 + 0.2\ C + 0.4\ HCl + 0.3\ H_2 + 0.1\ SiCl_x$

Silicon carbide from methylsilane[a]

1. $SiC + SiO_2 + C + SiH_4 + CH_4 \xrightarrow[3.3KPa]{975K} 2\ SiC + SiO_2 + 0.98\ C + 3.96\ H_2 + 0.02\ CH_4$

$SiC + SiO_2 + C + SiH_4 + CH_4 \xrightarrow[3.3KPa]{1125K} 2\ SiC + SiO_2 + C + 4\ H_2$

2. $SiO_2 + SiC \xrightarrow[100KPa]{1473K} SiO_2 + SiC$

3. $SiO_2 + SiH_4 + CH_4 \xrightarrow[3.3KPa]{1125K} SiO_2 + SiC + 4\ H$

[a]No thermodynamic data were available for CH_3SiH_3; thus, an analogous system containing SiH_4 and CH_4 was considered.

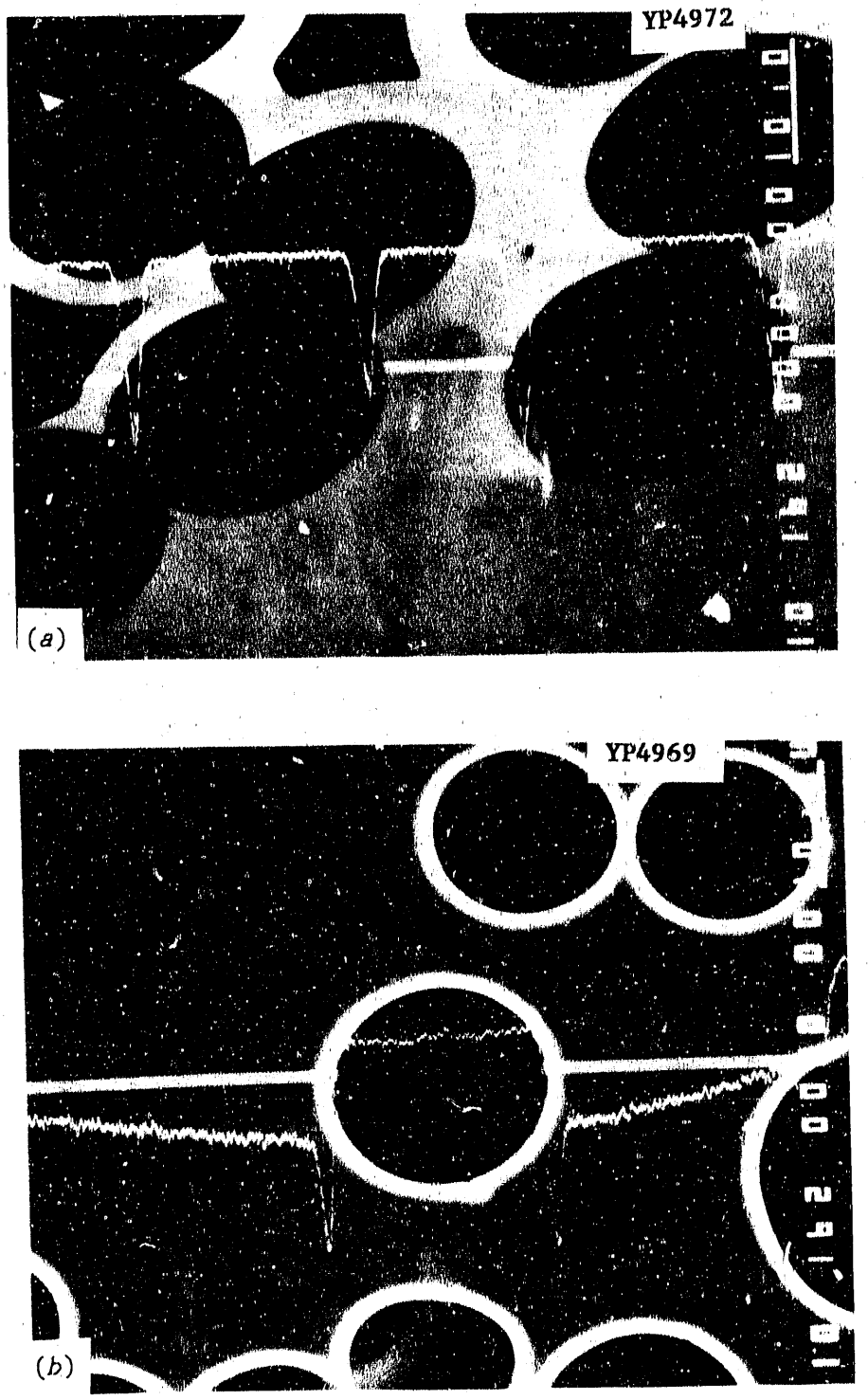

Figure 10.8. The presence of the thin films was verified using microprobe line scan data: (*a*) silicon coating on Nicalon fibers in SiC matrix, and (*b*) boron coating on Nicalon fibers in SiC matrix.

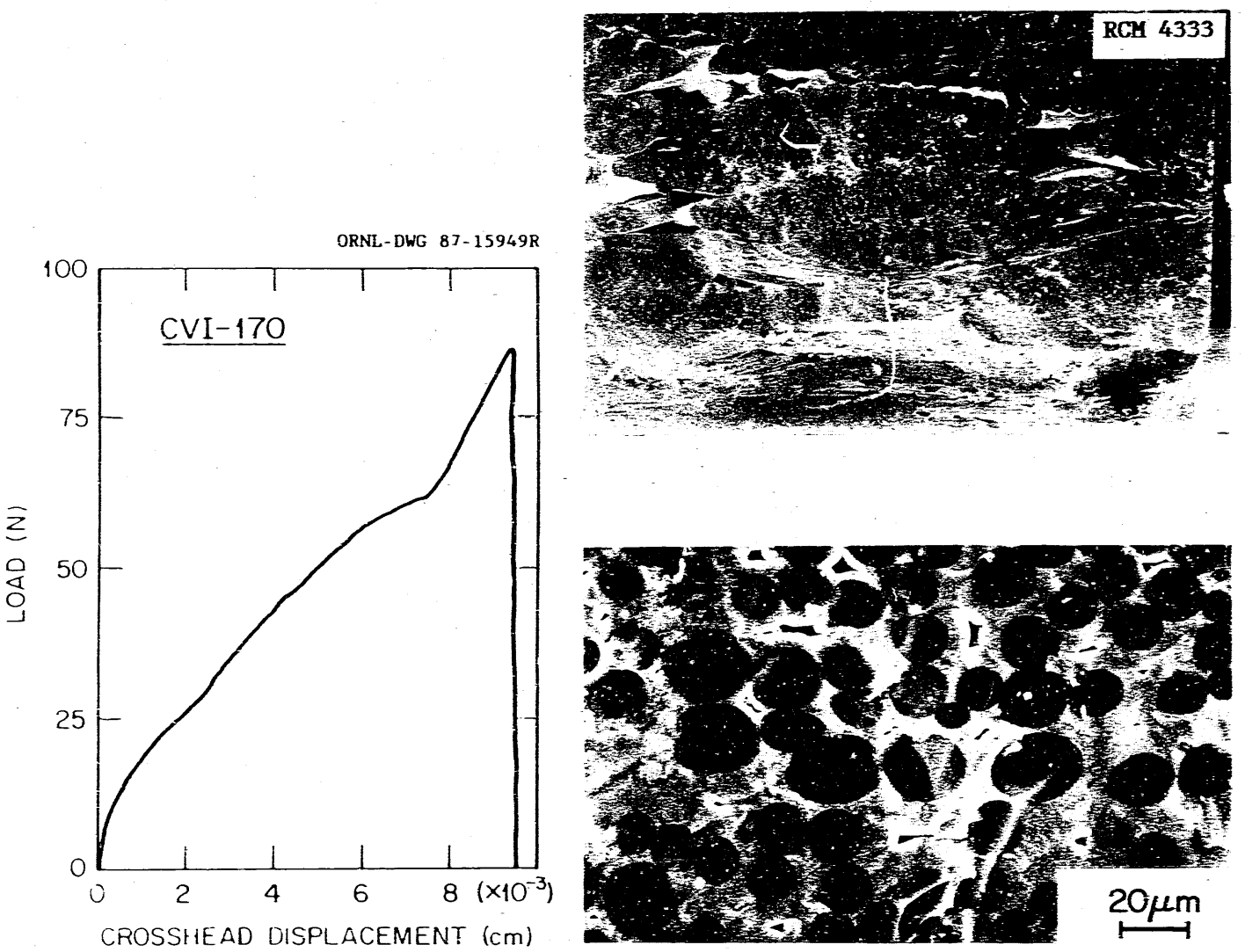

Figure 10.9. Load-displacement curve and fracture surfaces of specimens containing Nicalon fibers coated with silicon.

Figure 10.10. SEM micrograph showing indented silicon-coated Nicalon fibers.

Analysis of the matrix-deposition process reveals that the conversion of the silicon layer to silicon carbide is the favored reaction (Table 10.5). The intermediate coating becomes the silicon source in the deposition process, and the silicon-containing species in the reactant methyltrichlorosilane reacts with the excess hydrogen in the system to form various chlorosilanes. Earlier calculations have shown that a silicon-rich coating is favored at the given infiltration conditions (42). The result is methane in the gas phase, and when elemental silicon is present, methane in the gas mixture will react to form silicon carbide. This reaction may explain the extreme strength of the bonding between the matrix and the elemental silicon precoat.

Auger analysis of the fracture surface of a specimen having silicon as an intermediate layer was complicated by the smooth fracture surfaces and the lack of fiber pull-out. Fiber surfaces and pull-out grooves were elusive features; however, with diligent searching, useful areas were found. The majority of the observed surfaces of the fibers and pull-out grooves were rough in texture, most likely because of the formation of reaction zones at the boundary and the subsequent intense bonding. High silicon concentrations were recorded for both the fiber surfaces and the pull-out grooves (Figure 10.11).

10.4.3 Carbon interlayers

Carbon coatings were produced by the cracking of propylene gas at 1375 K and reduced pressure. The concentration of the propylene was varied to produce carbon coatings that ranged in thickness from 0.10 to 0.28 μm. The thickness of the interfacial layer was measured from the weight gained during interlayer deposition. The JEOL 733 electron

Table 10.5. Thermochemical evaluation of the system containing silicon-coated Nicalon fibers.

Silicon interface coating

1. $SiC + SiO_2 + C + SiH_4 \xrightarrow[3.3KPa]{675K} 2\ SiC + SiO_2 + 2\ H_2$

2. $SiC + SiO_2 + C + Si \xrightarrow[100KPa]{1475K} 2\ SiC + SiO_2$

3. $SiO_2 + SiH_4 \xrightarrow[3.3KPa]{675K} SiO_2 + Si + 2\ H_2$

4. $SiO_2 + Si \xrightarrow[100KPa]{1475K} SiO_2 + Si$

5. $Si + CH_3SiCl_3 + 10\ H_2 \xrightarrow[100KPa]{1473K} SiC + 0.29\ Si + 10.9\ H_2 + 1.1\ HCl + 0.71\ SiCl_xH_y$

6. $SiC + Si \xrightarrow[100KPa]{1475K} SiC + Si$

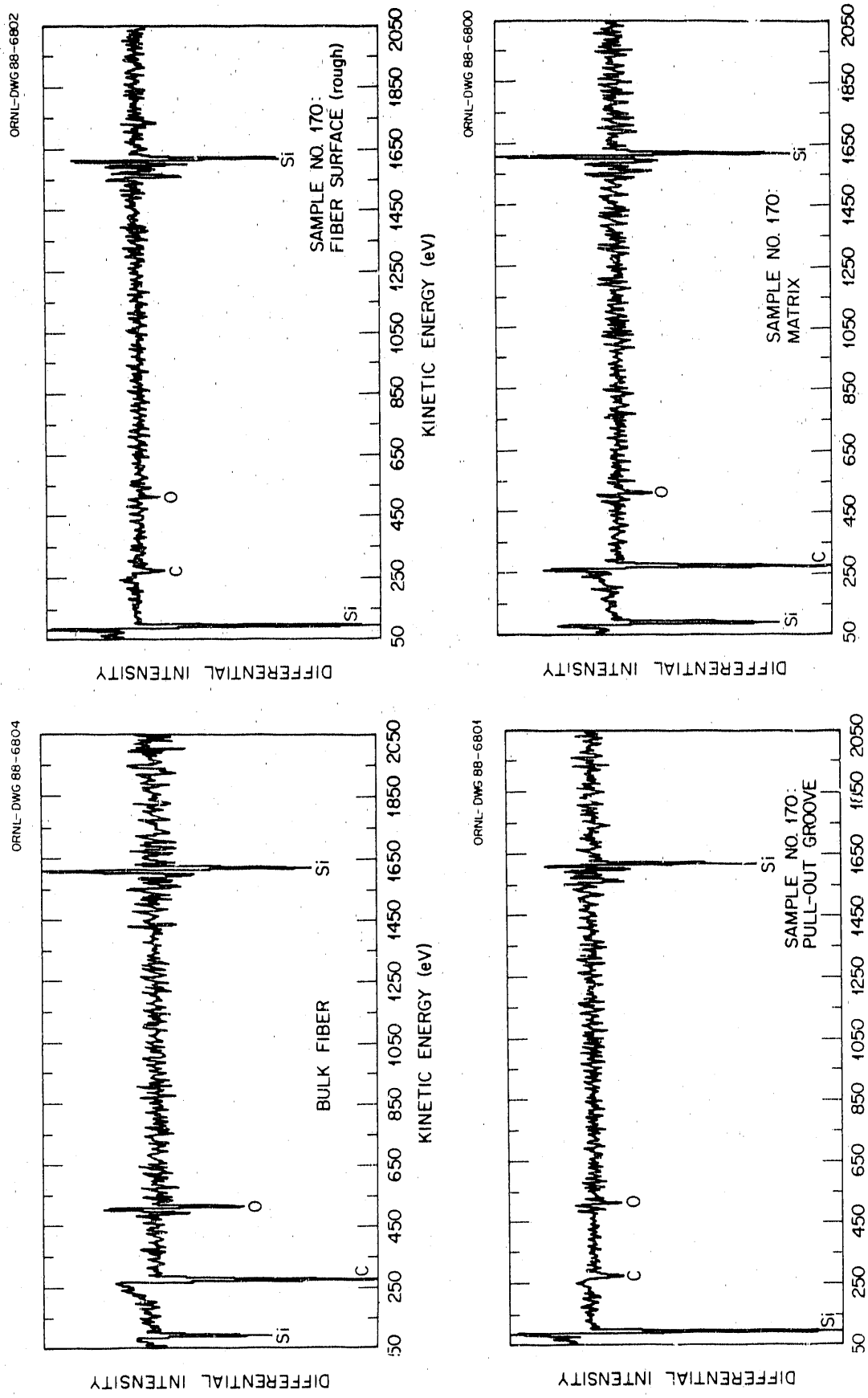

Figure 10.11. AES analysis of fracture surface features for an SiC composite specimen containing Nicalon fibers coated with a silicon intermediate layer.

microprobe was not equipped to detect the carbon coatings; thus, polarized light micrographs were required to verify the presence of the carbon layers. Examples of polarized light micrographs are shown in Figure 10.12. The thickness of the carbon coating had a significant effect on the strength and fracture of the specimens.

The load displacement curves and SEM photographs of fracture surfaces for the carbon-coated composites are shown in Figure 10.13. The thicker layers produced the most desirable results, a combination of higher strength and the greatest strain to failure. The interfacial frictional stress was found to be inversely proportional to the coating thickness. The measured values ranged from 0.6 $\pm$ 0.4 MPa to 11.3 $\pm$ 4.7 MPa (Figure 10.14).

Thermochemical calculations show that a carbon layer should be inert with r ,pect to the fibers and matrix. A reaction between the carbon and the silica layer at the fiber surface could occur during the carbon-layer-deposition process (Table 10.6). Thus, silicon carbide would be expected to form a strong bond between the fiber and the carbon coating. SEM photomicrographs and Auger elemental analysis of fracture surface features support these results. Using Auger elemental spectra to analyze the surface of the fiber, a single carbon peak was found, whereas silicon and carbon were found in the pull-out grooves (Figure 10.15).

10.4.4 Oxidized sample

The weight loss for the heat-treated pieces appeared relatively low, suggesting that the oxidation of the carbon interlayer was not complete. The weight losses for the specimens were: 0.3% for the specimen from the top area, 0.75% for the middle, and 0.86% for the bottom. The

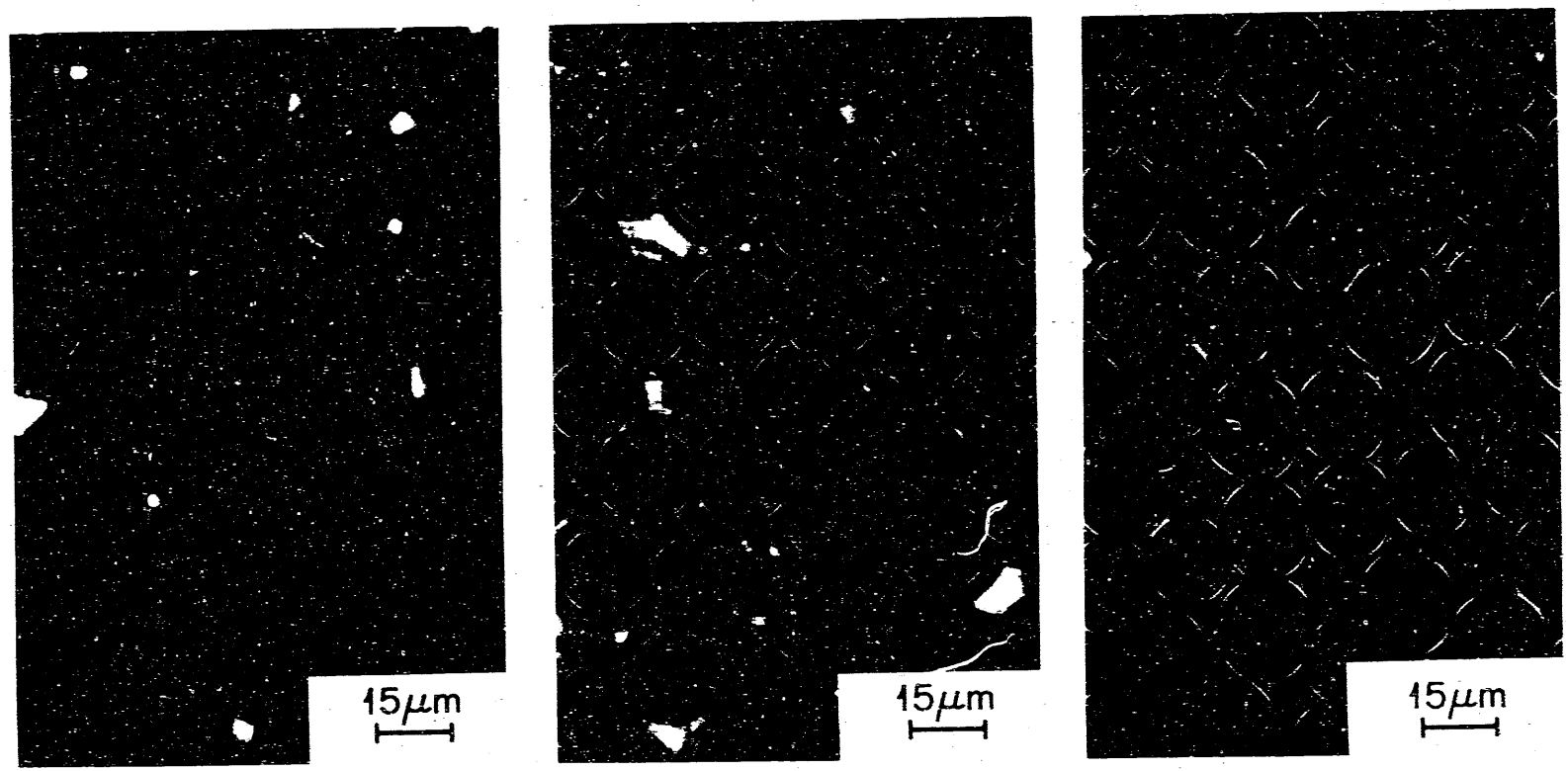

(*a*) (*b*) (*c*)

Figure 10.12. Polarized light micrographs of the carbon-coated samples: (*a*) CVI-175, (*b*) CVI-171, and (*c*) CVI-174.

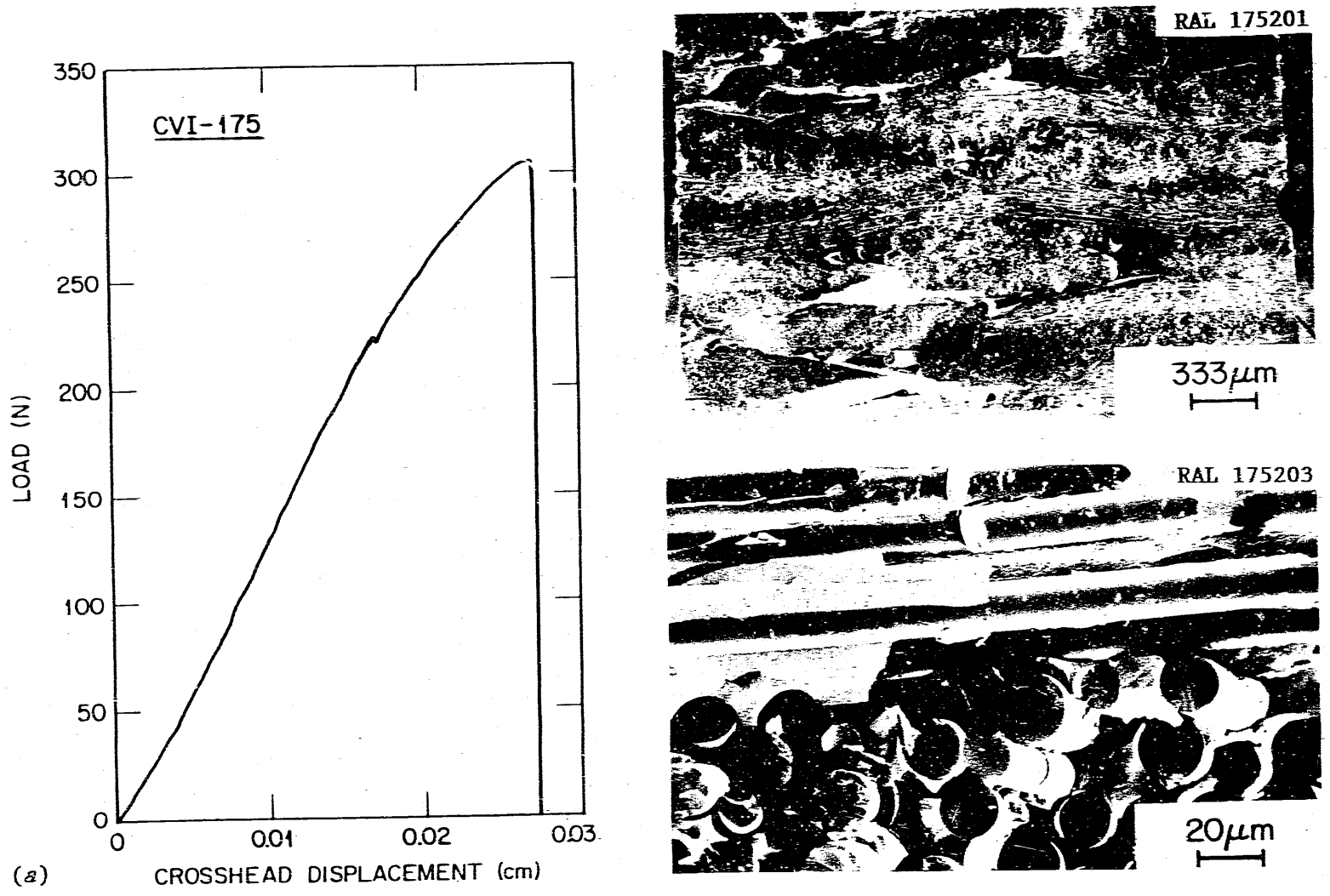

Figure 10.13. Load-displacement curves and fracture surfaces of specimens containing Nicalon fibers coated with a carbon intermediate layer prior to infiltration: (*a*) CVI-175, 0.10-μm carbon layer; (*b*) CVI-171, 0.17-μm carbon layer; and (*c*) CVI-174, 0.28-μm carbon layer.

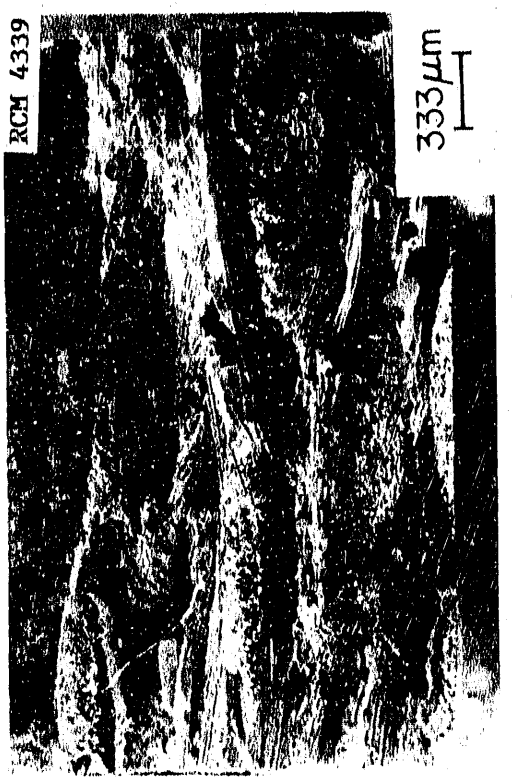

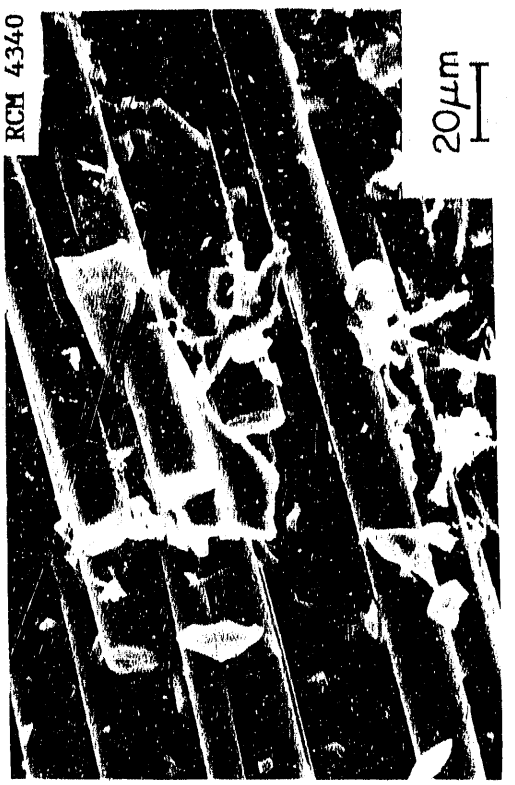

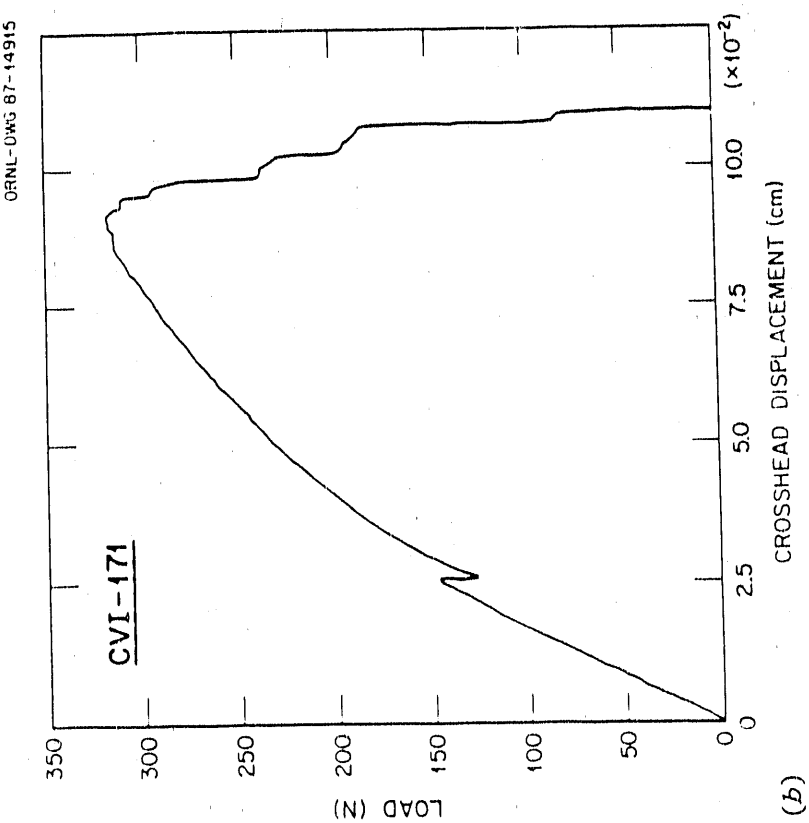

(b)

Figure 10.13 continued

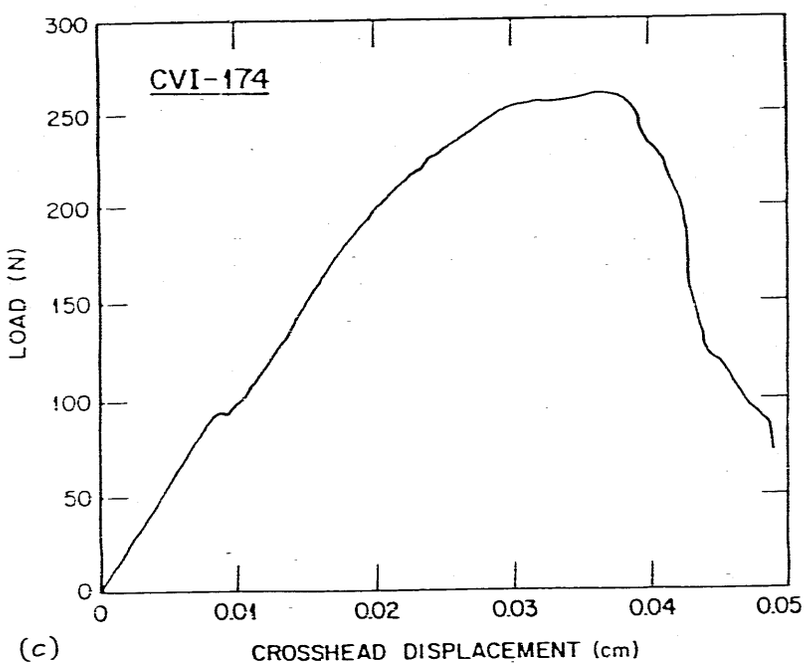

(c)

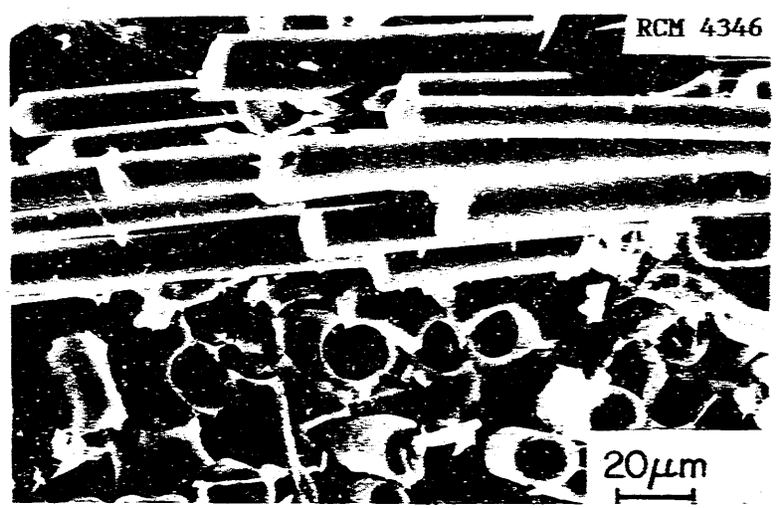

Figure 10.13 continued

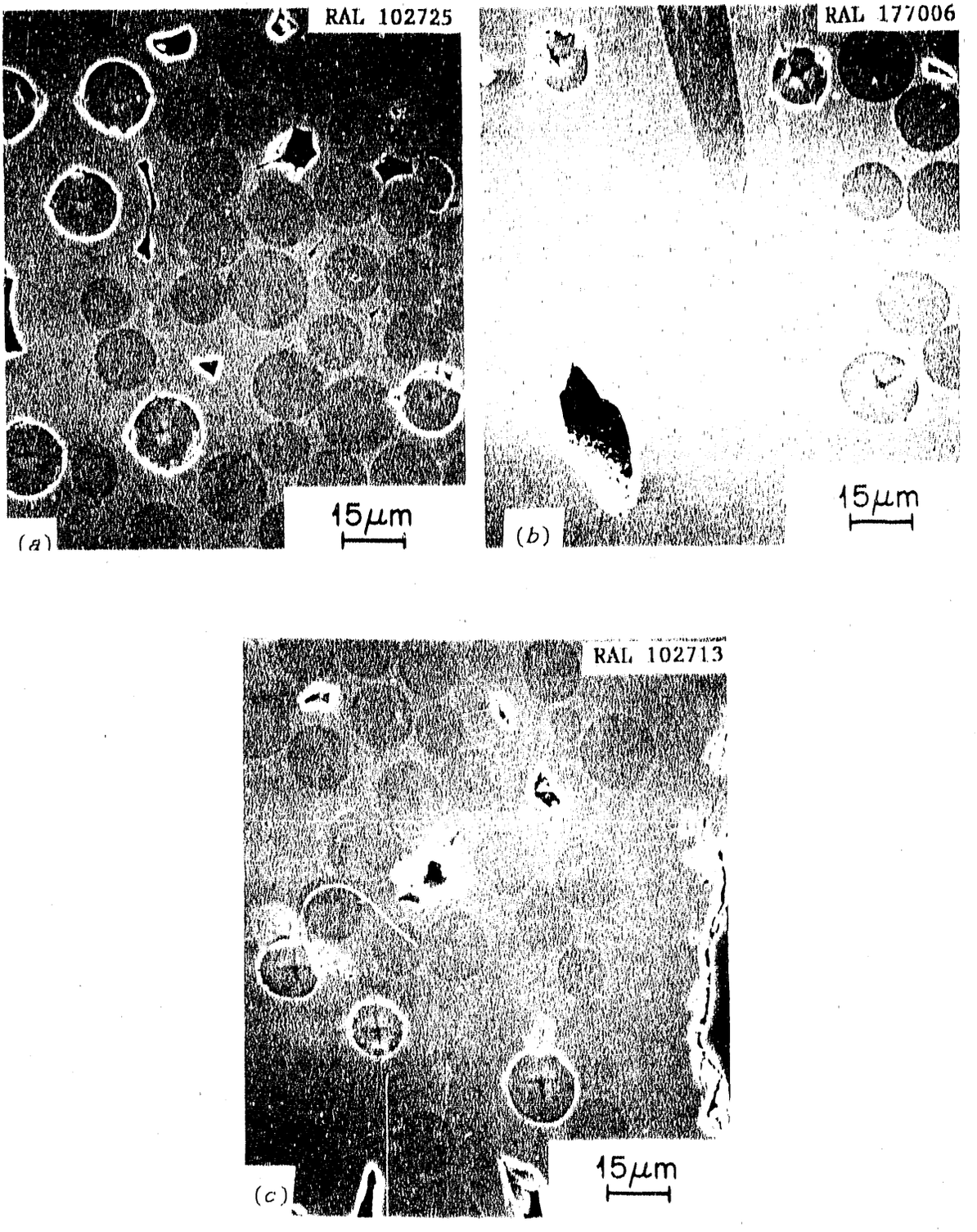

Figure 10.14. SEM micrographs of indented carbon-coated Nicalon fibers in a CVI SiC matrix: (*a*) CVI-174, (*b*) CVI-171, and (*c*) CVI-175.

Table 10.6. Thermochemical evaluation of the system containing carbon-coated Nicalon fibers.

Carbon coating

1. $SiC + SiO_2 + C + C_3H_6 \xrightarrow[3.3KPa]{1373K} 1.1\ SiC + 0.9\ SiO_2 + 3.6\ C + 3\ H_2 + 0.2\ CO$

2. $SiC + SiO_2 + C \xrightarrow[100KPa]{1473K} SiC + SiO_2 + C$

3. $SiO_2 + C_3H_6 \xrightarrow[3.3KPa]{1373K} 0.9\ SiO_2 + 0.1\ SiC + 2.6\ C + 3\ H_2 + 0.3\ CO$

4. $SiO_2 + C \xrightarrow[100KPa]{1473K} SiO_2 + C$

5. $C + CH_3SiCl_3 + 10H_2 \xrightarrow[100KPa]{1473K} 0.9\ SiC + 1.1\ C + 10.1\ H_2 + 2.8\ HCl + 0.1\ SiCl_x$

6. $SiC + C \xrightarrow[100KPa]{1473K} SiC + C$

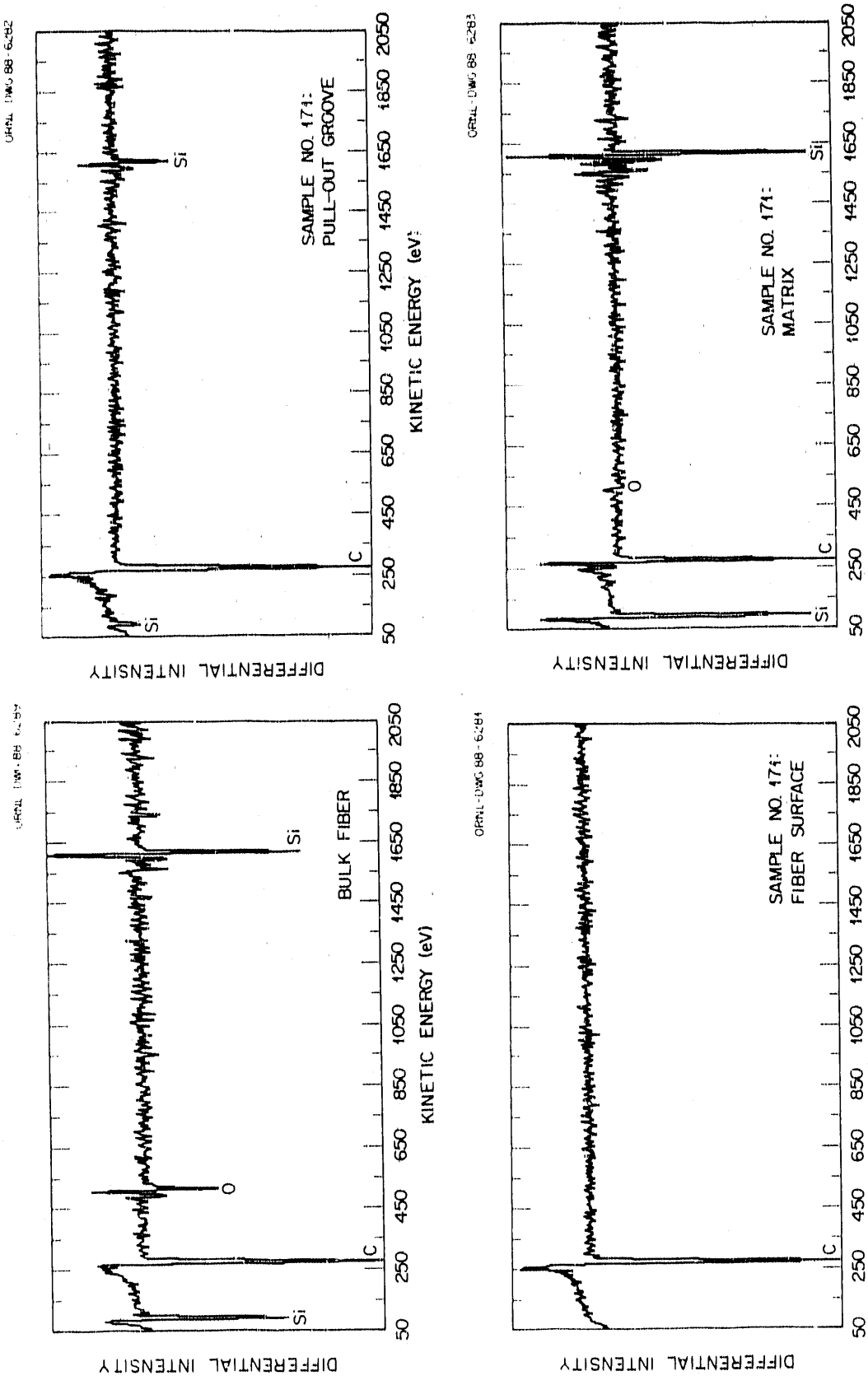

Figure 10.15. AES analysis of fracture surface features for an SiC composite specimen containing Nicalon fibers coated with a carbon intermediate layer.

predicted weight loss was 3%. The flexure results confirmed this suspicion. Only the flexure bars cut from the edge closest to the original cut surface exhibited the expected low strength. The oxidation temperature was kept low to minimize possible matrix damage. This did not allow for the total removal of the carbon layer even though pure oxygen was used to increase the oxidation rate.

However, the few specimens did yield useful results. The flexure strengths of the treated and unoxidized specimens are listed in Table 10.1. The oxidized specimens possessed lower matrix fracture strengths and decreased ultimate strength compared with the untreated specimens from the composite sample. Representative flexure curves and photographs of fracture surfaces for oxidized and untreated specimens are shown in Figures 10.16 and 10.17.

10.4.5 Boron coating

The presence of a boron coating was verified using X-ray line scan data (Figure 10.8). The composite exhibited low flexure strength and little strain-to-failure. This is depicted in the fracture surfaces and the load-displacement curve in Figure 10.18(*a*). A small degree of fiber pull-out is evident in the SEM photographs, and a closer examination of the fracture surfaces showed the fiber pull-out grooves to be rough and have crystalline appearance (Figure 10.19). A number of fibers also possessed a reaction zone noted by discoloration and an inner boundary line.

Thermodynamic evaluation of the coating processes and the stability of the boron in contact with the fibers or matrix predicts that a series of reactions may develop at the interfaces (Table 10.7). Some of these

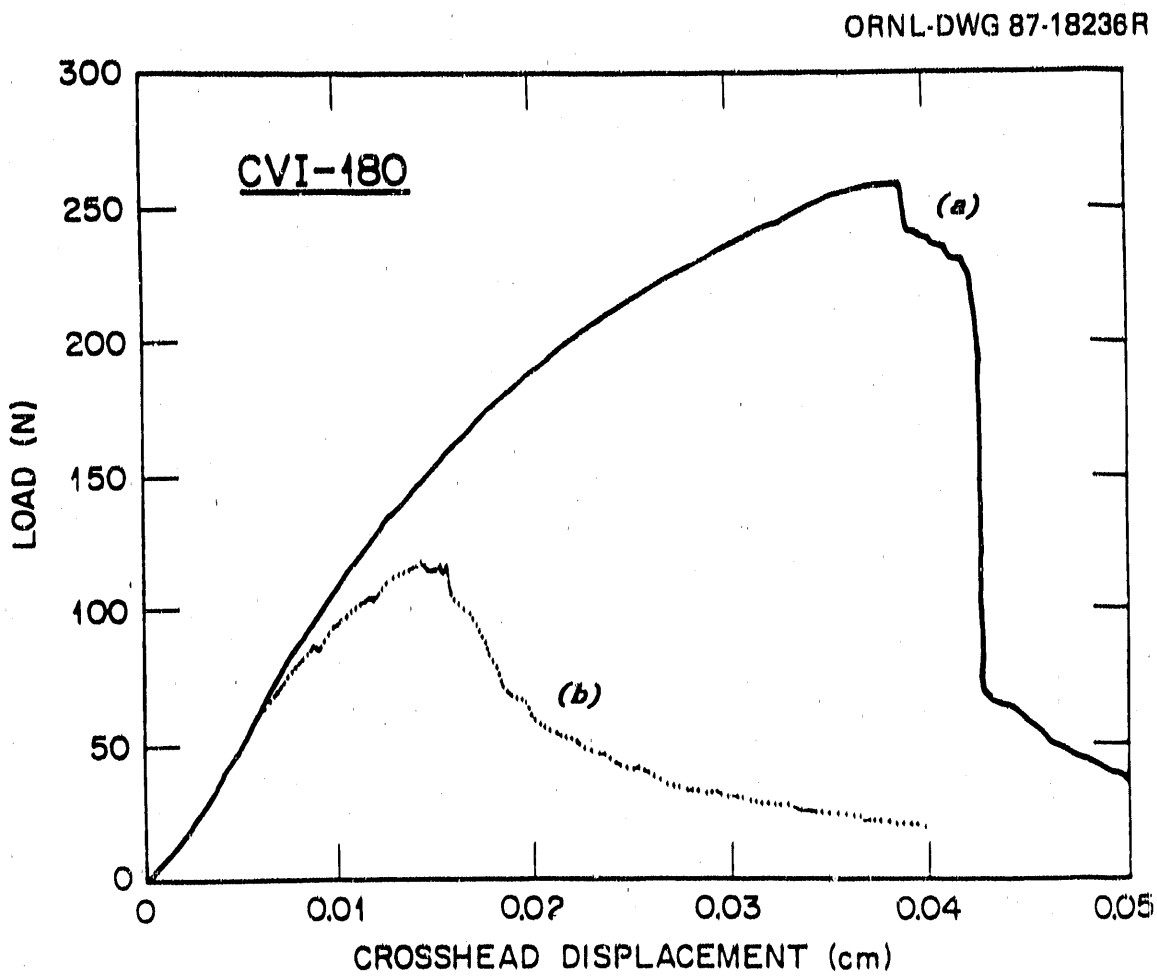

Figure 10.16. Load-displacement curves for specimens containing Nicalon fibers with a carbon intermediate layer: (*a*) as fabricated and (*b*) after heating to 1125 K for 44 hours in flowing oxygen.

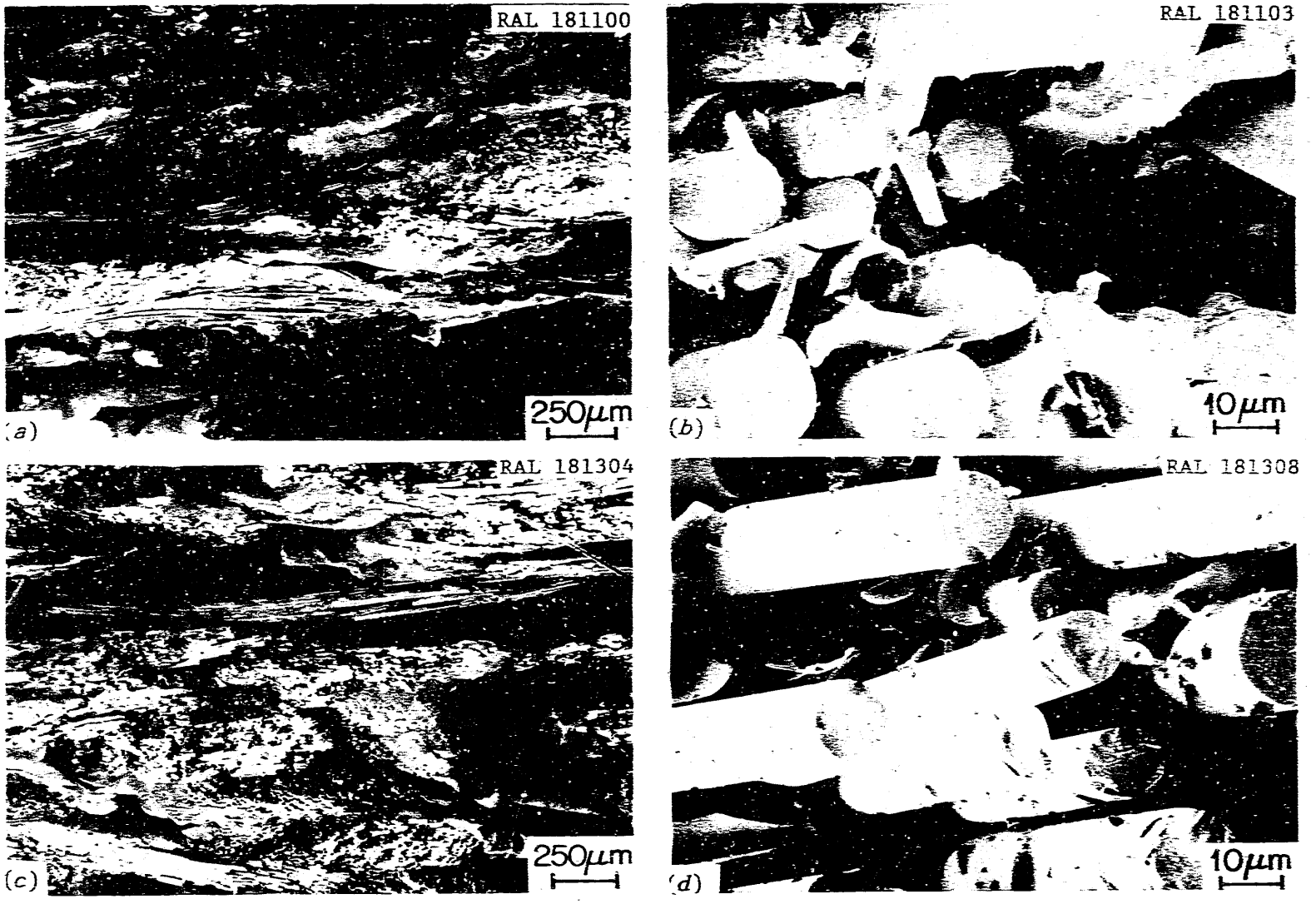

Figure 10.17. SEM micrographs of the fracture surfaces of specimens containing Nicalon fibers with a carbon intermediate layer: (*a*) and (*b*) as fabricated and (*c*) and (*d*) after heating to 1125 K for 44 hours in flowing oxygen.

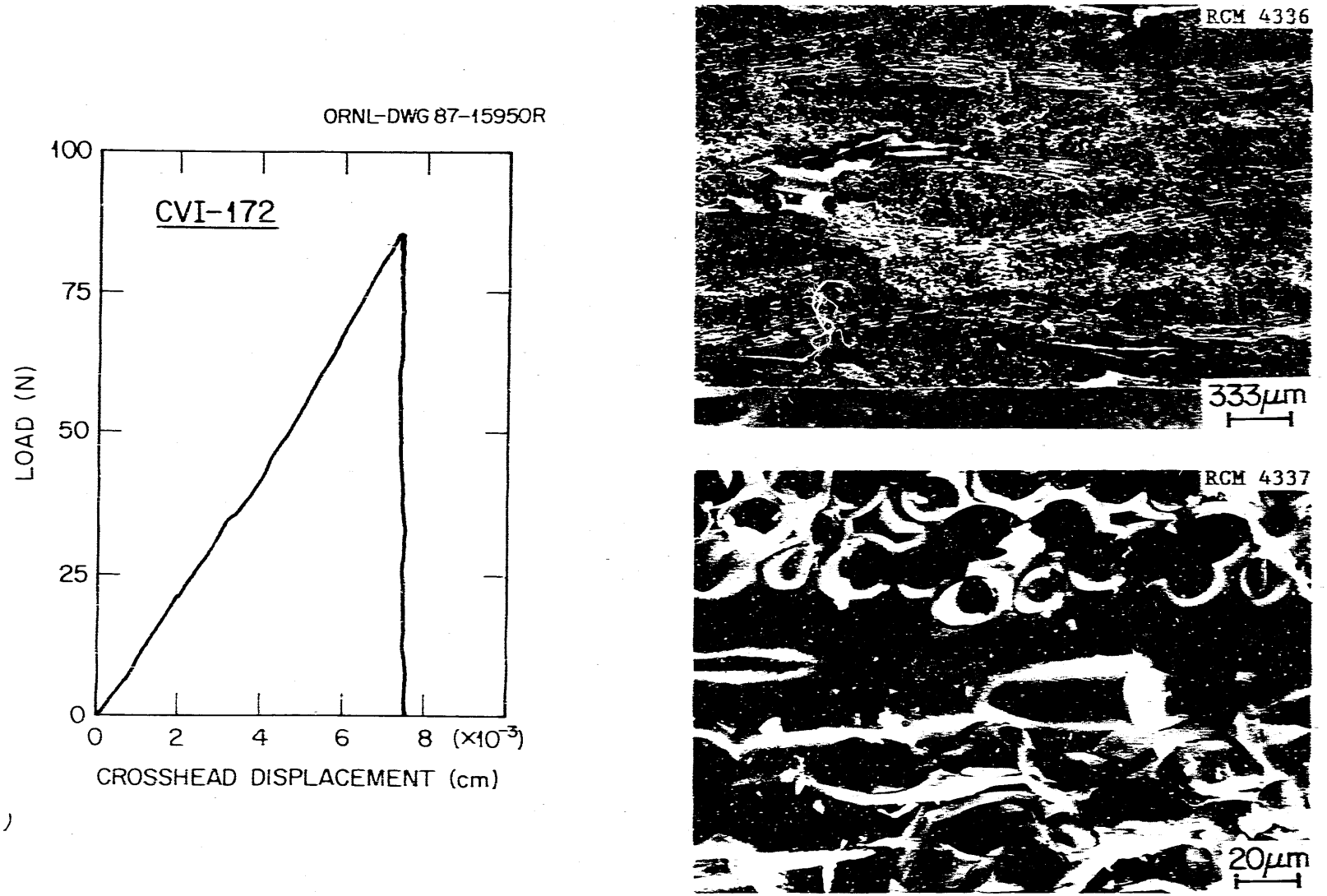

Figure 10.18. Load-displacement curves and fracture surfaces of specimens fabricated from Nicalon fibers coated with boron-containing intermediate layers prior to infiltration: (*a*) elemental boron and (*b*) boron nitride from diborane and ammonia.

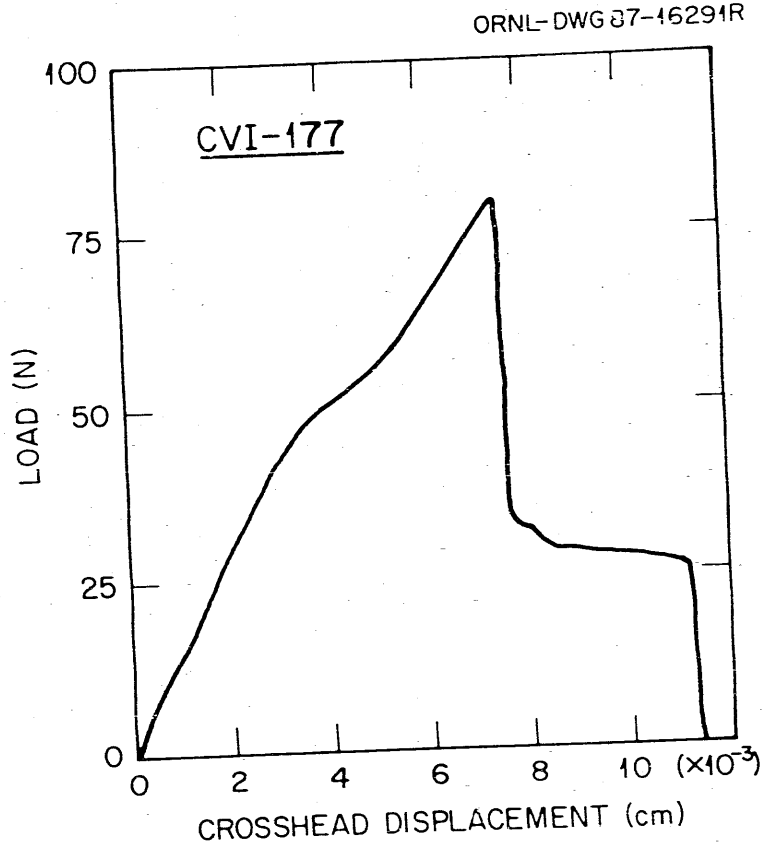

(b)

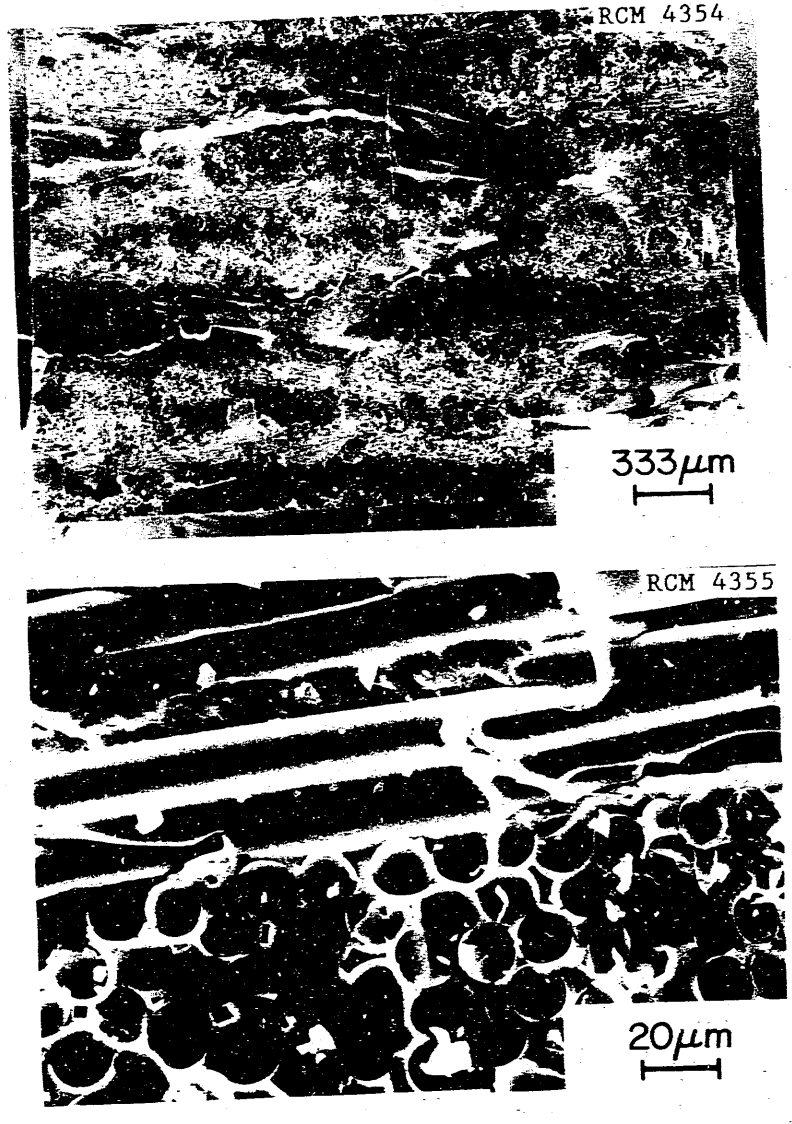

Figure 10.18 continued

RAL 033021

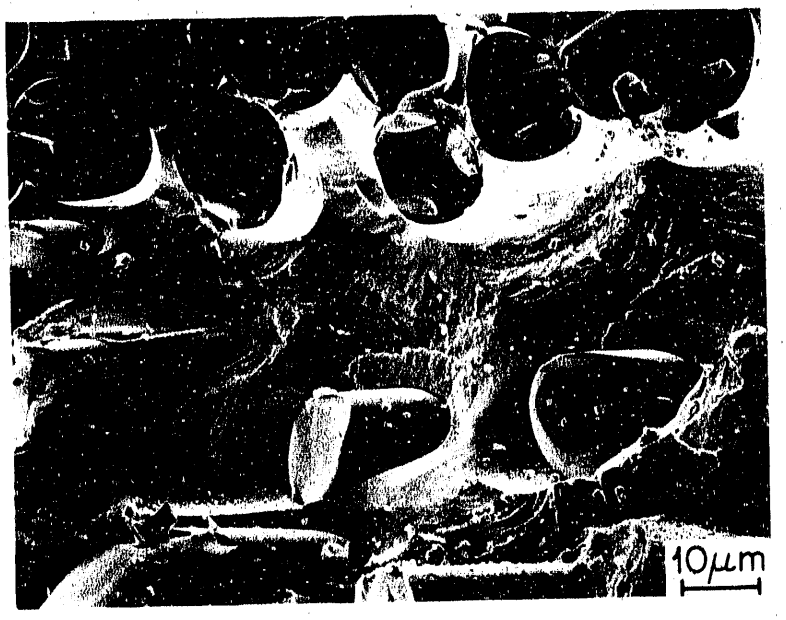

RAL 033023

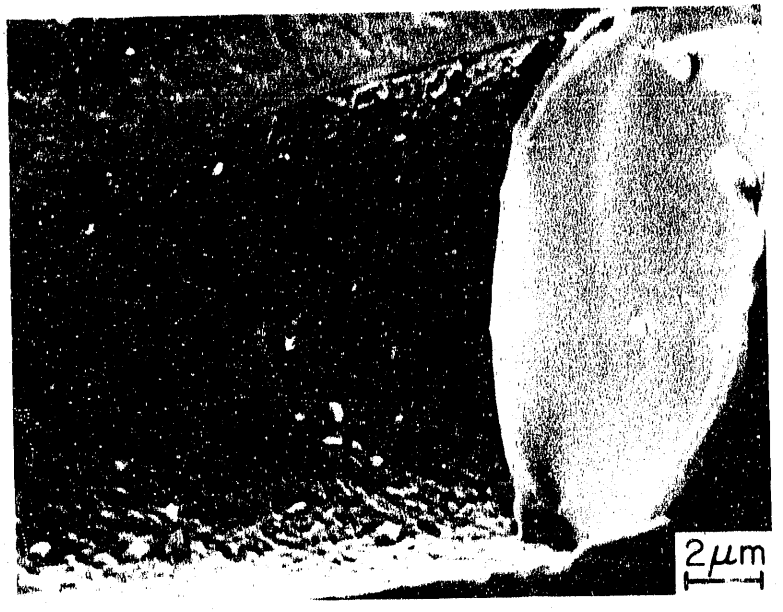

Figure 10.19. Higher-magnification SEM analysis of fractured boron-coated fiber specimens showing evidence of chemical interaction at the fiber-matrix interface and within the fiber.

Table 10.7. Thermochemical evaluation of the system containing boron-coated Nicalon fibers.

Boron interface coating:

1. $SiC + SiO_2 + C + B_2H_6 \xrightarrow[3.3KPa]{775K} SiC + SiO_2 + 0.32\ C + 0.5\ B_4C + 2.64\ H_2 + 0.18\ CH_4$

2. $SiC + SiO_2 + C + B \xrightarrow[100KPa]{1473K} 1.75\ SiC + 0.25\ SiO_2 + 0.25\ C + 0.5\ B_2O_3$

3. $SiO_2 + B_2H_6 \xrightarrow[3.3KPa]{775K} SiO_2 + 2\ B + 3\ H_2$

4. $SiO_2 + B \xrightarrow[100KPa]{1473K} SiO_2 + B$

5. $B + CH_3SiCl_3 + 10\ H_2 \xrightarrow[100KPa]{1473K} 0.8\ SiC + 0.2\ B_4C + 10.5\ H_2 + 1.9\ HCl + 0.17\ SiCl_x + 0.1\ BCl_3$

6. $SiC + B \xrightarrow[100KPa]{1473K} 0.75\ SiC + 0.25\ Si + 0.25\ B_4C$

include: the reaction of boron with carbon to form boron carbide, the reduction of SiC to Si and B_4C, and the reaction of boron and SiO_2 to produce B_2O_3. Carbon is present in the fibers and in the gases during matrix deposition. Silica is found at the fiber surface and in the bulk of the fiber. The matrix is SiC. The chemical reactivity of boron in the system would lead to the conclusion that a moderately strong bond between the fiber, the boron layer, and the matrix will be present. Indentation of fiber ends showed the interfacial stresses to be relatively low (6.3 ± 1.7 MPa [Figure 10.20(*a*)]. In earlier tests, fibers coated with boron at low temperatures retained a substantial portion of their original strength. Heat-treating similar fibers resulted in strengths of <165 MPa (see Table 10.3). A reaction zone can be seen in some of the fiber ends in the photomicrographs of Figure 10.19, therefore, it appears the boron disturbs the composition of the fiber, resulting in a significant reduction in strength.

Auger analysis of the pull-out grooves and fiber surfaces of fractured specimens having a boron coating on the fibers showed identical results for both areas (Figure 10.21). The silicon peaks were suppressed and carbon, boron, and oxygen showed strong intensities. This supports the hypothesis that the boron reacted with both the matrix and fiber during processing.

10.4.6 Boron nitride

The sample precoated with boron nitride (BN) from a diborane and ammonia mixture exhibited low strength and limited fiber pull-out; however, the calculated frictional stress of 15.7 ± 5.0 MPa for the BN-coated sample is moderate relative to the other composite samples [see Figures 10.18(*b*) and 10.20(*b*)]. It has been demonstrated in the past

RAL 102721

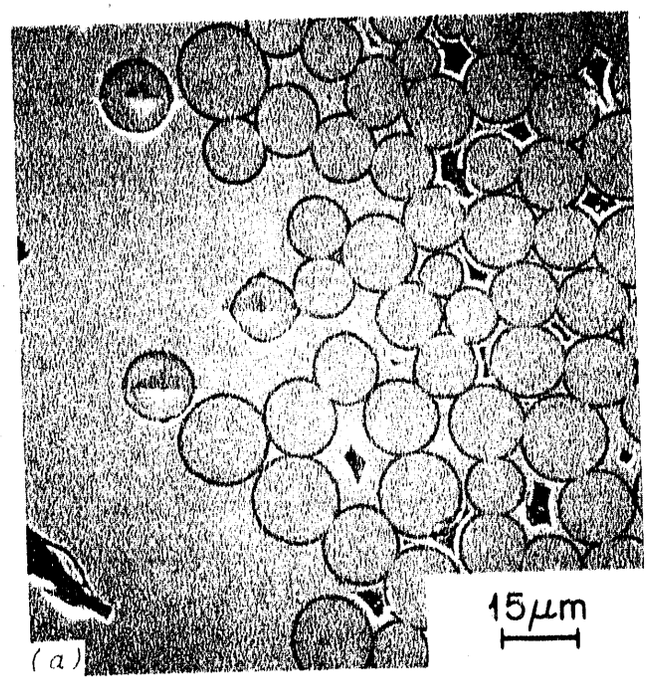

RAL 177002

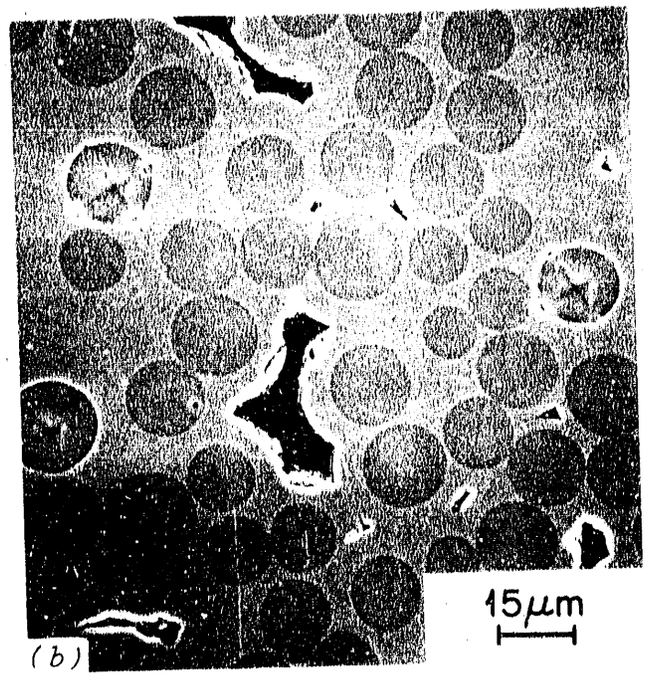

Figure 10.20. SEM micrographs of indented Nicalon fibers with (*a*) a boron coating and (*b*) a boron nitride layer.

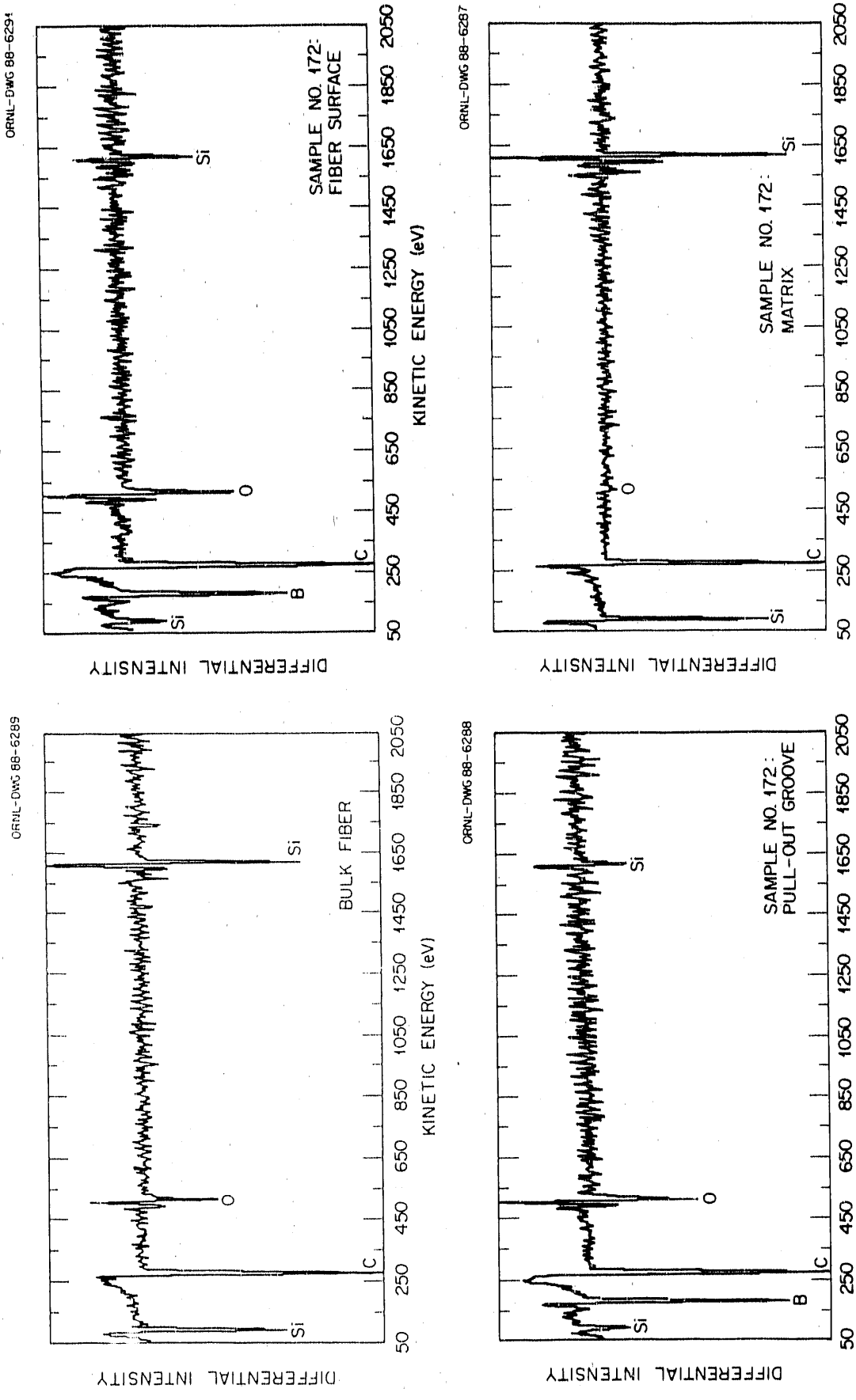

Figure i0.21. AES analysis of fracture surface features for an SiC composite specimen containing Nicalon fibers coated with a boron intermediate layer.

that BN coatings react with the Nicalon fibers and degrade the properties of the reinforcement. The tensile strengths of fibers coated with BN at low temperatures from a variety of reactants have been respectable; however, subsequent exposure to elevated temperatures has resulted in fiber damage (Table 10.3). It can be expected that the boron could act as stated in the case for an elemental boron coating although the thermochemical calculations show that the highly reactive nitrogen from the ammonia could also react with the SiC in the fibers, converting the carbide to the nitride (Table 10.8). Auger analysis was not completed for this sample.

10.4.7 Molybdenum

Molybdenum was a poor choice as an intermediate coating for the SiC-SiC system. Infiltration of the preform fabricated from molybdenum-coated fibers was difficult. The average density of flexure specimens prepared from the composite was only 74.4 ± 1.2% theoretical even though the densification process appeared complete as indicated by sufficient backpressure. The average flexure strength of the composite specimens was 57.2 ± 11.5 MPa, and the specimens exhibited brittle fracture as shown in the load-displacement curve and photomicrographs of the fracture surface of a flexure specimen shown in Figure 10.22. The interfacial frictional stress was measured to be 32.3 ± 6.0 MPa, and typical indent impressions are shown in Figure 10.23.

Thermochemical analysis of the system demonstrates the damaging effect of the presence of not only molybdenum but also flourine (Table 10.9). Molybdenum hexaflouride can react with any element or compound found in the fiber. SiC and SiO_2 are attacked during the interlayer deposition. The formation of SiC is hindered during

Table 10.8. Thermochemical evaluation of the system containing boron-nitride-coated Nicalon fibers.

Boron nitride coating

1. $SiC + SiO_2 + C + B_2H_6 + 3\ NH_3 \xrightarrow[3.3KPa]{875K} 0.25\ SiC + SiO_2 + 1.64\ C + 2\ BN + 0.25\ Si_3N_4 + 7.28\ H_2 + 0.11\ CH_4$

2. $SiC + SiO_2 + C + BN \xrightarrow[100KPa]{1473K} SiC + SiO_2 + C + BN$

3. $SiO2 + B_2H_6 + 2\ NH_3 \xrightarrow[3.3KPa]{875K} SiO_2 + BN + 6\ H_2$

4. $SiO_2 + BN \xrightarrow[100KPa]{1473K} SiO_2 + BN$

5. $BN + CH_3SiCl_3 + 10H_2 \xrightarrow[100KPa]{1473K} 1.0\ BN + 0.9\ SiC + 0.1\ C + 10.1\ H_2 + 2.8\ HCl + 0.1\ SiCl_x$

6. $SiC + BN \xrightarrow[100KPa]{1473K} SiC + BN$

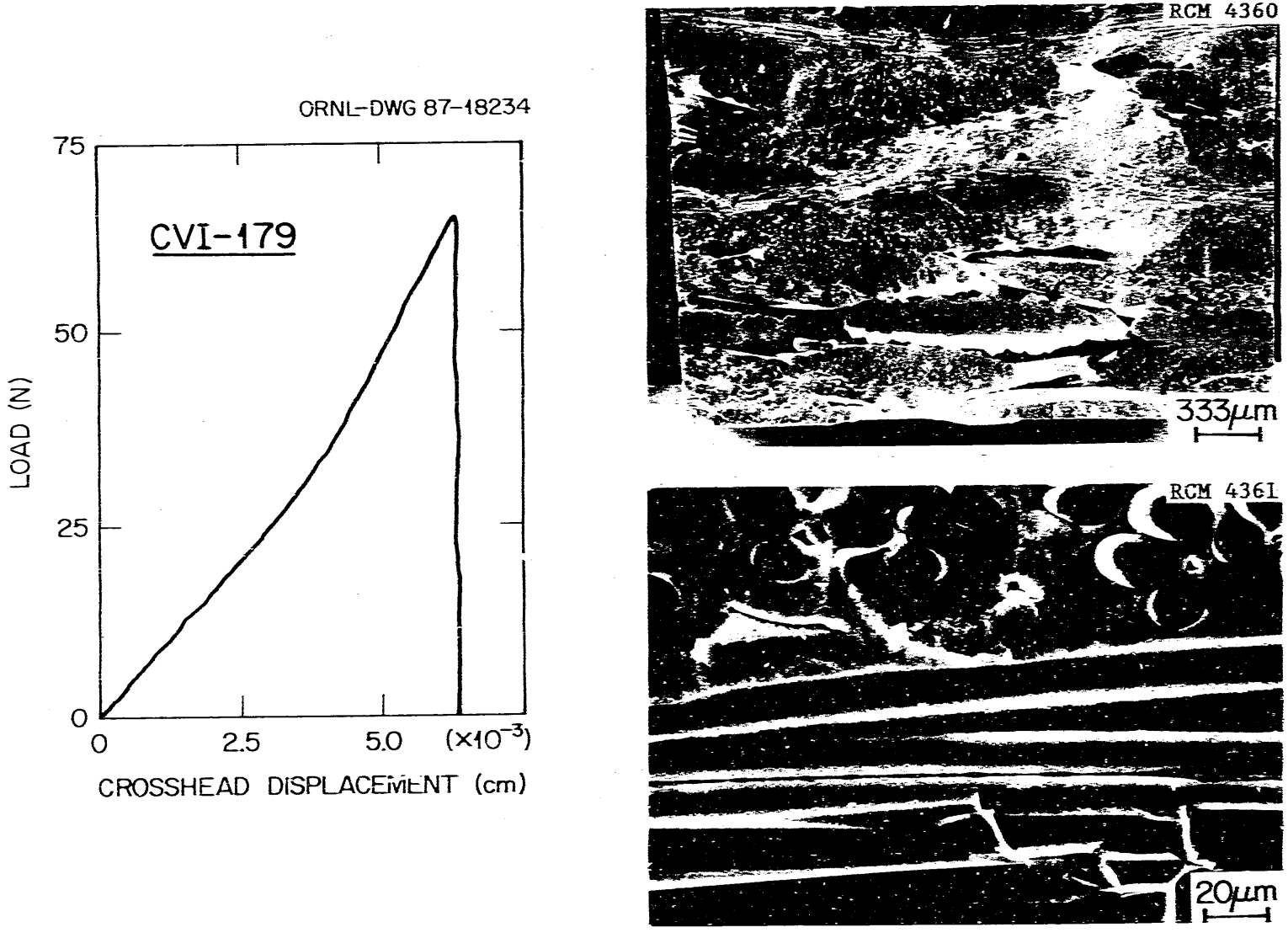

Figure 10.22. Load-displacement curve and fracture surfaces of specimens fabricated from Nicalon fibers coated with a molybdenum intermediate layer prior to infiltration.

RAL 102744

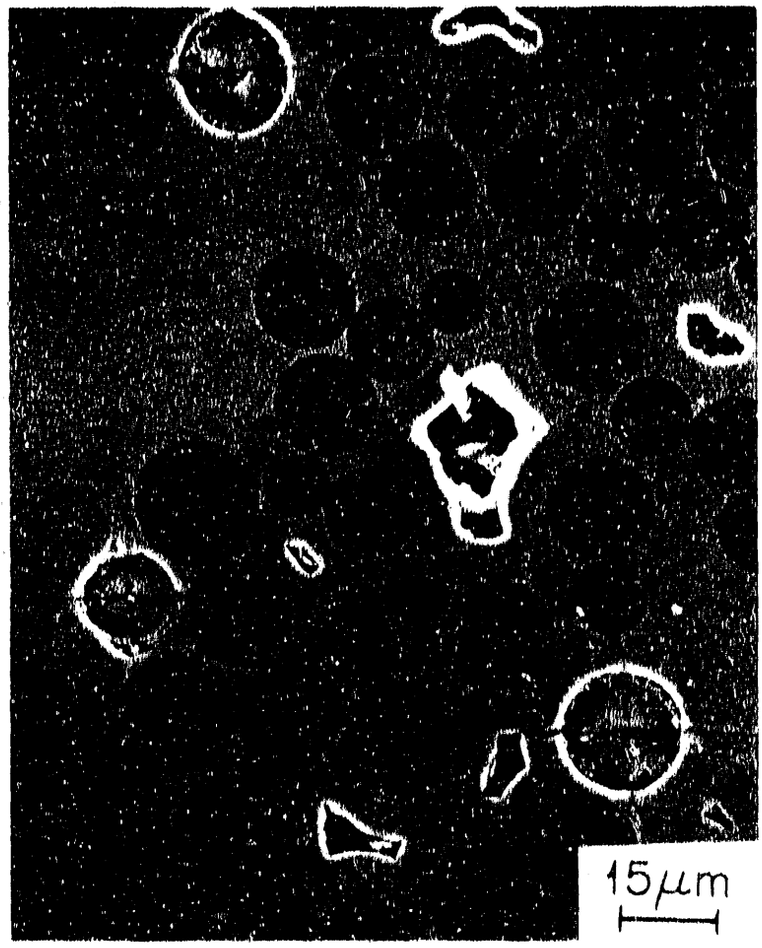

Figure 10.23. SEM micrographs of indented molybdenum-coated Nicalon fibers in an SiC matrix.

Table 10.9. Thermochemical evaluation of the system containing molybdenum-coated Nicalon fibers.

Molybdenum coating

1. $SiC + SiO_2 + C + MoF_6 + 10\ H_2 \xrightarrow[3.3KPa]{1125K} 0.6\ SiO_2 + 0.7\ C + 0.5\ Mo_2C + 9.4\ H_2 + 1.4\ SiF_4 + 0.6\ CO + 0.5\ HF + 0.1\ CH_4 + 0.1\ H_2O$

2. $SiC + SiO_2 + C + Mo \xrightarrow[100KPa]{1473K} 0.4\ SiC + SiO_2 + 1.6\ C + 0.2\ Mo_5Si_3$

3. $SiO_2 + MoF_6 + 10\ H_2 \xrightarrow[3.3KPa]{1125K} 0.4\ Mo + 0.6\ MoO_2 + SiF_4 + 8.2\ H_2 + 2\ HF + 0.8\ H_2O$

4. $SiO_2 + Mo \xrightarrow[100KPa]{1473K} SiO_2 + Mo$

5. $Mo + CH_3SiCl_3 + 10H_2 \xrightarrow[100KPa]{1473K} 0.3\ SiC + 0.7\ C + 0.2\ Mo_5Si_3 + 10.1\ H_2 + 2.8\ HCl + 0.1\ SiCl_x$

6. $SiC + Mo \xrightarrow[100KPa]{1473K} 0.4\ SiC + 0.6\ C + 0.2\ Mo_5Si_3$

Nicalon fibers in an HF containing environment

$SiC + SiO_2 + C + HF \xrightarrow[3.3KPa]{1125K} 0.75\ SiC + SiO_2 + 1.25\ C + 0.5\ H_2 + 0.25\ SiF_4$

---

infiltration by the preferred production of Mo_5Si_3. This also can lead to a carbon enrichment of the fiber surface-intermediate coating boundary. The reactions exacerbate fiber-degradation mechanisms.

Molybdenum was not as evident as expected in the Auger spectral analyses (Figure 10.24). The three Mo peaks that occur at 160, 186, and 217 eV were extremely weak compared with those for carbon, silicon, and oxygen (Appendix A). Molybdenum could be found in some areas of the matrix and fibers of a specimen but not in all regions of the same specimen. As predicted by the thermochemical calculations, carbon-enrichment was observed at fiber surfaces and in pull-out grooves.

10.5 Fragmented Coatings on Individual Filaments

10.5.1 Large-diameter filaments

Initial tests were performed on AVCO SCS-6 filaments with only a silicon carbide coating and with a modifying interlayer of pyrolytic carbon. The critical lengths were measured to be 1.67 ± 0.58 mm and 7.46 ± 0.61 mm, respectively. Using a coating fracture strength of 500 MPa, extrapolated from matrix fracture results recorded during flexure testing, the interfacial shear strengths were calculated to be 3.98 ± 0.37 MPa and 0.89 ± 0.04 MPa. Figure 10.25 shows fractures as observed through a stereoscopic microscope at 70X.

10.5.2 Nicalon fibers

Tensile testing of the Nicalon fibers to determine interfacial frictional stresses was more complex and tedious than for the AVCO filaments. Segmented fracturing was observed on a limited portion of the filaments in each fiber bundle. The lengths of the fragments for

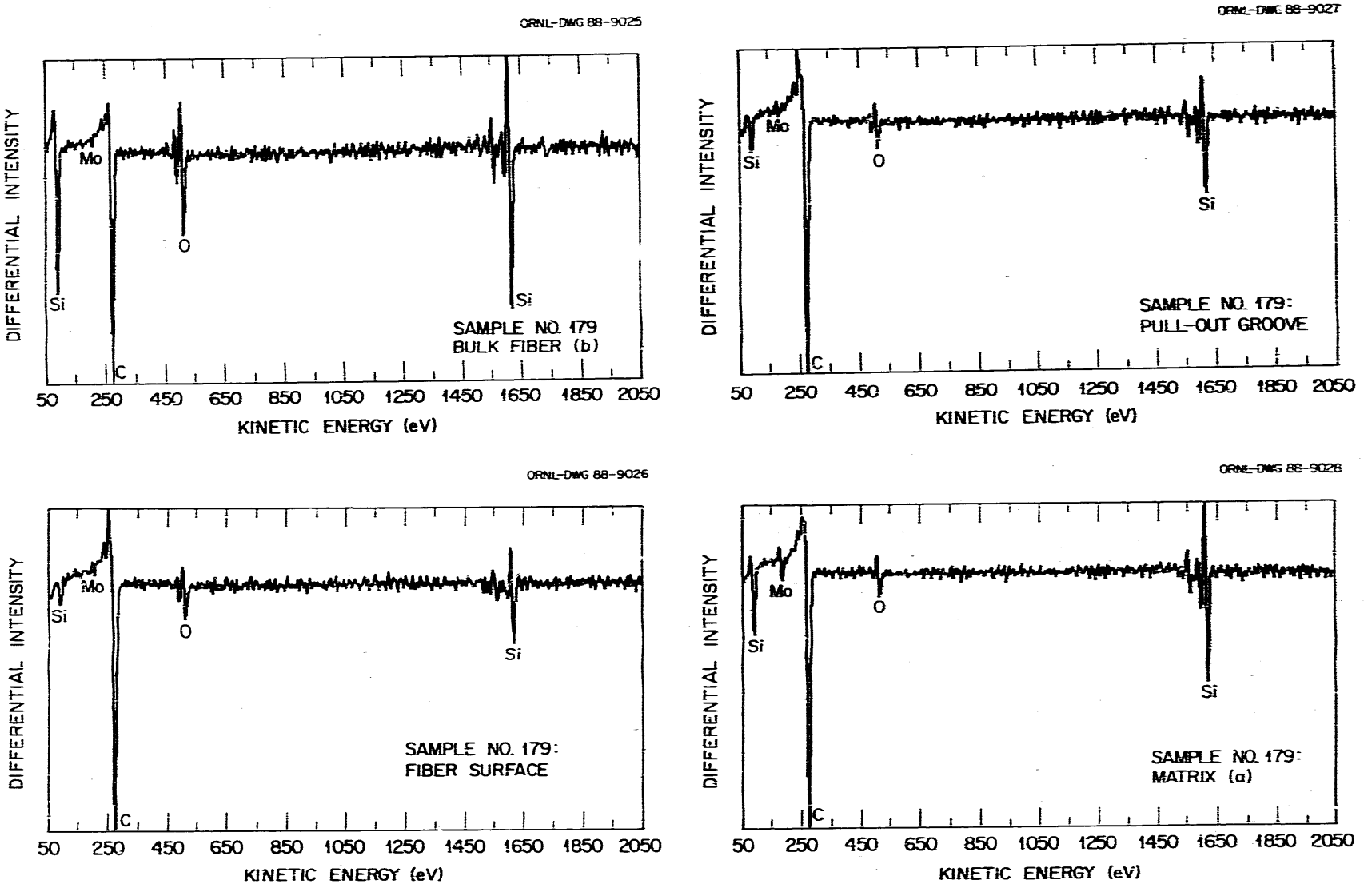

Figure 10.24. AES analysis of fracture surface features for an SiC composite specimen containing Nicalon fibers coated with a molybdenum intermediate layer.

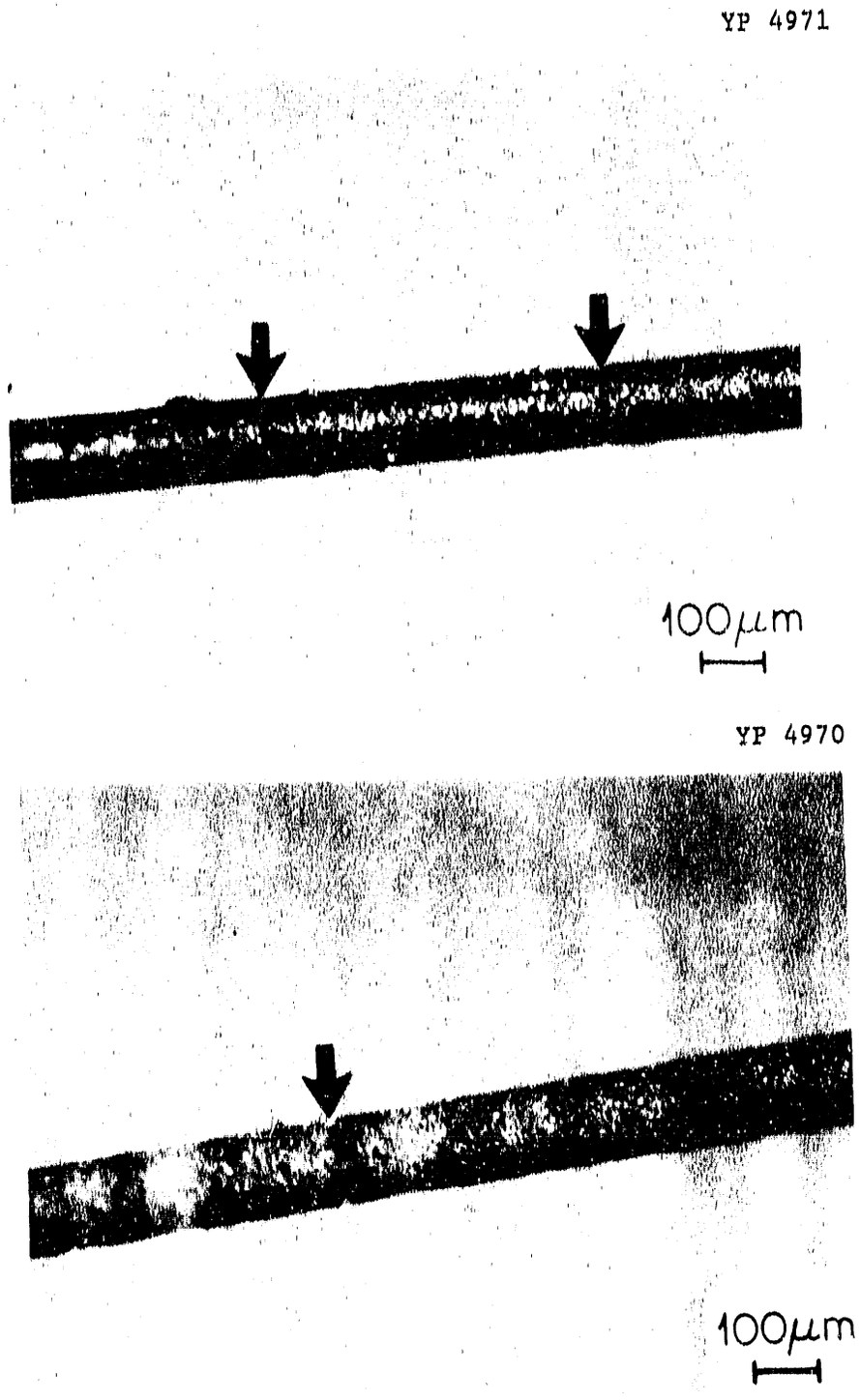

Figure 10.25. Coating fracture observed during testing of AVCO filaments: (*a*) untreated and (*b*) with a carbon intermediate coating.

uncoated tows were 14 ± 2 μm; the coatings on the carbon-coated bundles flaked off and could not be measured. The interfacial frictional stress for uncoated filaments was calculated to be 39 ± 6 MPa. A summary of tensile testing data is given in Table 10.10.

Testing of the individual filaments uncovered a new set of variables that were not evident in the testing of the larger-diameter fibers. The majority of the filaments bowed and warped during coating with SiC, independent of the positioning of the fixtures during processing. The curvature leads to bending moments upon loading and subsequent catastrophic failure of the fibers before fragmentation of the coating.

Straight fibers that could be stressed demonstrated that the coating structure and modulus play a much enhanced role in this micro-application of the tensile method. Actual straining of the coating could also be observed as the loading increased without evidence of coating segmentation. The grain size and morphology of the deposited SiC were critical factors influencing the application of the technique (Figure 10.26). These points merit further investigation to render the method reliable and reproducible for the small filaments.

Table 10.10. Determination of interfacial frictional stress from the critical lengths of fractured coatings.

Fiber type	Interlayer	Coating diameter	Segment length	Interfacial shear stress (MPa)
AVCO SCS-6	none	168±8 μm	1.67±0.58 mm	4.61±0.42
AVCO SCS-6	carbon	171±1 μm	7.46±0.61 mm	1.15±0.06
Nicalon (CG)	none	1 μm thick	14±2 μm	38.1±6.2

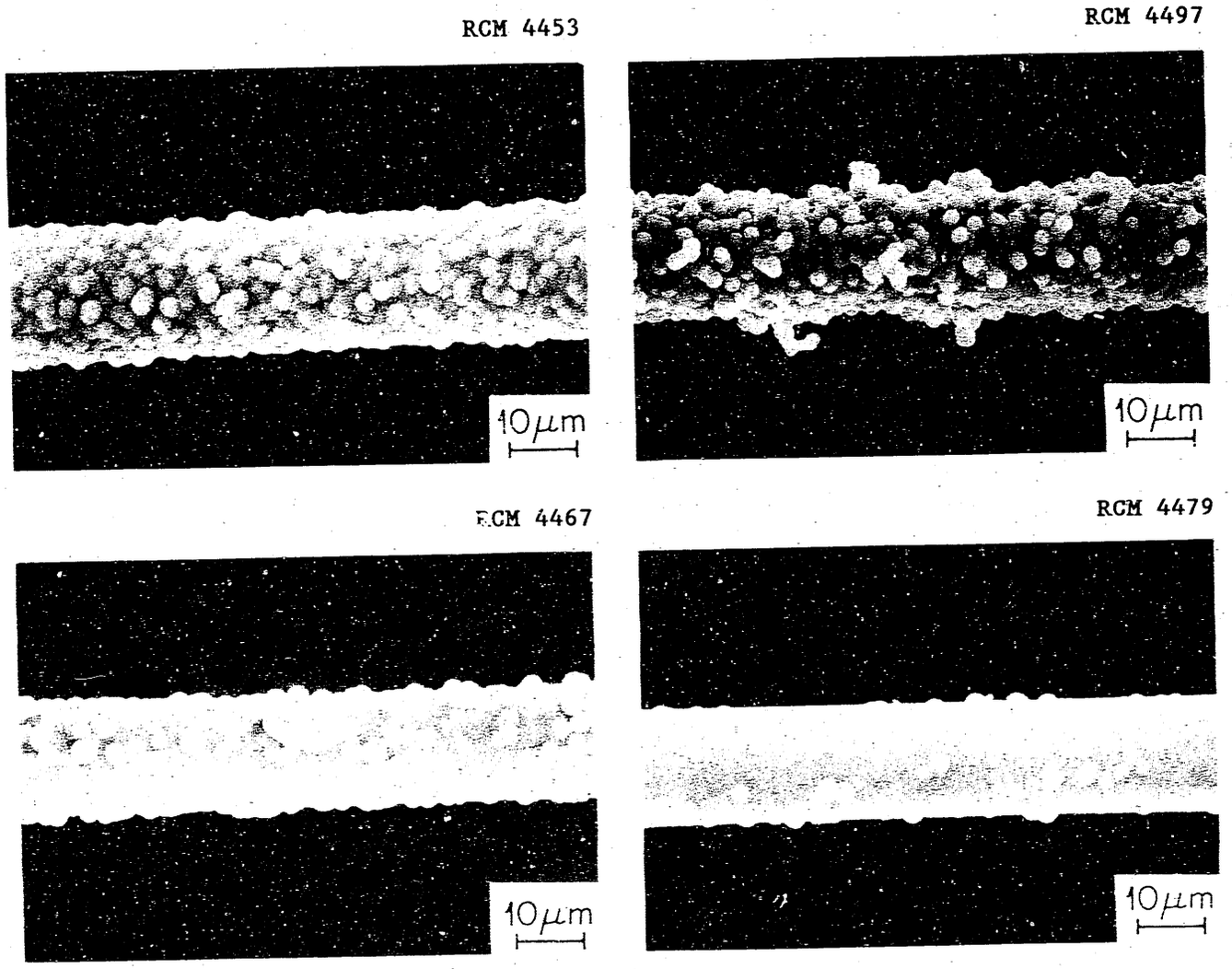

Figure 10.26. SEM photomicrographs of SiC-coated Nicalon filaments.

11. DISCUSSION

11.1 Constituent Properties

A review of the mechanical properties of the Nicalon fibers and of CVD SiC precedes the examination of the effects of modifying interlayers on interfacial stresses and the mechanical properties of composite materials fabricated from these components. A working knowledge of the properties of the constituents and the factors affecting their individual behavior is necessary to provide the basis from which further relationships can be developed. The mechanical properties of the fibers and matrix as specified by the parameters of the forced chemical vapor infiltration (FCVI) process can be incorporated into the predictive equations for composite behavior. The relationships concerning modulus and strength can provide trends that describe or help to explain observed behavior. The expressions are well developed and the properties of the components have been thoroughly evaluated. The mechanics and materials data can be combined to calculate probable composite properties and behavior.

The Nicalon fibers have been scrutinized since their introduction a decade ago. Nicalon fibers are produced from an organometallic precursor, polycarbosilane (17,18,123,124). The process begins with the dechlorination of dichlorodimethylsilane with molten sodium metal to form the solid polymer, dimethylpolysilane, which is converted by further polymerization to polycarbosilane, which is then purified and melt-spun into fibers. To prevent melting during heating and pyrolysis, the polycarbosilane fibers are heated in air or exposed to ozone to cross-link the molecular chains. The polymer fibers are then converted to SiC by a sequence of heat treatments to a final temperature of 1475 to 1675 K.

The resultant fibers are composed of approximately 55 wt % silicon, 30 wt % carbon, and 15 wt % oxygen. These elements are present as 60 wt % β-SiC, 30 wt % amorphous SiO_2, and 10 wt % amorphous free carbon, and the fibers have a measured density of 2.55 g/cm^3. The oxygen content is a consequence of the curing cycle and is partially responsible for the thermal instability of the Nicalon Si-C-O fibers.

The mechanisms of fiber degradation have been a topic of debate for a number of years (119-135). The manufacturer quotes a strength of 2500 MPa for the material; however, extensive evaluation has shown the ultimate strength of fiber tows to be about 2100 MPa (see Table 10.3). Heating the fibers in any atmosphere to temperatures above 1075 K results in a reduction in fiber strength. This is the major disadvantage of the Nicalon fibers, and this degradation of properties has been attributed to factors such as grain growth, carbothermal reduction of SiO_2 to form SiC and CO gas, composition changes, etc.

The composition and structure of the fibers have been analyzed using many analytical techniques (119-134). From the investigations, the fibers appear to be composed of ultrafine 1.7-nm grains of β-SiC bonded together by an amorphous silica matrix. Nuclear magnetic resonance has revealed the presence of bonding that is characteristic of silicon oxycarbide, suggesting that this material acts as a transition layer at the surface of the grains. Others (135) have also hypothesized that the SiC particles are surrounded by a carbon layer. Regardless, the Nicalon fibers are damaged by heating to elevated temperatures, and many factors exacerbate the problem. The strength of Nicalon fibers subjected to a variety of treatments was given in Table 10.3.

The properties of CVD SiC have been of great interest for some time (136-140). The density, strength, and modulus of the deposited material are strongly influenced by the processing temperature. Table 11.1 lists the measured properties of silicon carbide fabricated by various methods. The results show the mechanical properties of the carbide degrade as the deposition temperature decreases. This is a disadvantage in the processing of Nicalon fiber-SiC matrix composites because the properties of the composite could be improved by higher processing temperatures, but the fibers limit the deposition temperature.

11.2 Predicted Composite Behavior

Comparative analysis of the predicted and measured properties was used to determine the effects of fiber coatings on the behavior of Nicalon-SiC composites. The coatings not only influence interfacial bonding and friction but also interact with the fibers. Consequently, the ultimate strength of a brittle matrix composite is determined entirely by the ultimate strength of the reinforcing phase; therefore, degradation of the ultimate strength of the fibers results in a reduction in the final strength of the composite. The properties of the fibers and matrix to be used in the prediction of composite behavior are: an ultimate strength of 1250 MPa, a fiber modulus of 110 GPa, a matrix strength of 500 MPa, and a modulus of 295 GPa. These were chosen by comparing the experimental and literature results for strength and modulus for the two components and selecting the values that best represent the retained properties after exposure to FVCI conditions.

Table 11.1. Properties of SiC.

Processing method	Density (g/cm^3)	Strength (MPa)	Young's modulus (GPa)	Fracture surface energy (J/m^2)
Sintered	2.67	103.4	193.0	12
Sintered	2.70	122.8	197.0	27
Sintered	2.77	128.3	254.0	11
Hot pressed	2.65	167.6	209.0	24
CVD				
1475 K	2.95	482.8	295.9	
1575 K	3.04	682.1	335.9	
1675 K	3.19	857.9	420.7	
1875 K	3.19	794.8	434.5	
2075 K	3.21	827.6	426.9	

11.2.1 Matrix cracking

In the Nicalon fiber-reinforced silicon-carbide-composite system, brittle fiber exists in a brittle matrix. The fibers possess higher strength and higher strain-to-failure values than the matrix; thus, the fibers can increase the stress necessary to nucleate the first matrix crack. The degree to which the matrix failure strain will be increased is dependent on interfacial bonding and frictional stresses [Eq. (16)]. The relationship describing first-cracking stress in the matrix can be determined by rearranging Eq. (16) to give

$$\sigma_c = [24\gamma_m r_i E_f V_f^2 / E_m^2 E_c d_f V_m]^{1/3} E_c \quad . \tag{34}$$

The measured and calculated matrix fracture stresses for the composites are listed with the respective interfacial frictional stresses in Table 11.2.

Only the composites containing carbon-coated fibers exhibited adequate postcracking stress and strain to examine the effect of interfacial frictional stress on matrix cracking. Figure 11.1 shows the combined load-displacement curves for the samples having a carbon intermediate layer. The remainder of the samples failed shortly after the first sign of matrix cracking, suggesting that the fibers could not sustain the load supported by the composite after matrix fracture. Thus, other factors must be considered when attempting to relate composite properties to interfacial forces.

Table 11.2. The influence of interfacial frictional stress on matrix cracking.

Sample No.	Frictional stress (MPa)	Observed matrix fracture (MPa)	Predicted matrix fracture (MPa)
171	4.3±1.2	193±28	163
174	0.6±0.4	160±16	87
175	11.3±4.7	257±29	243

ORNL-DWG 88-10677

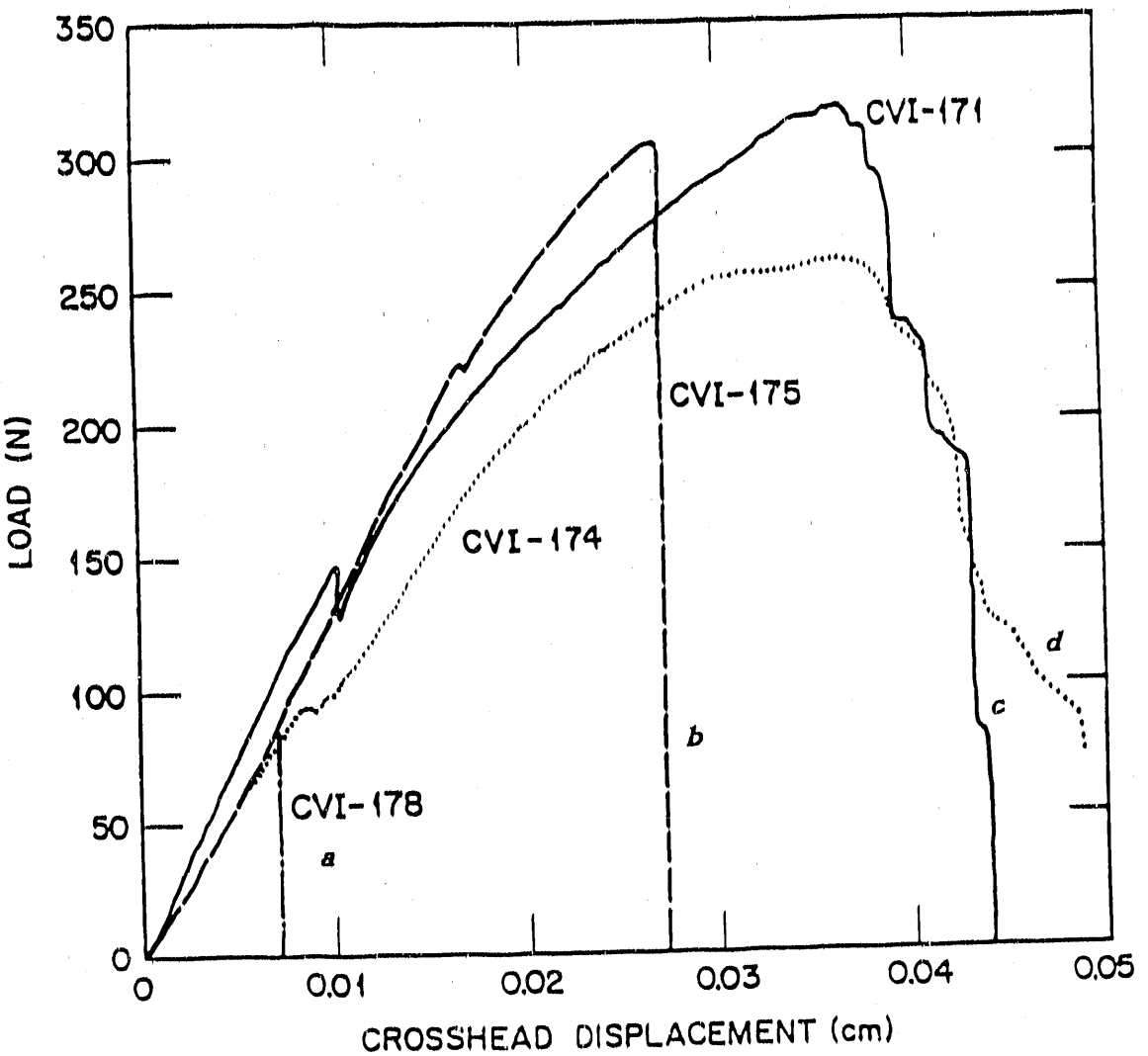

Figure 11.1. The effect of varying thickness of pyrocarbon on the fracture of SiC composite samples: (*a*) CVI-178, uncoated; (*b*) CVI-175, 0.10-μm carbon layer; (*c*) CVI-171, 0.17-μm carbon layer; and (*d*) CVI-174, 0.28-μm carbon layer.

11.2.2 Fracture stress and Young's modulus

The average measured values for density, strength, and modulus for all tested composite samples and property data calculated using the predictive equations are given in Table 11.3. "Rule of Mixtures" behavior can only accurately predict the behavior of a composite in which a perfect bond exists between the fibers and matrix. The more realistic ACK interpretation model allows for debonding and slip at the fiber-matrix interface and the strain associated with multiple-matrix fracture. The predicted single-fracture tensile behavior of a unidirectionally reinforced composite is shown in Figure 11.2 (78). The similar curve in Figure 11.3 includes a short constant-stress zone associated with the mulitiple-matrix phenomenon (82). The expressions have been successfully applied to a number of composite systems, such as fiber-reinforced glasses and cement. These systems, however, combine high-modulus, large strain-to-failure fibers with low-modulus, strain-intolerant matrices to improve the overall properties of the system.

The Nicalon-SiC system is completely different from the majority of the previously examined systems in that, although the fibers have a higher strain-to-failure ratios than the matrix, the modulus of the reinforcement is lower than that of the matrix. The composite is not being developed to create a stiffer or stronger material than monolithic SiC but to produce a tough, impact-resistant material that fails in a more-ductile manner. The goal of incorporating brittle fibers into a brittle matrix is to prevent catastrophic failure through fiber pull-out and crack-bridging after matrix fracture.

Table 11.3. Property comparison in the Nicalon-SiC system.

Sample No.	Fiber content (wt %)	density (g/cm^3)	Theoretical density (%)	Flexure strength (MPa)	Flexure modulus (GPa)
Measured Values					
170	41.8	2.35±0.03	80.9±1.0	88.0±8.0	120.7±17.9
171	42.1	2.32±0.04	79.8±1.4	388.8±14.6	137.2±20.7
172	41.3	2.35±0.03	80.7±1.0	107.7±13.2	119.3±26.2
173	39.0	2.31±0.02	79.3±0.7	80.0±10.3	129.0±21.4
174	41.8	2.42±0.03	83.1±1.0	389.7±13.4	163.4±15.9
175	43.5	2.25±0.04	77.5±0.5	261.8±40.6	147.6±9.0
176	42.0	2.44±0.03	84.1±1.0	91.2±4.1	122.1±2.8
177	40.4	2.30±0.06	79.1±2.0	113.9±19.5	150.3±22.8
178	40.3	2.34±0.06	80.4±0.9	81.9±10.1	160.0±21.4
179	41.3	2.17±0.04	74.4±1.2	57.2±11.5	140.7±33.1
180 (unoxidized)	42.9	2.40±0.14	82.4±4.7	380.2±33.4	103.4±13.1
180 (oxidized)	42.9	2.37±0.15	81.6±5.3	188.5±17.0	114.5±3.4
Predicted Values					
Fully dense	40	2.95	100	500	220
80% dense	40	2.31	80	500	160
No fiber contribution	40	2.31	80	200	160
No fiber contribution (20% porosity)	40	2.31	80	90	110
Fibers as pores (60% porosity)	40	2.31	80	75	55

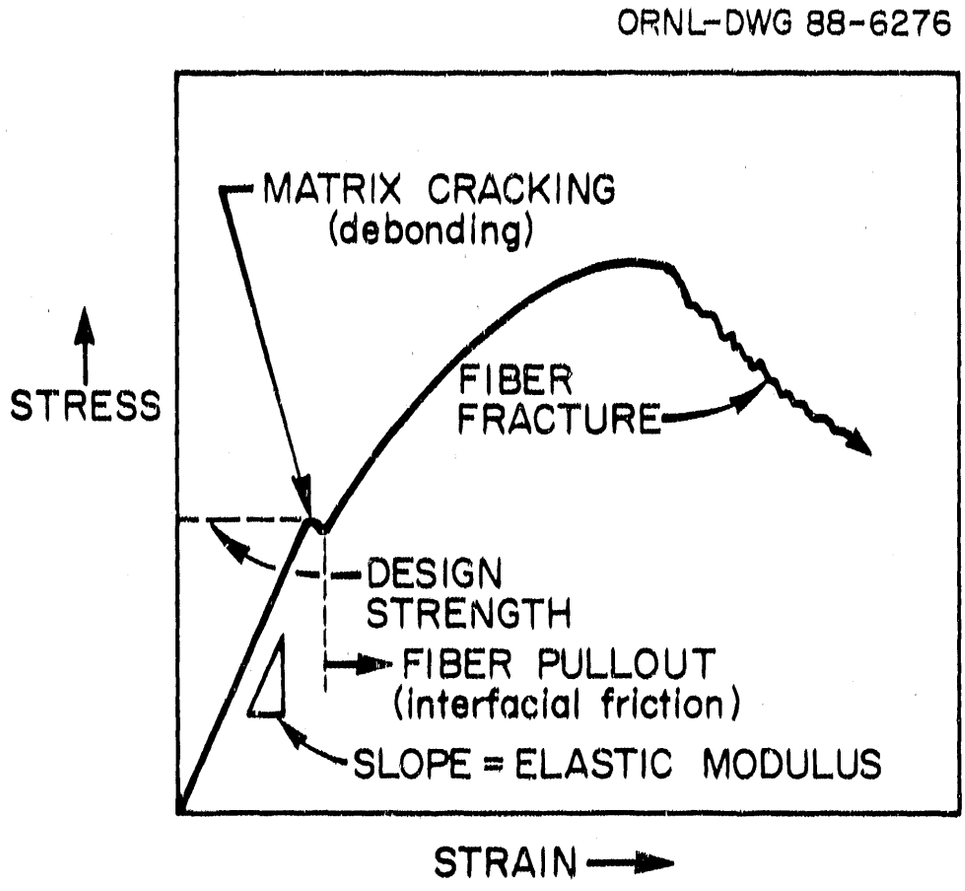

Figure 11.2. An ideal stress-strain curve for a fiber-reinforced composite exhibiting single-fracture behavior.

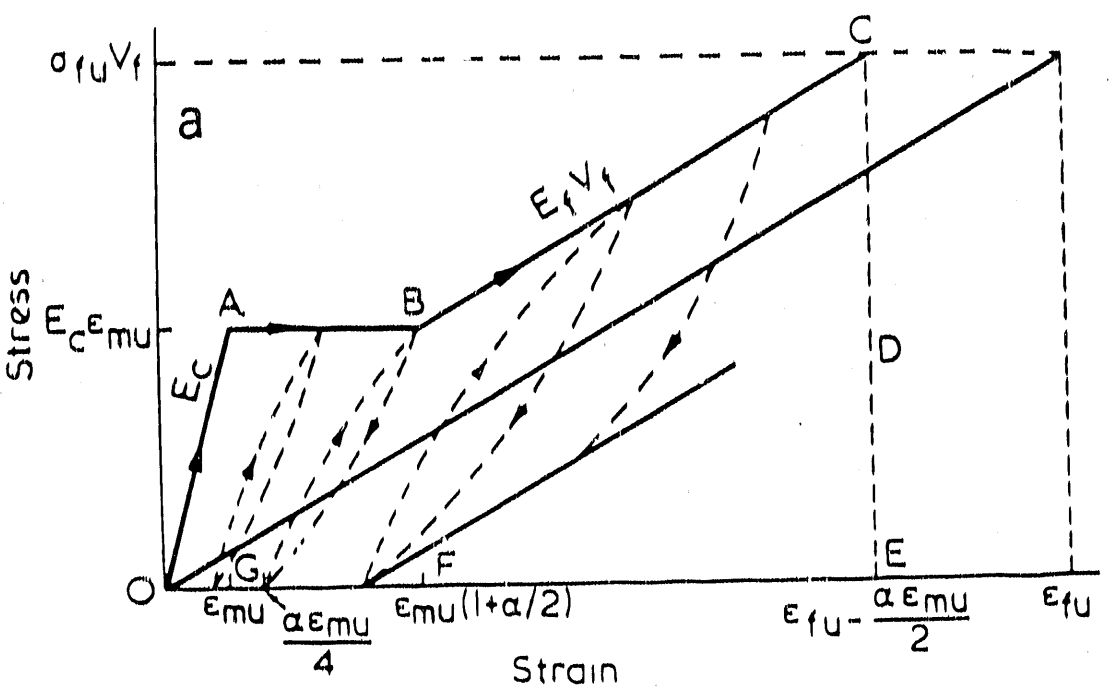

Figure 11.3. The theoretical stress-strain curve for a composite exhibiting multiple matrix fracture. *Source*: J. Aveston, G. A. Cooper, and A. Kelly, "Single Multiple Fracture: The Properties of Fiber Composites," pp. 15-26 in *National Physics Lab Conference Proceedings*, November 1971.

As previously discussed, the ultimate strength of the composite is determined by the volume fraction and the failure strength of the fibers. Thus, the maximum strength of a composite unidirectionally reinforced with 40 vol % heat-treated Nicalon fibers is 500 MPa. (This can vary depending on the retained strength of the fibers.) Figure 11.4 contains the approximated stress-strain curves for the individual constituents in the Nicalon-SiC system and a typical flexure curve for a composite fabricated from carbon-coated fibers. Comparing Figures 11.2, 11.3, and 11.4, it becomes obvious that the expressions do not accurately predict composite behavior; however, the calculations can be used to determine the contribution of the individual components and their influence on the mechanical behavior of the composite.

The discrepancies result from number of factors. It is assumed that the fibers are unidirectionally aligned and are continuous filaments of infinite length. It is obvious that the Nicalon-SiC composites do not constitute an ideal system, but the composites contain misaligned fibers of varying length. The effective length of the fibers is dependent on the angle of each cloth ply, the structure of the cloth weave, and the distibution of critical flaws in the fibers themselves. For example, plain-weave cloth was used in the fabrication of the samples. The cloth contains 6 tows/cm in the weft and warp directions, and the tows are approximately 1 mm wide; therefore, each yarn bends around another yarn every 1.67 mm. This bending at the fiber intersections could affect the apparent embedded length of the fiber and influence composite ultimate properties.

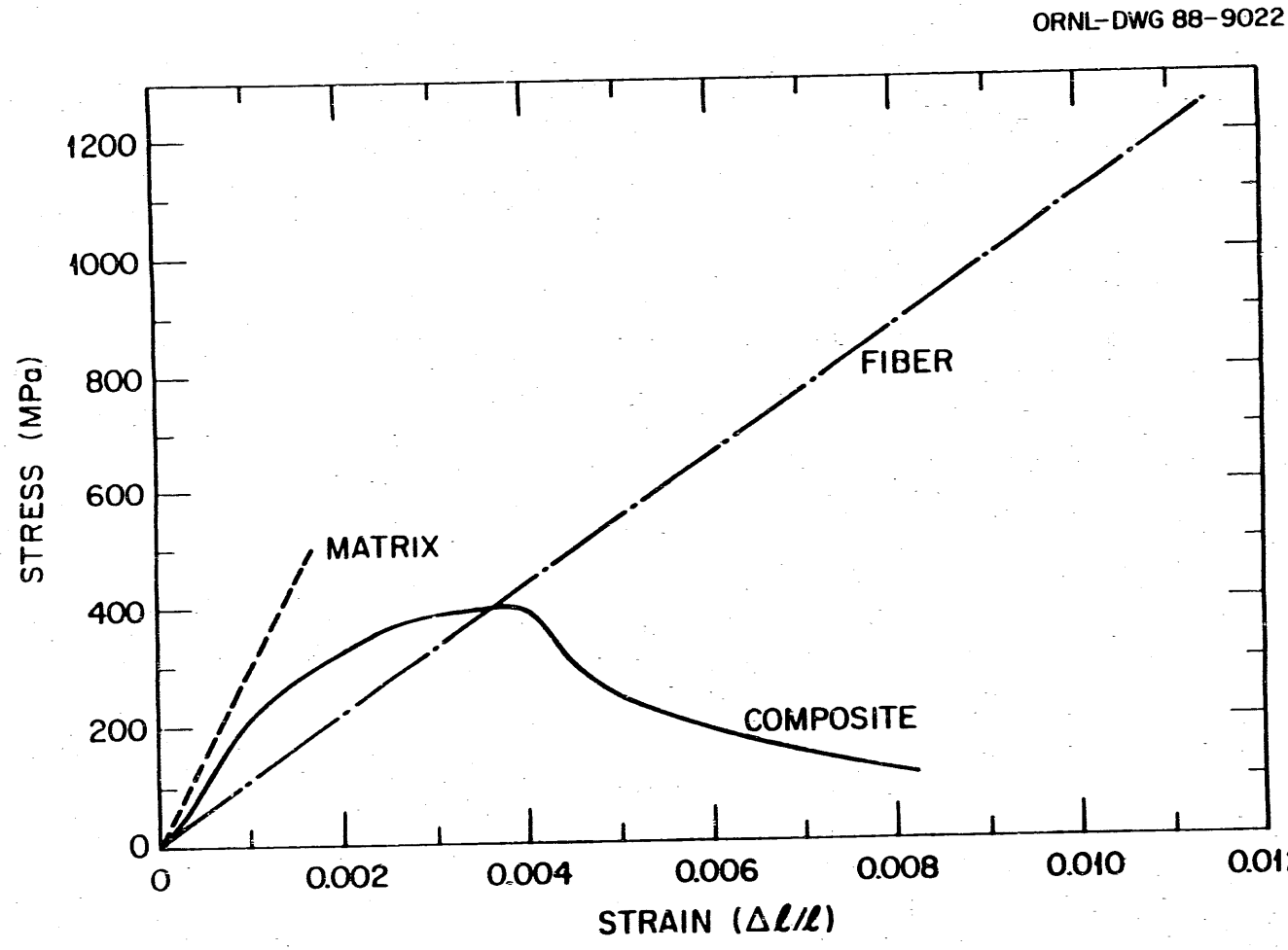

Figure 11.4. The apparent mechanical behavior of the fibers and matrix compared with an actual flexure curve for a 40 vol % Nicalon fiber-SiC composite.

Fiber length becomes important after matrix failure. When a brittle matrix fractures, the fiber and matrix debond and the ultimate fracture strength of the composite will then depend on the forces to overcome the friction between the fibers and matrix during fiber pull-out and to fracture the reinforcing fibers. Once debonding has occurred, the frictional resistance to the fiber pulling out of the matrix is determined by the normal compressive forces exerted on the fiber by the matrix (141-143). A semiempirical expression for the tensile stress on a fiber during pull-out in a glass or carbon-fiber-reinforced cement is given as

$$\sigma_f = (T_i/k)[1-\exp(-4k\ell_e/d_f)] \quad , \tag{35}$$

where ℓ_e is the embedded length of the fiber, T_i is the interfacial shear stress, d_f is the fiber diameter, and k is a fitting constant. As shown earlier, there is a minimum length over which efficient load transfer can occur. The argument can be extended to determine the influence of interfacial frictional stress on the ultimate strength of a composite by assuming that the interfacial frictional stress decreases linearly with stress on the fiber (see Figure 7.4). The postcracking strength of a fiber-reinforced composite is then

$$\sigma_c = (V_f\tau_i/k)[1 + (d_f/2\ell k)\exp(-2\ell k/d_f) - (d_f/2\ell k)] \quad , \tag{36}$$

where V_f is the volume fraction of fiber and the variables are as in the previous equation and

$$k = E_m\nu_f\mu/E_f(1 + \nu_m) \quad , \tag{37}$$

where E is the modulus, ν is the Poisson's ratio, and μ is the coefficient of friction between the fiber and matrix.

The equations demonstrate that the interfacial forces and fiber length continue to influence the behavior of a composite even after matrix failure. A high coefficient of friction and high interfacial shear stress will allow efficient load transfer from the matrix to the fibers and also hinder pull-out of the fibers. This will result in an increase in the strength of the composite.

It had been speculated that entanglements in the fiber bundles would allow the yarns to perform like "rope" (63,64) and provide sufficient reinforcement to carry the load at the onset of matrix fracture; therefore, there was little concern with regard to excessive slipping of the fibers. Closer examination of the Nicalon tows reveals that they will not act like ropes or braids because the filaments are not twisted or intertwined within the tows. This fact and the described relationships show that an extremely weak bond or excessive slip will reduce the ultimate strength of the composite. This is demonstrated in the samples in which the carbon interlayer was burned out. The specimens were weakened, and matrix fracture occurred at extremely low-stress levels.

Of course, the interfacial bond does not singly determine the final behavior of a composite material. Equations (8) and (9) are used to demonstrate the effects of porosity on the mechanical properties of a material. The FCVI composites had densities of approximately 80% theoretical; therefore, predicted values for strength and modulus were corrected for porosity in these expressions. The effects of fiber property degradation were examined by calculating the properties of a composite in which the fibers had no contribution to the strength of the composite or, simply, could not withstand the load transferred to them

upon matrix failure. This is the condition under which catastrophic failure occurs. These values were then corrected for porosity. In the extreme case, it was assumed that the fibers were completely separated from the matrix and, therefore, did not contribute to the composite properties and that the fiber cavities acted as voids. The behavior is analogous to the behavior of CVD SiC containing 60 vol % porosity.

The data in Table 11.3 and the fracture surface photographs in Section 10 show that only the composites fabricated from carbon-coated preforms possessed high strengths and exhibited some degree of fiber pull-out. The measured strengths for the majority of these samples approached the predicted strength of 500 MPa, and the difference in the values results from fibers that were not aligned because of the rotating orientation of the cloth layers. The highest strengths were recorded for the sample with the intermediate interfacial frictional stress.

Carbon has proven to be a useful interfacial layer since the earliest ceramic composite experiments. Carbon coatings were applied to fibers to prevent attack of the fibers by silicon during liquid-metal infiltration in the fabrication of carbon-fiber-reinforced silicon composites. Many of the other CVI processes require the preforms to be rigidized prior to infiltration. This is accomplished by impregnating the fibrous structure with resin, which is pyrolyzed to form carbon.

Carbon is relatively stable with respect to the fibers and the matrix. The carbon reacts with the silica layer at the fiber surface to form SiC and probably does not diffuse into the fibers. The carbon appears to bond to the fibers and not to the matrix. The thermochemical

calculations of the matrix deposition onto the carbon layer reveals the increased presence of carbon at the interface, thus supporting the observation.

The remainder of the samples exhibited brittle fracture with little evidence of fiber pull-out or strength after matrix failure. The interfacial coatings reacted chemically with the fibers and/or matrix to either degrade fiber strength, enhance fiber-matrix bonding, or both. The samples having high interfacial frictional stress had the lowest strengths, and fracture surfaces were flat and smooth. Although the other samples had lower measured interfacial stresses, the strengths of these specimens were relatively low and little fiber pull-out was observed. The strengths of the specimens were within a few percent of the predicted strength of an 80% dense composite reinforced with extremely weak fibers ($\sigma_f = 0$).

One must conclude that the interfacial coatings reacted with the fibers and decreased their strength. The various elements of the coatings must diffuse into the fibers and disrupt composition and structure within the bulk of the material. The fibers consist of β-SiC crystallites, amorphous SiO_2, and free carbon. The diffusing elements could react with these compounds to form new compounds or to increase (or decrease) the concentration of these compounds. The diffusion rates of relevant elements in silica and silicon carbide are given in Figure 11.5 (144-149). These kinetic factors can be combined with thermochemical calculations to determine the possible chemical reactions within the Nicalon fibers.

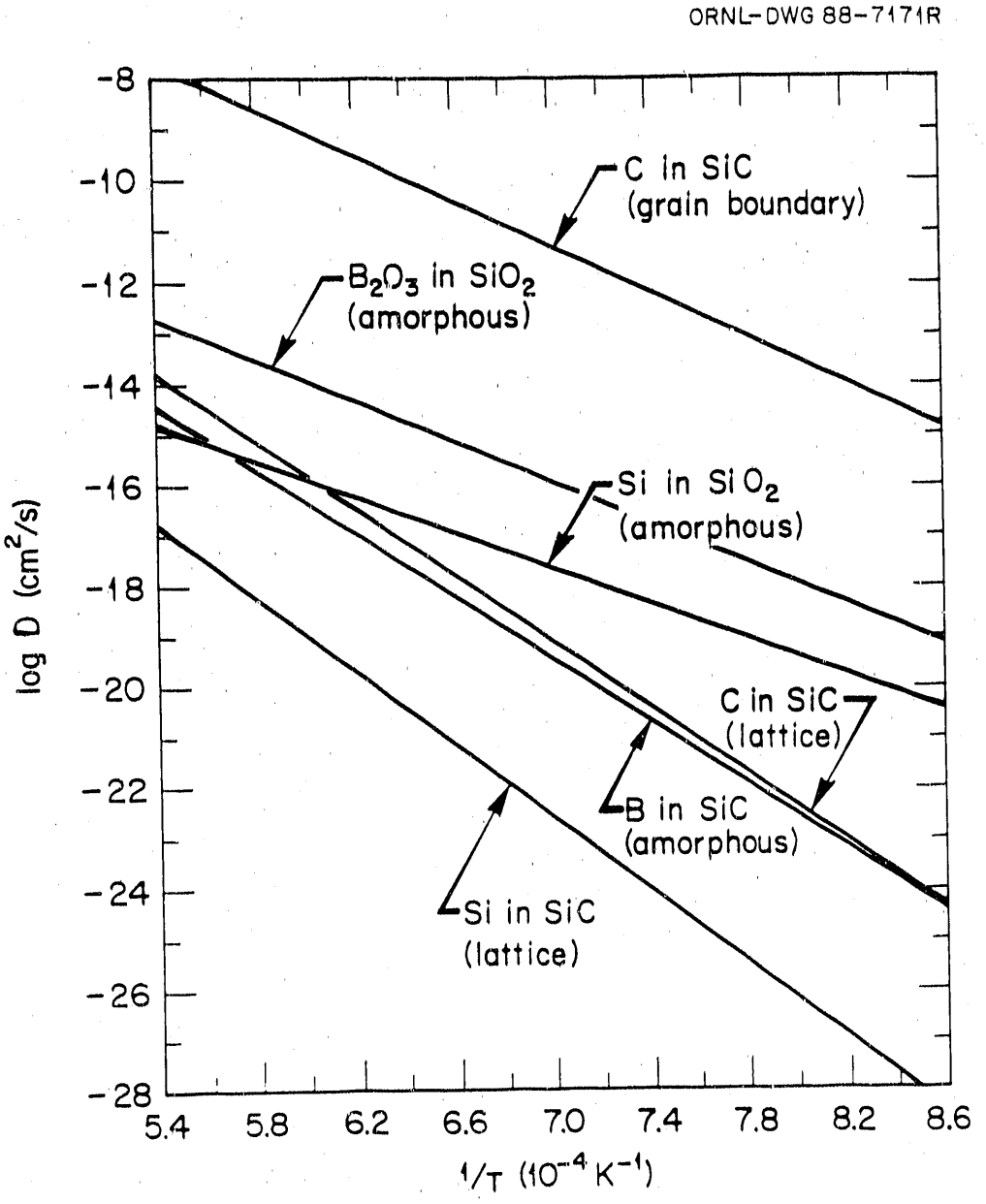

Figure 11.5. The diffusion coefficient for selected elements in relative materials.

In four of the samples, the fibers were exposed to a silicon-rich environment. These samples exhibited the highest bonds, and fiber tows coated using similar conditions failed before they could be tested. Silicon can diffuse relatively quickly through the silica and react with free carbon to form SiC. If carbon is present as a thin coating around the SiC crystallite, the reaction will accelerate grain growth in the fibers. The Nicalon fibers depend on their amorphous nature for strength, and it has been shown that crystallization and grain growth lead to reductions in fiber strength.

The grain growth will also lead to a reduction of grain-boundary volume, forcing the silica to move outward toward the surface of the fibers. This is useful in explaining the high oxygen content at the fiber-matrix boundary in these samples. The silica layer would strongly bond the fibers to the matrix.

These observations contradict the results of the analysis of composites composed of Nicalon fibers in glass or glass-ceramic matrices. Researchers have shown that a carbon layer forms at the surface of the fibers when they are hot pressed into an aluminosilicate-based matrix (106-108,150,151). The carbon layer allows for fiber debonding and slip, and the samples exhibit high strength and toughness. Samples without the carbon-rich surface fail in a brittle manner. It has been hypothesized that the carbon diffuses to the surface as CO gas, which reacts with the glass, which is most likely in a reduced state, to produce carbon. An exact explanation for the formation of this layer is unknown.

The observed phenomena in the CVI composites may be useful in explaining the events that proceed in the glass-matrix composites. The

as-received fibers have a slightly oxygen-rich surface layer. After processing, a carbon layer is found at the fiber-matrix boundary. The composition of the fibers changes; the amount of SiC increases and the SiO_2 concentration decreases correspondingly. Traces of aluminum are also found in the fibers embedded in the aluminosilicate glass matrices. It appears that aluminum diffuses into the silica to form mullite, and silica diffuses into the aluminosilicate matrix. The mullite reaction, combined with grain growth, will degrade the fiber properties. As the grain-boundary volume decreases, the silica and the free carbon are forced to the surface of the fiber. The silica can diffuse into the matrix; the carbon, on the other hand, remains at the fiber-matrix interface because it has nothing with which to react.

The mention of the mullite formation in the fiber leads to a discussion of the boron-containing interlayers. Boron can react with the silica in the fiber to form boria (B_2O_3). Boria diffuses rather rapidly through silica and could possibly react with the free carbon or SiC to form boron carbide (B_4C). Even if these reactions do not occur, boron additions reduce the strength of a glass. Table 11.4 lists the strengths of various glasses and shows that trace amounts of boria result in large decreases in strength (7,152,153). The boron appears to react to form B_4C during the matrix deposition process, as seen in the higher-magnification photos in Figure 10.19.

Molybdenum proved to be chemically reactive with every element and compound in the system, which demonstrates the need for a chemically inert interfacial coating. The molybdenum layer not only disturbed the composition of the fibers but was found in regions of the matrix

Table 11.4. Properties of glasses and glass fibers with varying compositions containing boron.

Glass/composition	Strength (MPa)	Modulus (GPa)
Bulk material		
Vitreous Silica	110	73
Vycor (4% B_2O_3)	70	46
Pyrex (13% B_2O_3)	70	70
Borosilicate (20% B_2O_3)	70	55
Fiber[a]		
D-glass (22% B_2O_3)	2400	52
E-glass (8-13% B_2O_3)	3500	70-75
S-glass (0% B_2O_3)	4600	84-88
SiO_2	5860	70

[a]Aluminosilicate compositions.

throughout the composite sample. The metal apparently reacted to form volatile species and hindered the matrix-deposition process, resulting in poor densification. It is obvious that the interlayer must be relatively inactive with respect to the composite components and fabrication procedures.

11.3 Interfacial Frictional Stress Measurement

11.3.1 Indentation

The indentation method for determining interfacial frictional stress is relatively simple and is easily implemented. The test provides a quantitative value for the degree of bonding and friction at the interface of a completed composite sample. The method is applied to finished specimens; thus, no speculation is necessary to account for unseen effects. The procedure also employs a standard hardness instrument to apply loads to the fibers and an indentor, which is a common item in most materials laboratories.

The technique has a few disadvantages. The results are a measure of the load necessary to break the fiber-matrix bond combined with the load required to overcome the frictional stresses and push the fiber a small distance. There are two distinct stresses at work at the interface, bonding and friction (154). Both phenomena contribute to the mechanical behavior of a composite; thus, both must be characterized to relate composite properties to interfaces. A number of in situ techniques that measure both bonding and friction are currently being developed. These methods will benefit from the recent advances in indentor instruments, such as instruments that simultaneously record load and displacement (155-157). These range from standard dash-pot indentors equipped with load cells and displacement gages to the Nanoindentors (157) that utilize

rare-earth magnets and coils to apply the loads and capacitance displacement devices to record travel. The instruments have been used to distinguish between debonding and friction and have shown that Poisson's expansion may pose more of a problem in these tests than anticipated (158).

The Marshall analysis (88) assumes linear distribution of forces along the displaced length of fiber. This has been an area of controversy and has resulted in the development of alternative numerical techniques for characterizing displacement, stress fields, and friction at the fiber-matrix interface. Finite-element analyses have shown that the frictional stresses increase locally because of the Poisson's expansion of the fiber during compression (159) (Figure 11.6). The evaluations of the method have demonstrated that nonlinearities and gradients are present in the system and that the indentation method only measures an average of the actual stresses. However, the average values computed from the finite- element analysis agreed with earlier-reported values.

Recently, a shear-lag analysis for estimating interfacial frictional stress in ceramic-matrix composites has been presented (160). The analysis includes an approximate correction for the increase in interfacial forces caused by the transverse Poisson expansion of the fibers subjected to a compressive load. An exponential decrease of the interfacial shear stress along the fiber is predicted and can provide a basis for the determination of the various stresses acting on the fiber-matrix interface.

The shape of the indentor tip and its effect on the distribution of forces has been discussed. A pyramid diamond may not apply a uniform load to the fiber end, thereby complicating the numerical analysis of the

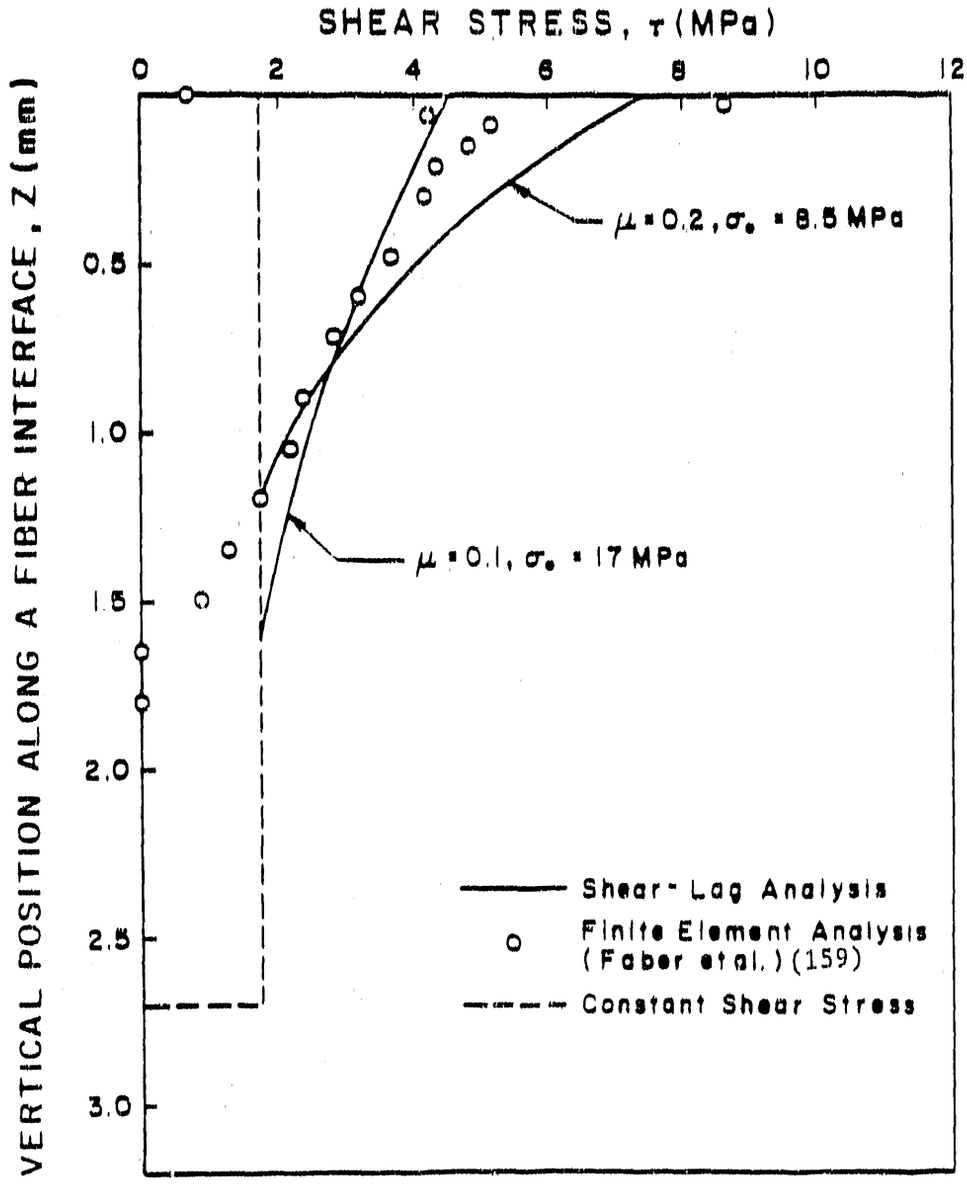

Figure 11.6. The nonlinear distribution of shear stresses at the fiber-matrix interface. *Source*: D. K. Shetty, "Shear-Lag Analysis of Fiber Push-Out (Indentation) Tests for Estimating Interfacial Frictional Stress in Ceramic Matrix Composites," *J. Am. Ceram. Soc.* 71(2), C107-9 (1988).

stress fields along the fiber interface (85,86). To alleviate the questions and problems associated with the aforementioned factor and also with the general aspects of elastic recovery in the impressions, alternative indentor geometries have been investigated. Some work has been completed using a rounded-tip diamond indentor and a flat tungsten rod to apply loads to fibers. In the first case, standard Vicker's indentors are carefully rounded using a flat diamond-impregnated grinding wheel. This method has been successfully applied to carbon and glass-fiber-reinforced plastics. The second method utilizes a fine tungsten point flattened to produce a 50-μm-diam face (161). The indentor has been used to apply loads to the relatively large 140-μm diam AVCO CVD SiC filaments embedded in a glass matrix. The major disadvantage in this case is that the surface of the indentor and fiber must be perfectly parallel during push-out. The test is in its earliest stages of development; thus, results are inconclusive.

Questions arise concerning the preparation of test specimens. Cutting, grinding, and polishing probably disturb the interface. The tested fiber must also be perpendicular to the surface, which poses a number of potential problems in multidimensional reinforced systems. The load must also be placed as close to the center of the fiber as possible. Off-center loading complicates the distribution of forces, leading to erroneous results.

The low values of frictional stress for the composite samples containing carbon-coated fibers agrees well with the measured shear of 2 MPa for the Nicalon reinforced LAS glass-ceramic composites (88). The specimens having the lowest frictional forces exhibited gradual

failure and extensive fiber pull-out. The same behavior was noted in the LAS composites.

The force required to displace the fiber within the matrix is derived from the dimensions of the impression on the fiber end and the hardness of the fiber. The results are, therefore, strongly dependent on the measured hardness of the fibers. The hardness of 22.0 ± 0.7 GPa was calculated from indent impressions made at 1-N loads on longitudinally oriented fibers. Ten indents were made on fibers in each sample. This value is high compared with a reported value of 13 GPa (88) for Nicalon in a glass matrix. Crystallization of Nicalon, which occurs upon heating above 1475 K, would explain the increase in the hardness values (130-132).

The limitations of the indentation methods become apparent when high shear strengths are measured. The application of large compressive loads on the fiber ends as delivered by the indentor split or crushed the fiber. Matrix cracking and fracture at the edges of the fiber cavities made accurate measurement of impression dimensions difficult. This is reflected in the large errors in the interfacial frictional stresses. Others applying this type of test to the well-bonded, glass-epoxy and carbon-epoxy systems have avoided fiber damage by utilizing the rounded-tip diamond indentor. Interfacial debonding stresses in excess of 88 MPa have been measured with no mention of splitting or crushing. The pyramidal Vickers diamond may accentuate the damage because of its shape. Unfortunately, the rounded tip does not leave an indent that can be measured easily after loading. Using a ground diamond or a flattened point requires the instrument be equipped to measure load and displacement, thus complicating the necessary instrumentation.

11.3.2 Tensile testing

The usefulness of the tensile test described in this report as a semiquantitative method for determining interfacial frictional stresses was demonstrated using a SiC coating on the relatively large-diameter AVCO SiC filaments. Interfacial frictional stresses were calculated from measured critical lengths for systems with and without a modifying interlayer. The low magnitude of the values is supported by the delamination of the composites and debonding of the individual filaments from the matrix observed during four-point flexure testing of composites formed from these fibers.

The tensile test is dependent on a reproducible coating with a known rupture stress. In this analysis, the strength of the coating was found in the literature and extrapolated from mechanical-property test results. A coating-rupture strength of 500 MPa was obtained and agrees well with the values calculated from measured loads corresponding to matrix fracture during flexure testing of numerous composite specimens.

The tensile method offers a number of advantages compared with the indentation test. Sample preparation is simplified and problems of fiber positioning are removed. Stress fields from neighboring fibers could influence the results of indentation measurements. This is not an issue in the tensile test. The greatest advantage of the tensile test is speed; however, the test is not problem-free.

The sequential fragmentation of coatings on the large-diameter filaments was easily observable. Specimen preparation was relatively uncomplicated. The critical lengths of the segments were relatively long and measure frictional stresses correlated well with observed behavior.

Conversely, the individual Nicalon filaments were impossible to test. The number of dependent variables increased greatly with decreasing size of the filaments. The most obvious of these were warping of the filaments during the coating process and the influence of coating microstructure. The majority of the Nicalon filaments warped during coating. The problem is a combination of the thermal expansion mismatch between the fiber and mounting fixture and the unforgiving forces of gravity. Tensile loading of bent coated fibers resulted in premature and catastrophic failure of the specimens.

The morphology and structure of the coatings greatly influenced the testing of the small-diameter filaments. The grain size of the coating and perturbations at the coating surface affected the coating fracture. The average grain size of CVD SiC deposited on Nicalon fibers at the given experimental conditions is approximately 1 μm. Nucleation is rapid and uniform at the untreated fiber surface; however, nucleation of SiC on the surface of the carbon intermediate layer is somehow hindered. This results in a coating having poorly distributed, large SiC grains.

Linear expressions for shear stress were used in the analysis of a coated fiber placed in tension. As with the indentation method, more-realistic shear-lag theories have been applied to the fiber-sheath model (162-164). These analyses account for shear stress buildup near the ends of the fibers and the nonlinear decreases in stress away from the fracture (Figure 11.5). The shear-lag theories, however, may not be accurate at higher stress levels (72). Many of the computations rely on elastic behavior in the components, and as discussed, ceramic materials exhibit very limited elastic response. Factors such as Poisson's

contraction have been ignored, and more effort is needed to thoroughly examine the value of the tensile test and its results.

11.4 Flexure Testing of Composite Materials

The usefulness of applying a flexure test to a composite has been a topic of debate in recent years. Samples of unidirectional Nicalon-glass ceramic, tested using a bending technique, were shown to fail in compression and shear but never in tension (87,165). This demonstrates that calculation of tensile strength from this loading configuration is clearly invalid. The computation of tensile strength is based on the propagation of a single coplanar crack that initiates at the tensile surface and ends at the compressive face of the specimen. At this point, the specimen fails.

The flexure strength of a beam of fiber-composite material can be up to three times that which would be predicted by linear elastic analysis for the ultimate tensile strength of the same material (141-143). The main reason for this discrepancy is the quasi-plastic stress-strain behavior of a composite material after matrix cracking. Postcracking behavior is dominated by fiber pull-out, and conventional beam theory is not applicable.

The stress block used to calculate flexural strength for an elastic material is inaccurate for fiber composites. A more realistic stress block for describing composite behavior in bending has been developed for cement and concrete composites. After matrix fracture, the neutral axis is shifted toward the compressive surface (166,167). A conservative estimate places the axis one-fourth the specimen thickness from the compressive surface (Figure 11.7). This changes the bending moment of

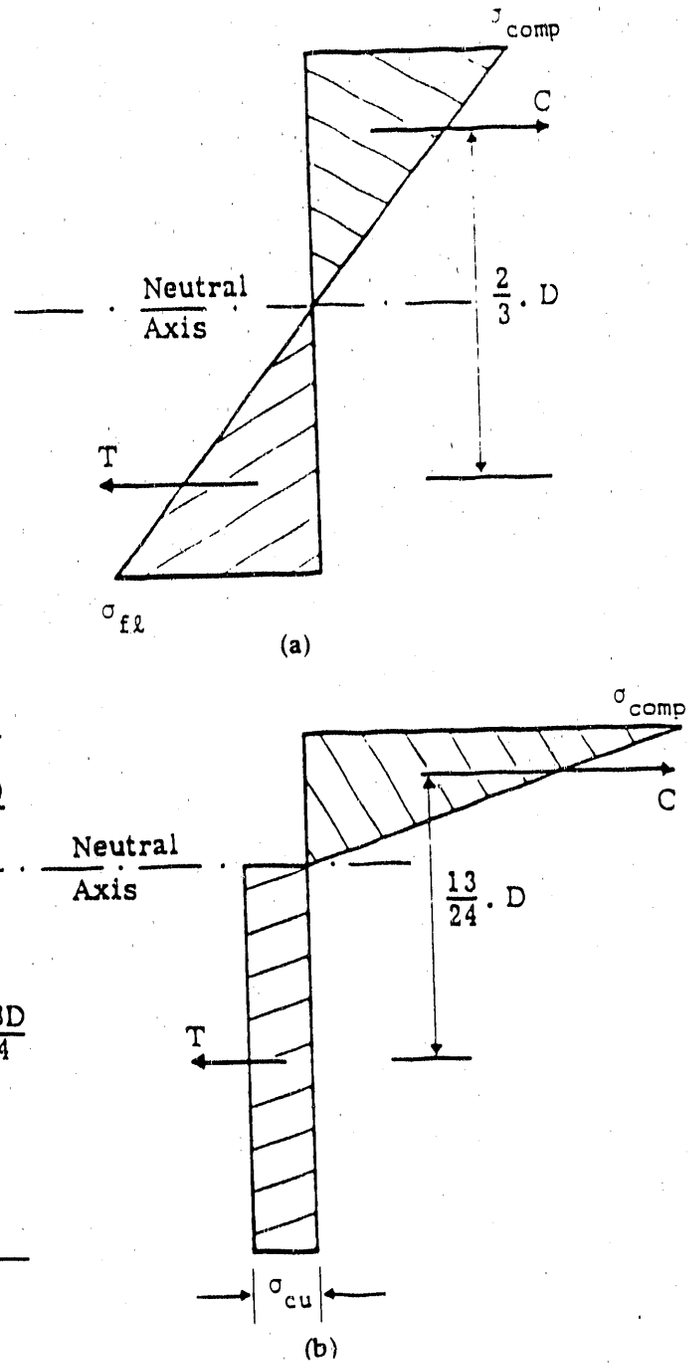

Figure 11.7. Stress blocks in flexure; (*a*) perfectly elastic material and (*b*) material that is elastic in compression and plastic in tension (166). *Source*: D. J. Hannant, "Fibre Reinforced Cements," PP. 429-500 in *Handbook of Composites, Volume 4 - Fabrication of Composites*, edited by A. Kelly and S. T. Mileiko, Elsevier Science Publishers B. V., North-Holland, The Netherlands, 1983.

the system, and when the result is compared with the expression from elastic-beam theory, the measured flexure strength of a composite is shown to be three times greater than its ultimate tensile strength. In practice, this condition is rarely achieved because compressive failure is initiated at the outer beam surface first. Although the ultimate tensile strength of a composite may not be accurately computed from flexure results, the test is useful in observing behavior of a composite before matrix cracking occurs.

12. CONCLUSIONS AND FUTURE WORK

Fabrication of a high-quality fiber-reinforced ceramic composite is a challenging task. Numerous factors must be considered in the selection of materials and the choice of processing techniques. The components must meet a list of requirements to produce the desired mechanical and physical properties when the individual phases are combined to form a composite material.

The reinforcement and matrix must be thermomechanically and thermochemically compatible. Thermomechanical interactions caused by thermal expansion differences can be a major obstacle in the development of a high-temperature composite. Thermochemical interactions will increase interfacial bonding and can destroy the properties of the reinforcement.

The strength of the fiber-matrix bond in fiber-reinforced ceramic composites controls the mechanical behavior of these materials. Interfacial bonding and frictional forces greatly influence matrix cracking and fiber pull-out. Qualitative and quantitative analyses of the interfacial shear strength is essential to develop composites that have the necessary combinations of strength and toughness for most applications. The tests described are relatively simple and can be applied to almost any fiber-interlayer-matrix system. They employ relatively uncomplicated instruments and analyses and are easily implemented.

Coatings can be employed to protect the fibers from environmental degradation and to modify interfacial bonding. The coatings must be inert to the fibers because chemical interaction increases bonding and

reduces fiber strength. The strongest composites having the largest displacement to failure resulted from the thicker carbon precoats. The fibers were well protected from chemical attack, the coatings did not react chemically with the fibers, and the materials provided adequate bonding and slip, thereby preventing brittle failure.

Continuing development will be aimed at observation of the smaller filaments in an SEM while applying the load. The method is versatile and rather uncomplicated; it can be applied to a large number of fiber-interlayer-matrix systems more easily than other techniques. A more-complete analysis of the mechanics of the system is also necessary to account for factors such as Poisson's contraction and nonlinear distribution of forces along the interface.

An instrumented indentation system is in the development stages. Work was initiated in collaboration with T. Coyle, D. Cranmer, and E. Fuller at the National Bureau of Standards (now National Institute of Standards and Technology), Gaithersburg, Maryland, in examining the various phenomena associated with fiber debonding and slip. In contrast to the work being completed by Marshall and Oliver (156) using the Nanoindentor to apply a load to the fibers in a composite to examine these stages of fiber displacement, a standard microhardness indentor is employed. This allows the loads to be increased to 20 N compared with the Nanoindentor's 0.12 N limit. The instrument(s) will be used to investigate the individual forces of debonding and frictional sliding. It appears that a thorough understanding of both forces is necessary to explain observed mechanical behavior in composite materials.

REFERENCES

1. A. H. Cotrell, "Strong Solids," *Proc. R. Soc. London* A282, 2-9 (1963).

2. A. Kelly, "The Strengthening of Metals by Dispersed Particles," *Proc. R. Soc. London* **A282**, 63-79 (1964).

3. H. W. Rauch, W. H. Sutton, and L. R. McCreight, *Ceramic Fibers and Fibrous Composite Materials*, Academic Press, New York, 1968.

4. J. D. Walton and W. J. Corbett, "Metal Fiber Reinforced Ceramics," pp. 223-38 in *Fiber Composite Materials*, American Society of Metals Seminar, October 1964.

5. D. C. Phillips, "Fibre Reinforced Ceramics," pp. 373-428 in *Handbook of Composites, Volume 4 - Fabrication of Composites*, edited by A. Kelly and S. T. Mileiko, Elsevier Science Publishers B. V., North-Holland, The Netherlands, 1983.

6. L. S. Millberg, "The Search for Ductile Ceramics," *J. Metals* 39(11), 10-13 (1987).

7. L. Holiday, "Ceramic Systems," pp. 91-127 in *Composite Materials*, Elsevier Publishing Company, New York, 1966.

8. Y. Baskin, A. Arenberg, and J. H. Handwerk, "Thoria Reinforced by Metal Fibers," *Ceram. Bull.* **38**, 345-48 (1959).

9. Y. Baskin, Y. Horado, and J. H. Handwerk, "Some Physical Properties of Thoria Reinforced by Metal Fibers," *J. Am. Ceram. Soc.* 43, 498-92 (1960).

10. J. R. Tinklepaugh, "Ceramic-Metal Fibre Composite Systems," p. 579 in *Strengthening Mechanisms: Metals and Ceramics*, edited by J. J. Burke, N. L. Reed, and V. Weiss, 12th Sagamore Army Materials Research Conference, Syracuse University Press, 1965.

11. D. C. Phillips, "The Fracture Energy of Carbon-Fiber Reinforced Glass," *J. Mater. Sci.* 7, 1175-91 (1972).

12. D. C. Phillips, "Interfacial Bonding and the Toughness of Carbon Fibre Reinforced Glass and Glass-Ceramics," *J. Mater. Sci.* 9, 1847-54 (1974).

13. D. C. Phillips, R. A. J. Sambell, and D. H. Bowen, "The Mechanical Properties of Carbon Fibre Reinforced Pyrex Glass," *J. Mater. Sci.* 7, 1454-64 (1972).

14. R. A. J. Sambell et al., "Carbon Fiber Composites with Ceramic and Glass Matrices, Part 2: Continuous Fibres," *J. Mater. Sci.* 7, 676-81 (1972).

15. R. A. J. Sambell, D. H. Bowen, and D. C. Phillips, "Carbon Fiber Composites with Ceramic and Glass Matrices, Part 1: Discontinuous Fibres," *J. Mater. Sci.* 7, 663-75 (1972).

16. F. Galasso, M. Basche, and D. Kuemle, "Preparation, Structure, and Properties of Continuous Silicon Carbide Filaments," *Appl. Phys. Lett.* **9**, 37 (1966).

17. S. Yajima et al., "Synthesis of Continuous SiC Fibers with High Tensile Strength," *J. Am. Ceram. Soc.* **59**(7-8), 324-27 (1976).

18. S. Yajima et al., "Anomalous Characteristics of the Microcrystalline State of SiC Fibres," *Nature* **27**(21), 706-7 (1979).

19. K. M. Prewo and J. J. Brennan, "High-Strength Silicon Carbide Fiber-Reinforced Glass-Matrix," *J. Mater. Sci.* **15**, 463-8 (1980).

20. K. M. Prewo, J. J. Brennan, and G. K. Layden, "Fiber Reinforced Glasses and Glass-Ceramics for High Performance Applications," *Ceram. Bull.* **65**(2), 305-22 (1986).

21. R. A. J. Sambell, "The Technology of Ceramic-Fibre Ceramic-Matrix Composites," *Composites* **1**(5), 276-85 (1970).

22. W. B. Hillig, "Strength and Toughness of Ceramic Matrix Composites," *Ann. Rev. Mater. Sci.* **17**, 341-83 (1987).

23. W. Hillig, "Ceramic Composites by Infiltration," *Ceram. Eng. Sci. Proc.* **6**(7-8), 674-83 (1985).

24. I. W. Donald and P. W. McMillan, "Review: Ceramic Matrix Composites," *J. Mater. Sci.* **11**, 949-72 (1976).

25. G. C. Wei and P. F. Becher, "Development of SiC-Whisker-Reinforced Ceramics," *Am. Ceram. Soc. Bull.* **64**(2), 298-304 (1985).

26. D. K. Shetty, "SiC Monofilament-Reinforced Si_3N_4 Matrix Composites," *Ceram. Eng. Sci. Proc.* **6**(7-8), 632-45 (1985).

27. R. P. Boisvert and R. J. Diefendorf, "Polymeric Precursor for SiC Matrix Composites," *Ceram. Eng. Sci. Proc.* **9**(7-8), 873-80 (1988).

28. T. Starr, J. N. Harris, and D. L. Mohr, "Reaction-Sintered Silicon Nitride With Short Fiber Reinforcement," *Ceram. Eng. Sci. Proc.* **8**(7-8), 985-91 (1987).

29. R. H. Jones et al., "Interfacial Chemistry-Structure and Fracture of Ceramic Composites," to be published in *Ceram. Eng. Sci. Proc.* **9**(7-8), 655-62 (1988).

30. R. Naslain et al., "Chemical Vapor Infiltration Technique," pp. 293-304 in *Euro-CVD-Four*, Eindhoven, The Netherlands, 1983.

31. J. C. Whithers, "Chemical Vapor Deposition of Ceramic Composites Containing Whisker and Fiber Reinforcements," pp. 507-20 in *Third International Conference on Chemical Vapor Deposition*, edited by F. A. Glaski, American Nuclear Society, Hinsdale, Ill., 1972.

32. W. H. Pfiefer et al., "Consolidation of Porous Structures by CVD," pp. 463-83 in *Second International Conference on Chemical Vapor Deposition*, edited by J. M. Blocher, Jr. and J. C. Whithers, Electrochemical Society, New York, 1970.

33. J. D. Theis, Jr., "The Process Development and Mechanical Testing of a Carbon/Carbon Composite Fabricated by Chemical Vapor Infiltration of a Filament Wound Substrate," pp. 561-73 in *Third International Conference on Chemical Vapor Deposition*, edited by F. A. Glaski, American Nuclear Society, Hinsdale, Ill., 1972.

34. L. R. Newkirk et al., "Chemical Vapor Deposition Fabrication of Filament-Reinforced Composites for High Temperature Applications," pp. 82-101 in *Chemically Vapor Deposited Coatings*, edited by H. O. Pierson, Am. Ceram. Soc., Columbus, Ohio, 1981.

35. H. O. Pierson, "Carbon Composites from Wool Felt Substrates," pp. 487-505 in *Second International Conference on Chemical Vapor Deposition*, edited by J. M. Blocher, Jr. and J. C. Whithers, Electrochemical Society, New York, 1970.

36. J. J. Gebhardt, "CVD Boron Nitride Infiltration of Porous Structures: Properties of Low Temperature Deposits," pp. 460-72 in *Fourth International Conference on Chemical Vapor Deposition*, edited by G. F. Wakefield and J. M. Blocher, Jr., Electrochemical Society, Princeton, N.J., 1973.

37. H. Hannache, R. Naslain, and C. Bernard, "Boron Nitride Chemical Vapor Infiltration of Fibrous Materials from BCl_3-NH_3-H_2 or BF_3-NH_3 Mixtures: A Thermodynamic and Experimental Approach," *J. Less Common Met.* 95, 221-46 (1983).

38. F. Christin, R. Naslain, and C. Bernard, "A Thermodynamic and Experimental Approach of Silicon Carbide CVD Application to the CVD-Infiltration of Porous Carbon/Carbon Composites," pp. 499-514 in *Seventh International Conference on Chemical Vapor Deposition*, edited by T. O. Sedgwick, Electrochemical Society, Princeton, N.J., 1974.

39. J. Rossignol, I. Langlais, and R. Naslain, "A Tentative Modelization of Titanium Carbide CVI Within the Pore Network of Two-Dimensional Carbon/Carbon Composite Preforms," pp. 596-614 in *Ninth International Conference on Chemical Vapor Deposition*, edited by M. Robinson et al., Electrochemical Society, Princeton, N.J., 1984.

40. A. J. Caputo, R. A. Lowden, and D. P. Stinton, *Improvements in the Fabrication of Ceramic-Fiber-Ceramic-Matrix Composites by Chemical Vapor Deposition*, ORNL/TM-9652, Oak Ridge National Laboratory, Oak Ridge, Tenn., June 1985.

41. A. J. Caputo et al., "Fiber-Reinforced SiC Composites with Improved Mechanical Properties," *Am. Ceram. Soc. Bull.* 66(2), 268-72 (1987).

42. R. A. Lowden et al., *Effects of Infiltration Conditions on the Properties of SiC/Nicalon Composites*, ORNL/TM-10403, Oak Ridge National Laboratory, Oak Ridge, Tenn., May 1987.

43. A. J. Caputo and W. J. Lackey, "Fabrication of Fiber-Reinforced Composites by Chemical Vapor Infiltration," *Ceram. Eng. Sci. Proc.* 5, 654-67 (1984).

44. D. P. Stinton, A. J. Caputo, and R. A. Lowden, "Synthesis of Fiber-Reinforced SiC Composites by Chemical Vapor Infiltration," *Am. Ceram. Soc. Bull.* 65(2), 347-50 (1986).

45. J. Aveston, "Fibres of High Thermal Stability," *Composites* 1(5), 296-99 (1970).

46. A. R. Holtz and M. F. Gretther, "High Tempertaure Properties of Three Nextel Ceramic Fibers," presented at the 32nd International SAMPE Symposium and Exhibition, Anaheim Convention Center, Anaheim, Calif., April 1987.

47. J. C. Romine, "New High-Temperature Ceramic Fiber," *Ceram. Eng. Sci. Proc.* 8(7-8), 755-65 (1987).

48. D. H. Bowen, "Fibre-Reinforced Ceramics," *Fibre Sci. Technol.* 1, 85-112 (1968).

49. L. Holiday, "Theoretical Background," pp. 28-62 in *Composite Materials*, Elsevier Publishing Company, New York, 1966.

50. M. R. Piggott, "Reinforcement Processes," pp. 83-97 in *Load Bearing Fibre Composites*, Pergamon Press, Oxford, England, 1980.

51. M. R. Piggott, "Composite Mechanics," pp. 62-82 in *Load Bearing Fibre Composites*, Pergamon Press, Oxford, England, 1980.

52. B. W. Rosen, "Mechanics of Composite Strengthening," pp. 37-75 in *Fiber Composite Materials*, American Society of Metals Seminar, October 1964.

53. H. L. Cox, "The Elasticity and Strength of Paper and Other Fibrous Materials," *B. J. Appl. Phys.* 3, 72-9 (1952).

54. R. L. Coble and W. D. Kingery, "Effect of Porosity on Physical Properties of Sintered Alumina," *J. Am. Ceram. Soc.* 39(11), 377-85 (1956).

55. K. K. Phani and S. K. Niyogi, "Young's Modulus of Porous Brittle Solids," *J. Mater. Sci.* 22, 257-63 (1987).

56. E. Ryskewitch, "Compressive Strength of Porous Sintered Alumina and Zirconia," *J. Am. Ceram. Soc.* 36, 65 (1953).

57. T. W. Coyle, M. H. Guyot, and J. F. Jamet, "Mechanical Behavior of a Microcracked Ceramic Composite," *Ceram. Eng. Sci. Proc.* 8(7-8), 947-57 (1987).

58. D. L. Harrod and R. T. Begley, "Some General Aspects of Interfaces in Composites," pp. E1-E16 in *SAMPE Advanced Fibrous Reinforced Composites*, Vol. 10, 10th National Symposium and Exhibition, 1966.

59. K. Khaund et al., "Influence of Elastic and Thermal Mismatch on the Local Crack-Driving Force in Brittle Composites," *J. Mater. Sci.* 12, 2269-73 (1977).

60. J. F. Jamet, D. Lewis, and E. Y. Luh, "Characterization of Mechanical Behavior and Fractographic Observations on Compglas SiC/LAS Composites," *Ceram. Eng. Sci. Proc.* 5(7-8), 625-42 (1984).

61. M. R. Piggott, "Reinforced Ceramics, Cements, and Plasters," pp. 211-23 in *Load Bearing Fibre Composites*, Pergamon Press, Oxford, England, 1980.

62. M. R. Piggott, "Failure Processes," pp. 101-19 in *Load Bearing Fibre Composites*, Pergamon Press, Oxford, England, 1980.

63. R. W. Rice, "Mechanisms of Toughening in Ceramic Matrix Composites," *Ceram. Eng. Sci. Proc.* 2(7-8), 661-701 (1981).

64. R. W. Rice et al., "The Effect of Ceramic Fiber Coatings on the Room-Temperature Behavior of Ceramic-Fiber Composites," *Ceram. Eng. Sci. Proc.* 2(7-8), 614-24 (1984).

65. G. Eriksson, "Thermodynamic Studies of High Temperature Equilibria XII. SOLGASMIX," *Chem. Scri. (Sweden)* 8(3), 100-3 (1975).

66. G. Eriksson and E. Rosen, "Thermodynamic Studies of High Temperature Equilibria VIII. General Equations," *Chem. Scri. (Sweden)* 4(5), 193-4 (1973).

67. T. M. Besmann, *SOLGASMIX-PV, a Computer Program to Calculate Equilibrium Relationships on Complex Chemical Systems*, ORNL/TM-5775, Oak Ridge National Laboratory, Oak Ridge, Tenn., April 1977.

68. V. I. Dybkov, "Reaction Diffusion in Heterogeneous Binary Systems, Part 2," *J. Mater. Sci.* 21, 3085-90 (1986).

69. V. I. Dybkov, "Reaction Diffusion in Heterogeneous Binary Systems, Part 3," *J. Mater. Sci.* 22, 4233-39 (1987).

70. V. I. Dybkov, "Reaction Diffusion in Heterogeneous Binary Systems, Part 1," *J. Mater. Sci.* 21, 3078-84 (1986).

71. N. F. Dow, *Study of Stresses Near a Discontinuity in a Filament-Reinforced Composite Metal*, Report No. R63SD61, Missiles and Space Division, General Electric Company, August 1963.

72. L. DiLandro and M. Pegoraro, "Carbon Fibre-Thermoplastic Matrix Adhesion," *J. Mater. Sci.* 22, 1980-86 (1987).

73. G. A. Cooper and A. Kelly, "Tensile Properties of Fibre-Reinforced Metals: Fracture Mechanics," *J. Mech. Phys. Solids* 15, 279-97 (1967).

74. A. Kelly and W. R. Tyson, "Tensile Properties of Fibre-Reinforced Metals: Copper/Tungsten and Copper/Molybdenum," *J. Mech. Phys. Solids* 13, 329-50 (1965).

75. G. A. Cooper and A. Kelly, "Role of the Interface in the Fracture of Fiber-Composite Materials," pp. 90-106 in *Interfaces in Composites*, ASTM STP 452, American Society for Testing and Materials, 1969.

76. A. Kelly, "Interface Effects and the Work of Fracture of a Fibrous Composite," *Proc. R. Soc. London A* 319, 95-116 (1970).

77. V. R. Riley and J. L. Reddaway, "Tensile Strength and Failure Mechanics of Fibre Composites," *J. Mater. Sci.* 3, 41-46 (1968).

78. B. Budiansky, J. W. Hutchinson, and A. G. Evans, "Matrix Fracture in Fiber-Reinforced Ceramics," *J. Mech. Phys. Solids* 34(2), 167-89 (1986).

79. L. B. Greszczuk, "Theoretical Studies of the Mechanics of the Fiber-Matrix Interface in Composites," pp. 42-58 in *Interfaces in Composites*, ASTM STP 452, American Society for Testing and Materials, 1969.

80. D. C. Phillips and A. S. Tetelman, "The Fracture Toughness of Fibre Composites," *Composites* 3(5), 219-25 (1972).

81. J. Aveston and A. Kelly, "Theory of Multiple Fracture of Fibrous Composites," *J. Mater. Sci.* 8, 352-62 (1973).

82. J. Aveston, G. A. Cooper, and A. Kelly, "Single Multiple Fracture: The Properties of Fiber Composites," pp. 15-26 in *National Physics Lab Conference Proceedings*, November 1971.

83. C. Atkinson et al., "The Rod Pull-Out Problem, Theory and Experiment," *J. Mech. Phys. Solids* 30(3), 97-120 (1982).

84. L. T. Drzal et al., "Interfacial Shear Strength and Failure Mechanisms in Graphite Fiber Composites," pp. 1-5 (Sect. 20-C) in *Proceedings of the 35th Annual Technical Conference*, Reinforced Plastics/Composite Institute, The Society of the Plastics Industry, Inc., 1980.

85. J. F. Mandell, K. C. C. Hong, and D. H. Grande, "Interfacial Shear Strength and Sliding Resistance in Metal and Glass-Ceramic Matrix Composites," *Ceram. Eng. Sci. Proc.* 8(7-8), 937-40 (1987).

86. J. F. Mandell et al., "Modified Microdebonding Test for Direct In Situ Fiber/Matrix Bond Strength Determination in Fiber Composites," pp. 87-108 in *Composite Materials: Testing and Design (Seventh Conference)*, ASTM STP 893, edited by J. M. Whitney, American Society for Testing and Materials, Philadelphia, 1986.

87. D. B. Marshall, "Strength and Interfacial Properties of Ceramic Composites," *Mater. Res. Soc. Symp. Proc.* 78 (1987).

88. D. B. Marshall, "An Indentation Method for Measuring Matrix-Fiber Frictional Stresses in Ceramic Components," *J. Am. Ceram. Soc.* 67(12), C259-60 (1984).

89. L. J. Ebert and J. D. Gadd, " A Mathematical Model for Mechanical Behavior of Interfaces in Composite Materials," pp. 89-112 in *Fiber Composite Materials*, Chapter 5, American Society of Metals Seminar October 1964.

90. A. Kelly and C. Zweben, "Poisson Contraction in Aligned Fibre Composites Showing Pull-Out," *J. Mater. Sci.* 11, 582-87 (1976).

91. A. Takaku and R. C. G. Arridge, "The Effect of Interfacial Radial and Shear Stress on Fiber Pull-out in Composite Materials," *J. Phys. D.* 6, 2038-47 (1973).

92. R. S. Williams and K. L. Reifsnider, "Strain Energy Release Rate Method for Predicting Failure Modes in Composite Materials," pp. 248-75 in *Fracture Mechanics, Proceedings of the Eleventh National Symposium on Fracture Mechanics: Part I*, ASTM, Blacksburg, Va., June 1978.

93. S. Ochiai and Y. Murakami, "The Strengthening Effect of Brittle Zones on Ductile-Fiber Composites," *Met. Sci.* 10(11), 401-08 (1977).

94. S. Ochiai and K. Osamura, "A Computer Simulation of Strength of Metal Matrix Composites with a Reaction Layer at the Interface," *Met. Trans.* 18A, 673-79 (April 1987).

95. S. Ochiai and K. Osamura, "A Study of Multiple Fracture Phenomenon of a Coating Film on a Metal Fiber by Means of a Computer Simulation," *J. Mater. Sci.* 21, 2735-43 (1986).

96. S. Ochiai and Y. Murakami, "Tensile Strength of Composites with Brittle Reaction Zones at Interfaces," *J. Mater. Sci.* 14, 831-40 (1979).

97. S. Ochiai and K. Osamura, "Stress Distribution in a Segmented Film on Metal Fiber Under Tensile Loading," *J. Mater. Sci.* 21, 2744-52 (1986).

98. M. H. Rawlins et al., "Interfacial Characterization of Fiber-Reinforced SiC Composites Exhibiting Brittle and Toughened Fracture Behavior," in *MRS Symposium Proceedings, Vol. 78, Advanced Structural Ceramics* (November 1986).

99. S. Novak, Charles Evans and Associates, Redwood City, Calif., private communication to R. A. Lowden.

100. B. L. Butler, D. A. Northrop, and T. R. Guess, "Interfaces in Carbon Fiber/Pyrolytic-Carbon Matrix Composites," *J. Adhes.* 5, 161-78 (1973).

101. M. J. Chappel and R. S. Millman, "The Fabrication of Ceramic-Coated Carbon Fibre Duplex Elements," *J. Mater. Sci.* **9**, 1933-48 (1974).

102. K. Brennfleck et al., "CVD of SiC Interlayers and Their Interaction with Carbon Fibers and with Multi-layered NbN-Coatings," pp. 649-62 in *Proceedings of the 9th International Conference on Chemical Vapor Deposition*, vol. 84-6, Electrochemical Society, 1984.

103. T. Shikama et al., "Mechanical Properties of Molybdenum Coated with Titanium Carbide Film," *J. Mater. Sci.* **18**, 3092-98 (1983).

104. M. Kh. Shorshorov et al., "Brittle Interface Layers and the Tensile Strength of Metal Matrix-Fiber Composites," *J. Mater. Sci.* **14**, 1850-61 (1979).

105. P. S. Theocaris and T. P. Phillippidis, "Influence of the Mesophases on the Mechanical Properties of Three-Phase Composites," *J. Mater. Sci.* 22, 3407-15 (1987).

106. J. J. Brennan, "Interfacial Characterization of Glass-Ceramic Matrix/SiC Fiber Composites," pp. 186-204 in the *Proceedings of Interface Science and Engineering*, Lake Placid, N.Y., July 1987.

107. J. J. Brennan, "Interfacial Characterization of Glass and Glass-Ceramic Matrix/Nicalon SiC Fiber Composites," pp. 549-60 in *Tailoring Multiphase and Composite Ceramics*, edited by R. E. Tressler et al., Plenum Publishing Corporation, 1986.

108. J. J. Brennan, "Interfacial Chemistry and Bonding in Fiber Reinforced Glass and Glass-Ceramic Matrix Composites," pp. 387-400 in *Ceramic Microstructures: Role of Interfaces*, University of California at Berkeley, July 1986.

109. T. Mah et al., "Room-Temperature Mechanical Behavior of Fiber-Reinforced Ceramic Matrix Composites," *J. Am. Ceram. Soc.* 68(1), C27-30 (1985).

110. P. J. Lamicq et al., "SiC/SiC Composite Ceramics," *Am. Ceram. Soc. Bull.* 65(2), 336-38 (1986).

111. W. V. Kotlensky, "Deposition of Pyrolytic Carbon in Porous Solids," *Chem. Phys. Carbon* **9**, 173-262 (1973).

112. H. O. Pierson and M. L. Lieberman, "The Chemical Vapor Deposition of Carbon on Carbon Fibers," *Carbon* **13**, 159-66 (1975).

113. K. L. Luthra, "Thermochemical Analysis of the Stability of Continuous 'SiC' Fibers," *J. Am. Ceram. Soc.* **69**(10), C231-33 (1986).

114. B. Bender et *al.*, "Effect of Fiber Coatings and Composite Processing of Properties of Zirconia-Based Matrix SiC Fiber Composites," *Am. Ceram. Soc. Bull.* **65**(2), 363-9 (1986).

115. W. T. Thompson, A. D. Pelton, and C. W. Bale, "Extension to SOLGASMIX fir INteractive Calculations with the F*A*C*T Thermodynamic Database," *CALPHAD* **7**(2), 113 (1983).

116. B. R. Lawn and V. R. Howes, "Elastic Recovery at Hardness Indentations," *J. Mater. Sci.* **16**, 2745-52 (1981).

117. J. L. Loubet, J. M. Georges, and G. Meille, "Vickers Indentation Curves of Elastoplastic Materials," pp. 72-89 in *Microindentation Techniques in Materials Science and Engineering*, ASTM STP 889, edited by P. J. Blau and B. R. Lawn, American Society for Testing and Materials, Philadelphia, 1986.

118. D. B. Marshall and B. R. Lawn, "Indentation of Brittle Materials," pp. 26-46 in *Microindentation Techniques in Materials Science and Engineering*, ASTM STP 889, edited by P. J. Blau and B. R. Lawn, American Society for Testing and Materials, Philadelphia, 1986.

119. T. J. Clark et al., "Thermal Stability Characterization of SiC Ceramic Fibers: I, Mechanical Property and Chemical Structure Effects," *Ceram. Eng. Sci. Proc.* **7**(7-8), 901-13 (1986).

120. E. Fitzer and R. Gadow, "Fiber-Reinforced Silicon Carbide," *Am. Ceram. Soc. Bull.* **65**(2), 326-35 (1986).

121. S. M. Johnson et al., "Degradation Mechanisms of Silicon Crabide Fibers," *J. Am. Ceram. Soc.* **71**(3), C132-35 (1988).

122. T. Mah et al., "Thermal Stability of SiC Fibers (Nicalon)," *J. Mater. Sci.* **19**, 1191-201 (1984).

123. C. H. Anderson and R. Warren, "Silicon Carbide Fibers and Their Potential Use in Composite Materials. Part 1," *Composites* **15**(1), 16-24 (1984).

124. Y. Hasegawa and K. Okamura, "Synthesis of Continuous Silicon Carbide Fibre: Part 3," *J. Mater. Sci.* **18**, 3633-48 (1983).

125. R. Warren and C-H. Andersson, "Silicon Carbide Fibres and their Potential for Use in Composite Materials," *Composites* 15(2), 101-12 (1984).

126. W. L. Johnson and R. G. Brasfield, "Comparison of Matrix Variation in Nicalon (SiC) Fiber Reinforced Composites," *Mater. Res. Soc. Symp. Proc.* **78**, 215-22 (1987).

127. C. J. Macey, R. L. Lehman, and R. L. Moore, "Surface Analysis of Nicalon SiC Fiber," *Scanning Electron Microsc.* **IV**, 1643-48 (1984).

128. M. Lancin et al., "Analysis by SIMS and by EELS-EDX in a STEM of SiC Fibers Reinforced Composites," *Mater. Res. Soc. Symp. Proc.* 78, 231-38 (1987).

129. A. S. Fareed et al., "Thermomechanical Properties of SiC Yarn," *Am. Ceram. Soc. Bull.* **66**(2), 353-58 (1987).

130. G. Simon and A. R. Busnell, "Mechanical and Structural Characterization of the Nicalon Silicon Carbide Fibre," *J. Mater. Sci.* 19, 3649-57 (1984).

131. G. Simon and A. R. Busnell, "The Creep of Silicon Carbide Fibers," *J. Mater. Sci. Lett.* 2, 80-82 (1983).

132. G. Simon and A. R. Busnell, "Creep Behavior and Structural Characterization at High Temperatures of Nicalon SiC Fibers," *J. Mater. Sci.* 19, 3658-70 (1984).

133. L. C. Sawyer et al., "Thermal Stability Characterization of SiC Fibers: II, Fractography and Structure," *Ceram. Eng. Sci. Proc.* 8(7-8), 914-30 (1986).

134. T. J. Clark et al., "Thermal Degradation of Nicalon SiC Fibers," *Ceram. Eng. Sci. Proc.* **6**(7-8), 576-88 (1985).

135. Y. Sasaki et al., "Raman Study of SiC Fibres Made from Polycarbosilane," *J. Mater. Sci.* **22**, 442-8 (1987).

136. Z. Li and R. C. Bradt, "Thermal Expansion of the Hexagonal (6H) Polytype of Silicon Carbide," *J. Am. Ceram. Soc.* **69**(12), 863-66 (1986).

137. J. A. Coppola and R. C. Brandt, "Measurement of Fracture Surface Energy of SiC," *J. Am. Ceram. Soc.* **55**(9), 455-60 (1972).

138. T. D. Gulden, "Mechanical Properties of Polycrystalline ß-SiC," *J. Am. Ceram. Soc.* **52**(11), 585-90 (1969).

139. R. J. Price, "Structure and Properties of Pyrolytic Silicon Carbide," *Ceram. Bull.* 48(9), 859-62 (1969).

140. D. P. Stinton and W. J. Lackey, "Effect of Deposition Conditions on the Properties of Pyrolytic SiC Coatings for HTGR Fuel Particles," *Am. Ceram. Soc. Bull.* 57(6), 568-73 (1978).

141. P. W. Beaumont and J. C. Aleszka, "Cracking and Toughening of Concrete and Polymer-Concrete Dispersed with Short Steel Wires," *J. Mater. Sci.* 13, 1749-60 (1978).

142. Y. W. Mai, "Strength and Fracture Properties of Asbestos-Cement Mortar Composites," *J. Mater. Sci.* 14, 2091-102 (1979).

143. P. S. Mangat and K. Gurusamy, "Flexural Strength of Steel Reinforced Cement Composites," *J. Mater. Sci.* 22, 3103-10 (1987).

144. D. P. Birnie III, "A Model for Silicon Self-Diffusion in Silicon Carbide: Anti-Site Defect Motion," *J. Am. Ceram. Soc.* 69(2), C33-35 (1986).

145. G. Brebec et al., "Diffusion of Silicon in Amorphous Silica," *Acta Metall.* 28, 327-33 (1980).

146. M. H. Hon, R. F. Davis, and D. E. Newbury, "Self-Diffusion of ^{30}Si in Polycrystalline ß-SiC," *J. Mater. Sci.* 15, 2073-80 (1980).

147. M. H. Hon and R. F. Davis, "Self-Diffusion of C^{14} in Polycrystalline ß-SiC," *J. Mater. Sci.* 14, 2411-21 (1979).

148. Y. A. Vodakov et al., "Diffusion of Boron and Aluminum in n-SiC," *Sov. Phys.-Solid State* 8(4), 1040-1 (1966).

149. D. M. Brown and P. R. Kennicot, "Glass Source Diffusion in Si and SiO_2," *J. Electrochem. Soc.* 118(2), 293-300 (1971).

150. B. A. Bender et al., "Electron Microscopy of Ceramic Fiber-Ceramic Matrix Composites -- Comparison with Processing and Behavior," *Ceram. Eng. Sci. Proc.* 5(7-8), 513-29 (1984).

151. R. F. Cooper and K. Chyung, "Structure and Chemistry of Fibre-Matrix Interfaces in Silicon Crabide Fibre-Reinforced Glass-Ceramic Composites: An Electron Microscopy Study," *J. Mater. Sci.* 22, 3148-60 (1987).

152. W. D. Kingery, H. K. Bowen, and D. R. Ulman, *Introduction to Ceramics*, John Wiley and Sons, Inc., New York, 1960.

153. W. C. LaCourse, "The Strength of Glass," pp. 451-512 in *Introduction to Glass Science*, edited by L. D. Pyle, H. J. Stevens, and W. C. LaCourse, Plenum Press, New York, 1972.

154. J. Bowling and G. W. Groves, "The Propagation of Cracks in Composites Consisting of Ductile Wires in a Brittle Matrix," *J. Mater. Sci.* 14, 443-9 (1979).

155. M. F. Doerner and W. D. Nix, "A Method for Interpreting the Data from Depth Sensing Indentation Instruments," *J. Mater. Res.* 1(4), 601-9 (July/August 1986).

156. D. B. Marshall and W. C. Oliver, "Measurement of Interfacial Mechanical Properties in Fiber-Reinforced Ceramic Composites," *J. Am. Ceram. Soc.* 70(8), 542-8 (1987).

157. W. C. Oliver, "Progress in the Developments of a Mechanical Properties Microprobe," *MRS Bull.* 5, 15-19, (1986).

158. E. Fueller, T. Coyle, D. Cranmer, and R. A. Lowden, "Characterization of the Fiber/Matrix Interface by Instrumented Indentation Testing," presented at the 90th Annual Meeting of the American Ceramic Society, May 1988.

159. K. T. Faber et al., "Frictional Stress Evaluation Along the Fiber-Matrix Interface in Ceramic Matrix Composites," *J. Am. Ceram. Soc.* 69(9), C208-9 (1986).

160. D. K. Shetty, "Shear-Lag Analysis of Fiber Push-Out (Indentation) Tests for Estimating Interfacial Frictional Stress in Ceramic Matrix Composites," *J. Am. Ceram. Soc.* 71(2), C107-9 (1988).

161. Personal ommunications with K. Griffith, Ceramatec, Inc., Salt Lake City, Utah, to R. A. Lowden.

162. C. H. Hsueh, "An Analytical Evaluation of Interfacial Shear Strength for Fiber Reinforced Ceramic Composites," to be published in *J. Mater. Sci.*

163. C. H. Hsueh, "Elastic Load Transfer from Partially Embedded Axial Loaded Fiber to Matrix" to be published in *J. Amer. Ceram. Soc.*

164. Y. Termonia, "Theoretical Study of the Stress Transfer in Single Fibre Composites," *J. Mater. Sci.* 22, 504-8 (1987).

165. D. B. Marshall and A. G. Evans, "Failure Mechanisms in Ceramic-Fiber/Ceramic-Matrix Composites," *J. Amer. Ceram. Soc.* 68(5), 225-31 (1985).

166. D. J. Hannant, "Fibre Reinforced Cements," pp. 429-500 in *Handbook of Composites, Volume 4 - Fabrication of Composites*, edited by A. Kelly and S. T. Mileiko, Elsevier Science Publishers B. V., North-Holland, The Netherlands, 1983.

167. P. K. Mallick, "Mechanics," pp. 73-167 in *Fiber-Reinforced Composites*, Marcell Dekker, Inc., New York, 1988.

APPENDIX A

AUGER ELECTRON SPECTROSCOPY

APPENDIX A. AUGER ELECTRON SPECTROSCOPY

The Auger electron spectroscopy techniques for chemical analysis of surfaces is based on the Auger radiationless process. A core-level electron is ionized by an impinging electron, and the atom can decay to a lower-energy state through electronic rearrangement. The ejected electron, or Auger electron, will possess a kinetic energy that is proportional to the difference in energy states, and this energy is characteristic of the parent atom. The Auger electrons can then be captured and analyzed to determine surface compositions by analysis of the peaks in the Auger spectrum. Table A-1 lists the spectral peaks for elements pertinent to the examined composites as listed in "Handbook of Auger Electron Spectroscopy," L. E. Davis et al., Physical Electronics Division, Perkin-Elmer Corporation, Eden Prairie, Minnesota.

Table A-1. Auger spectral peaks for selected elements.

Element	Auger peak (eV)
Boron	179
Carbon	272
Oxygen	503
Aluminum	1396 68
Silicon	1619 92
Molybdenum	186 2044
Chlorine	181
Ar in Si	215

APPENDIX B

DETAILS OF THE FIBER-SHEATH ANALYSIS

APPENDIX B. DETAILS OF THE FIBER-SHEATH ANALYSIS

In the analysis of the tensile method for the determination of interfacial stresses, it was assumed that the radial contraction and the forces associated with this phenomenon could be ignored. References 89 and 92 give detailed mathematical analyses of the forces acting at the interface of a fiber contained in a matrix. The concepts are drawn from a single fiber having no neighbors; thus, forces exerted by the close proximity of another fiber are not considered.

For a fiber embedded in a matrix in which the system is subjected to an external load, the forces in the matrix are given by the expressions

$$\sigma_{rr} = a^2\epsilon_{zz}(1 - 2\nu)(1 - b^2/r^2)(K/\beta) , \qquad (B\text{-}1)$$

$$\sigma_{\theta\theta} = a^2\epsilon_{zz}(1 - 2\nu)(1 - b^2/r^2)(K/\beta) , \qquad (B\text{-}2)$$

$$\sigma_{zz} = E\epsilon_{zz} + a^2\nu\epsilon_{zz}(1 - 2\nu)(K/\beta) , \qquad (B\text{-}3)$$

$$\sigma_{r\theta} = \sigma_{rz} = \sigma_{\theta z} = 0 ;$$

and

$$\epsilon_{rr} = d\theta/dr = a^2/\beta\epsilon_{zz}[(1 - 2\nu) - (2b^2/r^2)] - \nu\epsilon_{zz} , \qquad (B\text{-}4)$$

$$\epsilon_{\theta\theta} = \theta/r = a^2/\beta\epsilon_{zz}[(1 - 2\nu) + (2b^2/r^2)] - \nu\epsilon_{zz} , \qquad (B\text{-}5)$$

$$\epsilon_{r\theta} = \epsilon_{rz} = \epsilon_{\theta z} = 0 .$$

Those for the fiber (primed) are given as

$$\sigma'_{rr} = \sigma'_{\theta\theta} = \epsilon_{zz} K_f ([a^2(1 - 2\nu_m) + b^2/\beta] - (\nu_m - \nu_f)) \quad , \qquad \text{(B-6)}$$

$$\sigma'_{zz} = E_f \epsilon_{zz} + 2\nu_f \epsilon_{zz} K_f ([a^2(1 - 2\nu_m) + b^2/\beta] - (\nu_m - \nu_f)) \quad , \qquad \text{(B-7)}$$

$$\sigma'_{zr} = \sigma'_{r\theta} = \sigma'_{\theta\zeta} = 0;$$

$$\epsilon'_{rr} = \epsilon'_{\theta\theta} = \theta'/r = \epsilon_{zz} ([a^2(1 - 2\nu_m) + b^2/\beta] - \nu_m)) \quad , \qquad \text{(B-8)}$$

$$\epsilon'_{r\theta} = \epsilon'_{rz} = \epsilon'_{\theta z} = 0 \; ;$$

where $\beta = [1/(\nu_m - \nu_f)][a^2(1 - 2\nu_m)(1 - K_m/K_f) + b^2(1 + (1 - 2\nu_m)(1 - K_m/K_f)]$

and $K = E/(1 + \nu)(1 - 2\nu)$.

The variables are as given in previous equations, and the directions of the stress vectors are shown in Figure 7.7. These expressions show that the stresses and strains in the fiber and matrix (sheath) are dependent on the diameter of the fiber, the thickness of the coating, and the Poisson ratios of the components. The Poisson ratio for ceramic materials is small, and from the preceding relationships, it can be seen that if ν is relatively small and the coating is thin ($b \approx a$), then the radial and tangential forces resulting from an applied stress or strain will be insignificant in ceramic-ceramic systems.

END

DATE FILMED

11 / 1 / 90